Dark-to-bright Transition of Coronal Holes and Spectropolarimetric Imaging of Type III Solar Radio Bursts Using the MWA

A thesis submitted for the degree of
Doctor of Philosophy

by

Md Mozibur Rahman

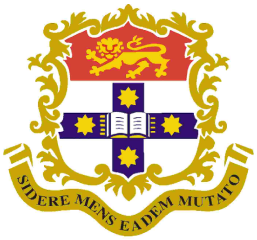

School of Physics
University of Sydney
Australia

February 2020

Declaration of originality

To the best of my knowledge, the content of this thesis is my own work. This thesis contains no copy or paraphrase of work published by another person, except where duly acknowledged in the text. There is no material in this thesis which has been presented for a degree at the University of Sydney or any other university.

Md Mozibur Rahman

Included papers and attribution

The papers are listed below on which Chapters 2 and 3 are organized.

Chapter 2 **On the Relative Brightness of Coronal Holes at Low Frequencies**

M. M. Rahman, Patrick I. McCauley, and Iver H. Cairns,

Published in *Solar Physics*, (2019) **294**:7.

I was primarily responsible for this work.

Chapter 3 **Spectropolarimetric Imaging of Metric Type III Solar Radio Bursts**

M. M. Rahman, Iver H. Cairns, and Patrick I. McCauley,

Submitted in *Solar Physics*, 2019.

I was primarily responsible for this work.

Some of the results of this thesis were presented for the oral/poster presentation at the following conferences:

On the Relative Brightness of Coronal Holes at Low Frequencies

M. M. Rahman, Patrick I. McCauley, and Iver H. Cairns,

Presented at the *100th AGU Fall Meeting*, Washington, DC 2018 (Poster).

A Study of Coronal Holes in Emission at Low Frequencies Using the Murchison Widefield Array

M. M. Rahman, Patrick I. McCauley, and Iver H. Cairns,

Presented at the *School of Physics Symposium, University of Sydney*, Sydney 2018 (Oral).

A Study of Coronal Holes in Emission at Low Frequencies

M. M. Rahman, Patrick I. McCauley, and Iver H. Cairns,

Presented at the *17th Australian Space Research Conference (ASRC)*, Sydney 2017 (Poster).

Acknowledgements

All praises are due to the Almighty who gave me this opportunity of completing this research work successfully. My heartfelt acknowledgement goes to my PhD supervisor Prof. Iver Hugh Cairns. It would not be possible to finish this work without his continuous guideline during my PhD research. I want to thank Prof. Cairns for giving me endless inspirations during a hard time of my research. I want to acknowledge my co-supervisor Prof. Donald Blair Melrose for constructive discussions in research.

I had an excellent opportunity to work with my friend like coauthor and lab mate Patrick I. McCauley. I am grateful to him for his support and guideline that were fruitful and effective to complete this research work. I am grateful to my lab mates James, Ronald, and Fiona. They were very friendly and helpful at any issues in my course of doing PhD.

It would be great feelings for me if I could have shown my thesis work to my beloved father (who passed away on the 2nd of December 2017 at the age of 60 years old) but alas! I could not do that! I believe that he is watching and hearing this good news for sure.

My mother is a source of inspiration for me. She gives me mental strength when I get frustrated and go through a bad time. I am thankful to her for giving me a lot of support and encouragements. I am grateful to my sister Panna, brother-in-law Afzal, and brother Sumon, for always giving me inspiration during my good and bad days. My love and affection go to Jannat, Yasin, and Joairiya.

I want to express my gratitude to Dr. Rumi, Dr. Samira, Dr. Nipa, Dr. Deeba, Dr. Sabina, Dr. Zobaer, Dr. Samiul, Dr. Arif, Mukta, Mariya, Bappi, and Ema. The MWA science team is acknowledged for supplying data and software for free. The University of Sydney International Scholarship Scheme supports this research work.

At last but not least, I would like to give thanks to them who have not been explicitly acknowledged here.

Md Mozibur Rahman

Abstract

This PhD thesis contains 5 Chapters. **Chapter 1** presents a short overview of the solar corona, quiet Sun, active regions, solar flares, and coronal holes. The magnetoionic theory, the gyromagnetic, bremsstrahlung, and plasma emission mechanisms, the generation and propagation of the radio waves in the solar corona are then briefly described. The FORWARD software package for modelling the thermal coronal emission based on the MHD Algorithm outside a Sphere (MAS) model, is discussed next. The *Murchison Widefield Array* (MWA) interferometer is described then, followed by descriptions of solar type radio bursts, their classes, and their appearance in the dynamic spectrum. Afterwards, the radio properties of coronal holes and type III solar radio bursts are described thoroughly, focusing first on observations using the MWA and other radio instruments and then on theory. The intriguing properties of type IIIs described include their appearance, drift rates, decay time, and circular polarization properties.

In **Chapter 2** (Rahman et al., 2019), we present low-frequency (80 – 240 MHz) radio observations of coronal holes (CHs) made with the MWA. CHs are expected to be dark structures relative to the background corona across the MWA's bandwidth due to their low densities. However, we observe that multiple CHs near disk center transition from being dark structures at higher frequencies to bright structures at lower frequencies ($\lesssim$ 145 MHz). We compare our observations to synthetic images obtained using the software suite FORWARD, in combination with the MAS model of the global coronal magnetic

field, density, and temperature structure. The synthetic images do not exhibit this transition, and we quantify the discrepancy as a function of frequency. We propose that the dark-to-bright transition results from refraction of radio waves into the low density CH regions, and we develop a qualitative model based on this idea and the relative optical depths inside and outside a CH as a function of frequency. We show that opacity estimates based on the MAS model are qualitatively consistent with our interpretation, and we conclude that propagation and relative absorption effects are a viable explanation for the dark-to-bright transition of CHs from high to low frequencies.

In **Chapter 3**, we present low-frequency radio observations of circular polarization in sixteen isolated type III solar radio bursts observed by the MWA between August 2014 and November 2015. We find that near burst onset, most of the burst events show degrees of circular polarization 5−30% at 80 MHz and 15−40% at 240 MHz and these percentages are 3−15% and 5−25% near burst maximum. We then measure polarization fraction as a function of burst source position and find on average higher polarization fraction when the source is near disk center and lower polarization fraction near the limb. We study the total intensity (Stokes I), circularly polarized intensity (Stokes V), and polarization fraction ($\mid V \mid/I$) profiles of a type III burst event with no source motion and two burst events with source motion as a function of position at times near burst maximum. For the burst event with no source motion, we obtain symmetric profiles for Stokes I, V, and $\mid V \mid/I$ but we find asymmetric $\mid V \mid/I$ profiles for those burst events which have source motion. We argue this is due to fundamental emission at the front of the type III electron beam and motion of the burst source. We then perform imaging studies of the polarization fraction for moving sources. At burst onset, we find higher polarization fractions for the burst source, which is due to a larger contribution from fundamental plasma emission. At burst maximum the

polarization fraction is lower, corresponding to a mixture of fundamental and harmonic emission. During the decay phase, the emission is dominated again by the fundamental component, which decays with lesser polarization fraction due to scattering. This pattern of fundamental, fundamental and harmonic, and then fundamental emission with time is consistent with the interpretations of Dulk et al. (1984), Robinson et al. (1994), and Robinson and Cairns (1998). We propose that scattering effects can be a viable reason for getting a lower polarization fraction for type III events. Finally, we measure the decay time (t_d) after peak intensity for three events as a function of frequency (f), finding $t_d \propto f^{-2.0\pm0.1}$ from 80 to 240 MHz and larger t_d as compared with the previous observations ($t_d \propto f^{-1.1\pm0.1}$).

In **Chapter 4**, we present analyses of low-frequency observations of type III solar radio bursts using the MWA. Specifically, near times of burst maximum intensity, we study the burst source sizes, flux densities, and brightness temperatures of 10 type III events in both total (Stokes I) and polarized intensity (Stokes V) images. We find that the source area A increases as f decreases, varying as $A \propto f^{-2.4\pm0.4}$ and $A \propto f^{-2.6\pm0.4}$ in Stokes I and V images, respectively, whereas the MWA beam area varies as $f^{-2.5\pm0.2}$. We propose that the source sizes, once separated from the effects of the MWA beam, do not support scattering (which predicts $A \propto f^{-4}$) as the primary physical effect determining the observed source sizes. We interpret the observed source size changes as due to divergence of open magnetic field lines, which causes the source size to increase at lower frequencies and larger heights. On average, the total and polarized fluxes are found to increase as frequency decreases, although some events have a peak flux at intermediate frequencies $\approx 108-132$ MHz. We find total fluxes of 550 SFU at 80 MHz and 50 SFU at 240 MHz averaged over our sample, which are consistent with the results (log-flux density of type IIIs ranging from 0.2 to 4.8 at 80 MHz) reported by Dulk and Suzuki (1980). Our

flux values are within the range of their flux values. On average the brightness temperatures T_b decrease as f increases and we find maximum T_b = 4×10^{11} K at 80 MHz and minimum T_b = 1.2×10^{8} K at 240 MHz. Our results of T_b are consistent with the observations (logT_b: 7−11.5 at 80 MHz) of Dulk and Suzuki (1980). T_b does not depend on the source's position, although this finding is uncertain since we analyse a small number of burst events. We argue that divergence of open field lines is a viable process for the source size increasing as the frequency decreases.

In **Chapter 5**, a final summary and suggestions for future work are presented. The PhD thesis ends with a set of references.

Contents

Chapter 1

Introduction and Literature Review

This introductory chapter starts with a brief description of the solar corona, quiet Sun features, active regions, solar flares, and coronal holes. The magnetoionic theory, the gyromagnetic, bremsstrahlung, and plasma emission mechanisms, and the generation and propagation of radio waves in the corona are then described. The FORWARD software package for modelling thermal coronal radio emissions, based on the MHD Algorithm outside a Sphere (MAS) model, is presented next. The *Murchison Widefield Array* (MWA) interferometer is described then, followed by descriptions of solar radio bursts, their classes, and their appearance in the dynamic spectrum. After that, the radio properties of coronal holes and type III solar radio bursts are described thoroughly, focusing first on observations using the MWA and other radio instruments and then on theory. The properties described include their drift rates, appearance, decay time, and polarization properties.

1.1 Solar Corona

The Sun is a source of energy for not only human beings but also for many other living creatures on the Earth. The dynamic activities of the Sun are of great interest to astronomers and space physicists due to not only its closeness to the Earth but also its influence on solar terrestrial activities. We know that the Sun consists of a core, convective zone, photosphere, chromosphere, and corona. Figure 1.1 shows these regions of the Sun's interior and its atmosphere. It is quite fascinating that the temperature of the Sun increases from a few thousand degrees kelvin to up to 3 million degrees kelvin as we move outward from the photosphere to the corona (or outermost part of the atmosphere) of the Sun.

The Sun's atmosphere consists of four distinct regions: photosphere, chromosphere, transition region, and corona. Figure 1.2 shows characteristic temperatures and particle densities of these regions as a function of height. The photosphere is a thin spherical layer of thickness $\approx$ 300 km and its temperature is 4500−6000 K. Most of the visible emission radiates from the photosphere. There is another spherical layer of thickness $\approx$ 2000 km above the photosphere called the chromosphere and its temperature is 10^4 K approximately. The chromosphere is separated from the lower corona by a thin layer of a hundred km thickness which is called the transition region. At the transition region, the temperature increases rapidly steeply from $\approx 10^4$ to 10^6 K.

The outermost part (or atmosphere) of the Sun is the corona, a gaseous plasma region with a temperature of 1 to 3 million degrees kelvin. Details about the solar interior and its atmosphere are explained by Priest (1982). We note that the particle densities in different regions of the Sun's atmosphere decrease as we move outward from the surface of the Sun (photosphere). The corona has three domains that correspond to different observing frequencies (Figure 1.2), 1)

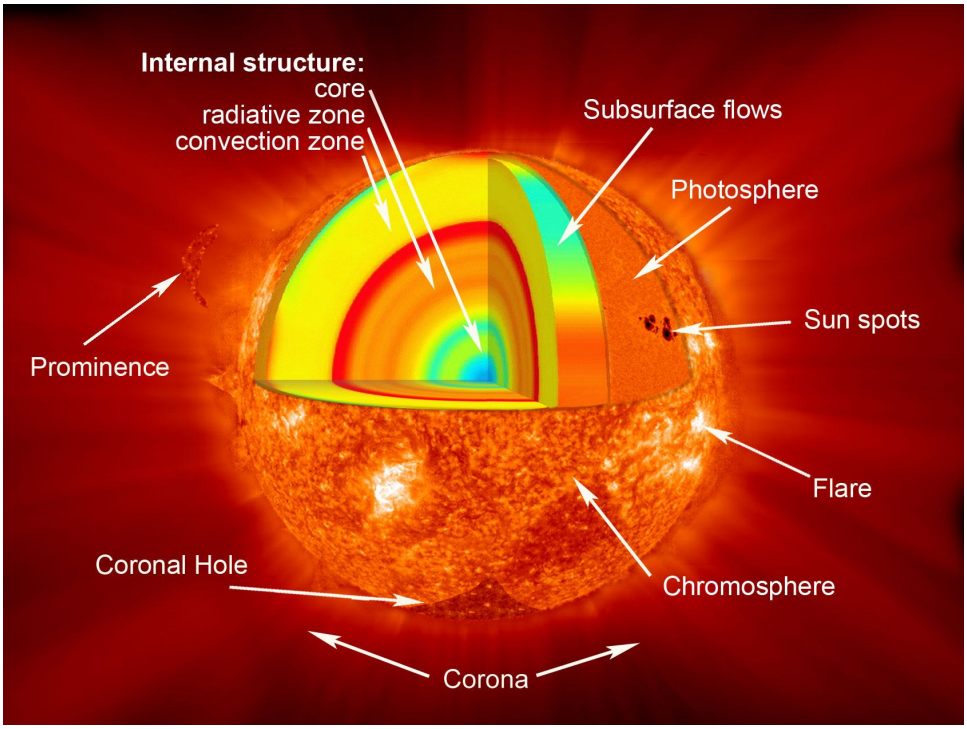

Figure 1.1: Different regions of the Sun and its atmosphere. Credit: NASA.

the lower corona from the photosphere up to 1.2 $R_\odot$, 2) the middle corona from 1.3 $R_\odot$ to 3 $R_\odot$, and 3) the upper corona from roughly 3 $R_\odot$ and above. Figure 1.3 shows a bright and intense solar coronal image at 171 $\mathring{A}$ obtained by the *Solar Dynamics Observatory* (SDO). The lower and upper parts of the corona contain intense active regions with strong magnetic fields arranged in magnetic loops so that the energetic particles can not easily leave. Some low-latitude coronal holes also exist in the corona. We add that coronal holes are low density and less active regions of the solar corona. Details about coronal holes will be discussed in later Sections and in Chapter 2 of this thesis (Rahman et al., 2019).

The Sun and corona can be observed across the electromagnetic spectrum, using different observing techniques for different wavelength ranges. Each wavelength of observation corresponds to a particular height of the solar atmosphere. Gases and plasmas with different temperatures produce light at

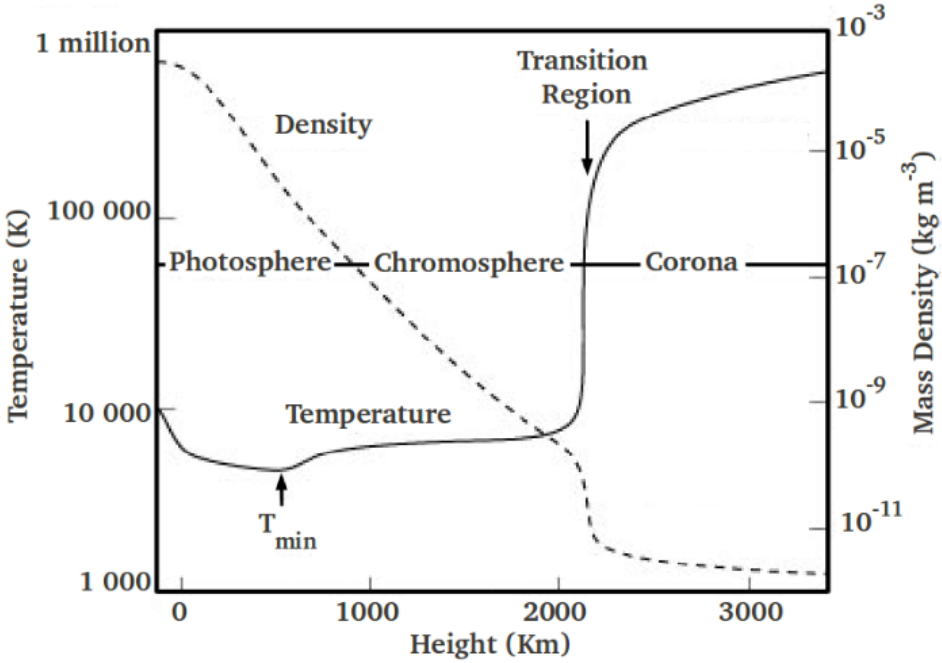

Figure 1.2: Variations of the temperatures and densities of the Sun's atmosphere as function of height whereas height zero corresponds to the solar surface (1 $R_\odot$) (Lang, 2001).

different wavelengths. Higher temperature atoms produce photons with higher energies and so shorter wavelengths. The Sun emits EUV light and x-rays at shorter wavelengths and radiates radio emission at longer wavelengths. The Atmospheric Imaging Assembly (AIA) instrument on SDO can successfully observe the Sun's atmosphere at different wavelengths of light that correspond to different heights from the surface of the Sun.

The photosphere can be observed at visible wavelengths. During solar eclipses, the chromosphere and corona are observed when the Moon occults the bright photosphere. The chromosphere is seen not only at microwave frequencies but also at ultraviolet frequencies. The corona can be observed in soft and hard x-rays, extreme ultraviolet (EUV), ultraviolet (UV), gamma rays, and radio frequency photons. The different layers of the corona can be observed in

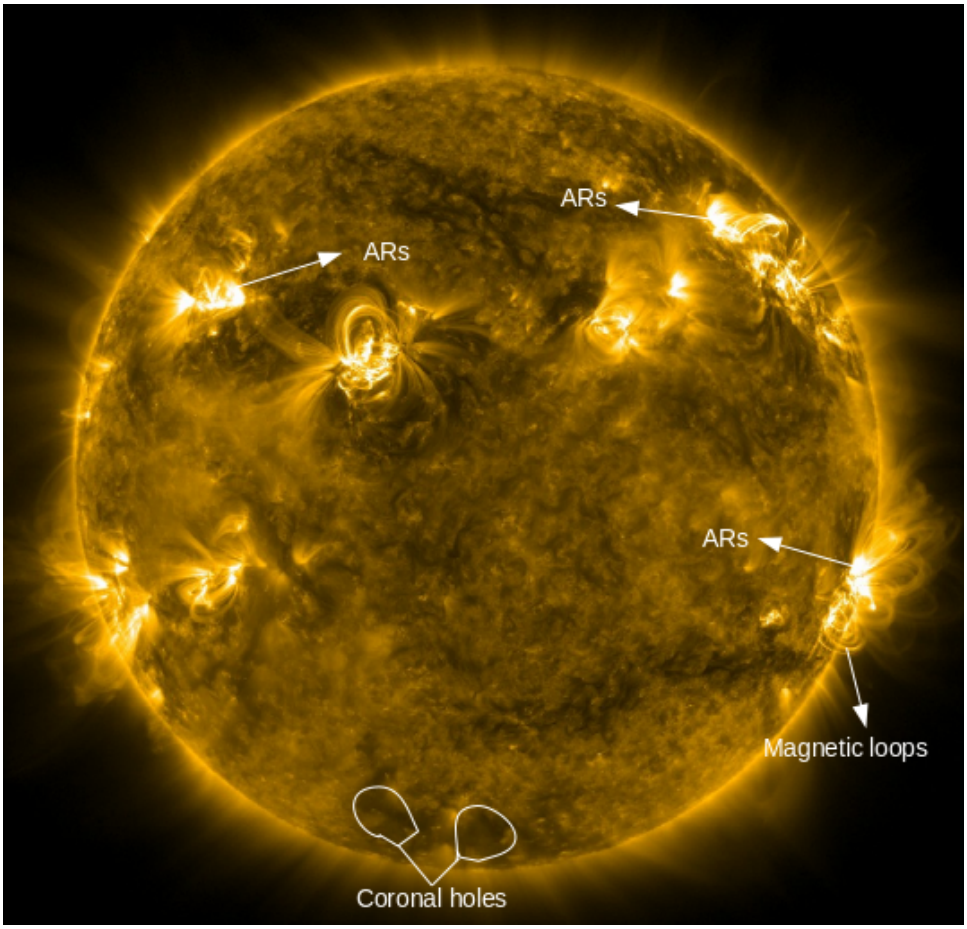

Figure 1.3: Solar corona at 171 $\mathring{A}$ with presence of active regions (ARs), magnetic loops, and coronal holes. Credit: SDO/AIA.

different wavelength ranges: the lower corona can be observed at centimeter and decimeter radio wavelengths, the middle corona at meter and decameter radio wavelengths, and the upper corona at hectometer and kilometer radio wavelengths. Ground-based microwave and radio observations can be used to observe the chromosphere and the corona.

1.1.1 Quiet Sun

The quiet Sun is said to be the undisturbed Sun where there are no active regions and coronal holes, in the absence of any transient events like solar flares, prominences, coronal mass ejections, etc. As a result, the quiet Sun is viewed as a static, spherically symmetric hot ball of plasma. Solar radio emissions are often divided into two components, a slowly varying background component corresponding to the quiet Sun and a sporadic component corresponding to solar radio bursts (Kundu, 1965). The quiet Sun is defined to be when and where the corona is less active, for instance during solar minimum, and emits mostly thermal emissions because of its lesser activity and the absence of active regions (see Figure 1.4). But during the solar maximum phase and from active regions, for instance, bursts of non-thermal radiation are produced that propagate to the Earth through interplanetary space as a result of solar flares, coronal mass ejections, etc.

Figure 1.5 shows the solar corona around solar minimum (top) and solar maximum (bottom) during solar eclipses. During solar minimum, the corona has a simple structure that looks calm and undisturbed due to there being few sunspots. There are streamers in the low latitude corona and a coronal hole at the north pole. There may be some prominences at the streamer sites. On the other hand, near solar maximum the corona looks very complex with many streamers at all latitudes due to there being numerous sunspots and magnetically active regions. Of course an eclipse can exist for only a few minutes and requires a favourable place and time to observe it. Thus coronagraphs are an alternative way to provide on-demand spectacular views of the Sun's atmosphere. A coronagraph is a telescope that is capable of seeing things close to the Sun since it produces an artificial solar eclipse. It uses a disk to block Sun's bright photosphere and reveal the fainter corona, stars, planets, and

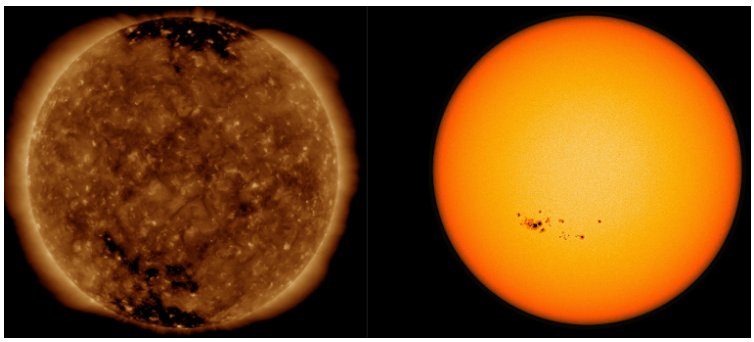

Figure 1.4: (Left) Solar quiet corona around solar minimum at 193 $\mathring{A}$ with coronal holes at both the north and south poles. (Right) The photosphere at visible light with darker sunspots. Credit: NASA/NOAA.

comets. The SOlar and Heliospheric Observatory (SOHO), European Solar Telescope (EST), and Goode Solar Telescope (GST), etc are capable of doing solar coronagraphy to observe the Sun's atmosphere and its corona.

Radio emission from the quiet Sun has a minimum level when there are no sunspots or active regions on the solar disk. The dominant component of background emission released from the quiet Sun is thermal in nature (Alissandrakis, 1994). This radio emission is mostly due to the free-free or bremsstrahlung emission process in the presence of relatively weak magnetic fields (Kundu, 1965). On the other hand, the emission in radio bursts is non-thermal in nature and generally originates from active regions, often in association with flares and coronal mass ejections.

The observations of the Sun's slowly-varying component have been done by many authors, but including specifically by Lantos and Alissandrakis (1994) at meter wavelengths (164 MHz) and by Lantos et al. (1987); Lantos et al. (1992) at decimeter, meter, and decameter wavelengths and Schonfeld et al. (2019). Weak noise storm continua, the most frequent sources of slowly-varying component, were observed at 169 and 73.8 MHz using Nançay and Clark Lake Radioheliographs, respectively. This emission is typically believed to peak near

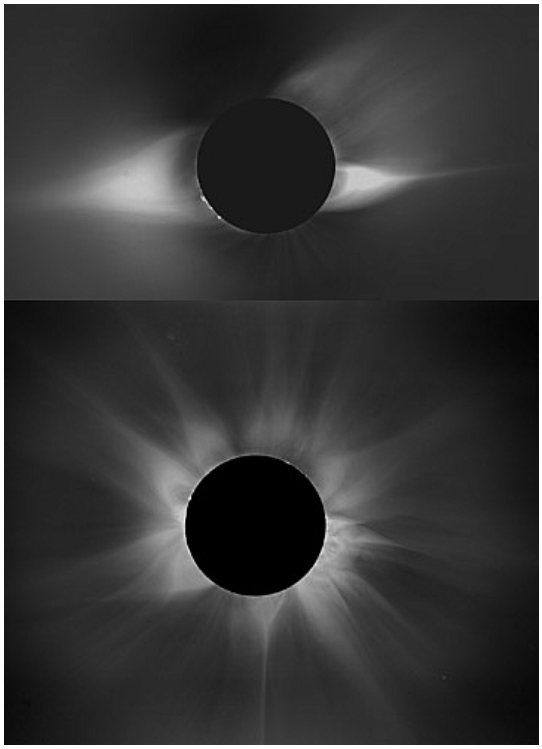

Figure 1.5: Solar corona around solar minimum (top) and solar maximum (bottom). Credit: NCAR's High Altitude Observatory and Rhodes College.

2.8 GHz (or 10.7 cm wavelength) and is often referred to as the $F_{10.7}$ solar microwave flux despite its wide range of frequencies.

The physics of the quiet Sun, where the emission comes from slowly varying components during quiescent periods has attracted a great deal of interest from the solar physics research community (Kundu, 1965; Lantos et al., 1992; Alissandrakis, 1994). In particular, the radio observations of the quiet Sun were investigated by many authors at multiple radio frequencies using many radio instruments, as reviewed by Alissandrakis (1994), Lantos (1999), Mercier and Chambe (2009), Shibasaki et al. (2011), and Mercier and Chambe (2012). For instance, Axisa et al. (1971) observed the quiet Sun at 169 MHz using the *Nançay Radioheliograph*, finding that the thermal radio emissions are linked with filaments and coronal streamers. Later, using the *Culgoora radioheliograph*,

two-dimensional images of the quiet Sun at 80 and 160 MHz were reported by Dulk and Sheridan (1974). They investigated maps of the brightness distribution of the quiet Sun and reported that darker radio regions were well correlated with darker regions on the UV maps, which corresponded to coronal holes whereas the brighter regions are associated with quiescent filaments.

1.2 Solar Radio Sources

During more active periods of the Sun, the corona shows dynamic activity with complex phenomena that include emissions at radio and other wavelengths which are not thermal in nature. These sources are active regions, solar flares, etc., some of which occur on small spatial scales and others on large spatial scales. Details of thermal vs non-thermal radiation and active regions are given in Sections 1.2.1 and 1.2.2. Solar flares are described in Section 1.2.3.

1.2.1 Thermal vs Non-thermal Radiation

A plasma system is defined as thermal when 1) there are no transient emissions for a long period of time or 2) the plasma particles in that system have a Maxwellian distribution function and the particles are at thermal equilibrium. On the other hand, a system such as an environment full of plasma particles is said to be non-thermal when 1) there are transient emissions on short time scales or 2) the plasma particles are not at thermal equilibrium, with either non-Maxwellian distribution functions or more than one Maxwellian distribution function for one or more plasma species.

1.2.2 Active Regions

Active regions (ARs) are coronal regions where the magnetic fields are strong and evolving, as coronal structures are fed by lower-lying structures in the chromosphere and below. ARs are usually bright in EUV observations and are often a source of non-thermal emissions. They are the most intense and prominent features in the solar corona, make up only a fraction of solar surface, and are visible in the photosphere as a group of sunspots at optical wavelengths. Figure 1.3 exhibits some bright and glowing ARs at high latitude and near the solar limb at EUV wavelengths. We also see closed magnetic field lines and magnetic loops in these ARs.

During active periods of the Sun, dynamic processes such as solar flares, prominences, CMEs, etc are associated with ARs (Kivelson and Russell, 1995) and occur due to restructuring of the magnetic field. Some ARs are source regions for solar wind streams with slow speeds (400 km/s). Although usually the sources of fast solar wind streams (speeds $\geq$ 600 km/s), coronal holes can also produce slow solar wind streams (He et al., 2010).

1.2.3 Solar Flares

Solar flares are sudden explosions on the Sun that occur when energy stored in magnetic fields is released. They usually produce a burst of emission from gamma and x-ray to radio emission across the electromagnetic spectrum. Solar flares generally happen in ARs. They generally have three phases: 1) a preflare phase that lasts for several hours to a few minutes, 2) a flash/impulsive phase that lasts for about 5 minutes, and 3) the main phase that lasts for few hours depending on the flare intensity. These three phases can be recognised in Figure 1.6. The preflare phase is from about 13:50 UT to 13:56 UT in which soft x-ray emission increases gradually but little if any hard x-rays and gamma ray

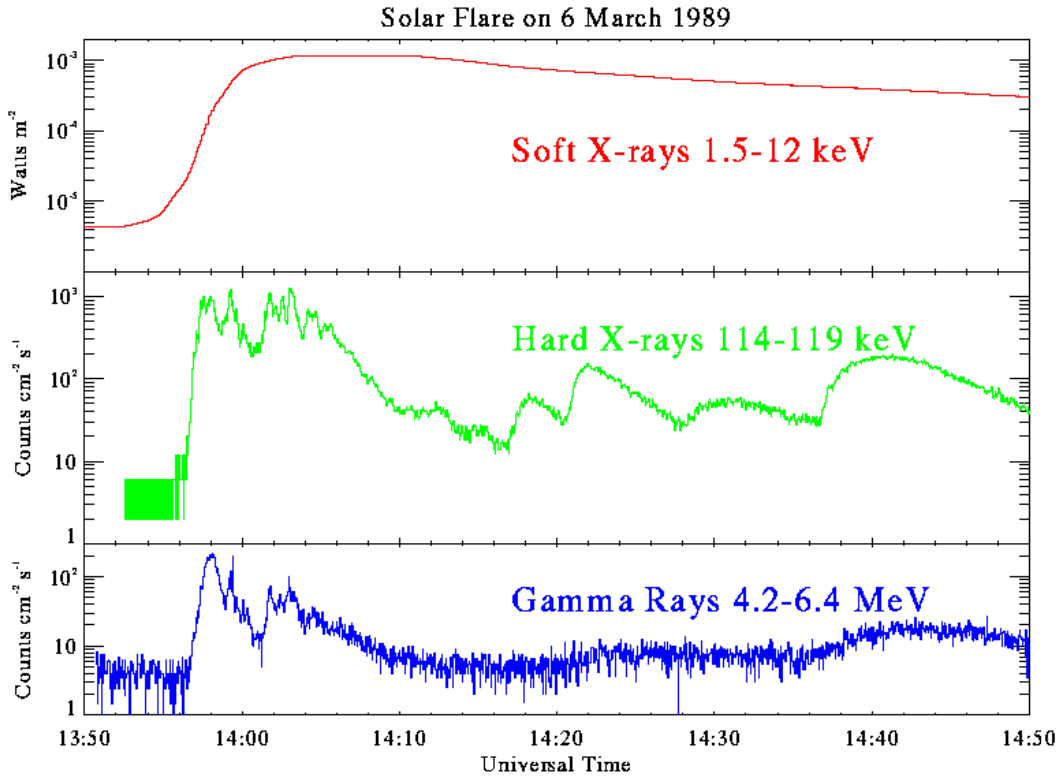

Figure 1.6: Time profiles of soft x-, hard x-, and gamma rays for a large solar flare on March 6, 1989. Credit: NASA/NOAA.

emissions are detected above the instrumental background level. During the flash phase, soft x-ray emission rises very steeply by two order of magnitudes in energy flux and remains high whereas the hard x-rays and gamma rays also show rapid increase in energy flux with short but intense spikes of emission, each lasting either a second or a few seconds until about 14:06 UT. In the main phase after 14:06 UT, the hard x-rays and gamma rays decay more or less exponentially with time constants measured in minutes. The soft x-ray emission continues to rise to a later peak and decay slowly with a longer time constant, sometimes as long as a few hours. It is noted that during the third phase, the soft x-ray emission always decays smoothly as compared to the hard x-rays and gamma rays.

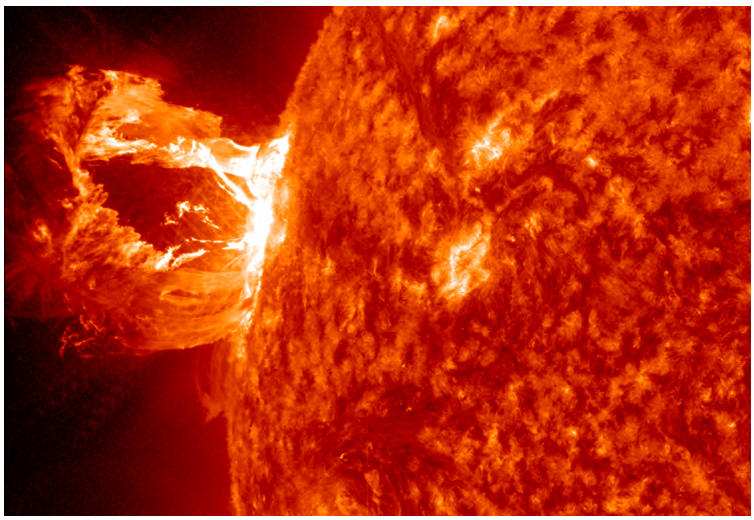

Figure 1.7: Intense solar flare (image is obtained from NOAA/NASA).

Figure 1.7 shows a massive solar flare. During the preflare phase, an active region filament (or prominence) and its overlying arcade of magnetic loops rise slowly due to weak instability or nonequilibrium state. In the flash phase, the unstable magnetic field lines that are stretched out start to break and reconnect, which releases huge energy and causes the filament/prominence to erupt rapidly. The plasma material is heated to temperatures of 10^7 K or greater within a few minutes (Golub and Pasachoff, 2010). During the main phase of the flare, as reconnection continues hot x-ray loops with ribbons at their footpoints are created as magnetic field lines fall back (Kivelson and Russell, 1995). As a result, massive energy $\approx 10^{32}$ erg (Emslie et al., 2004) is released from the flare site within a few minutes. Highly energetic particles can be produced during solar flares (McLean and Labrum 1985, p-56). It is noted that all solar flares do not necessarily follow all three phases.

Solar flares have five classes based on x-ray intensity, X-class, M-class, C-class, B-class, and A-class. X-class is the highest energy class of flares and A-class is the lowest energy class. Each letter is assigned to a numerical range, with

$A = 1{\times}10^{-8} - 10^{-7}$, $B = 1{\times}10^{-7} - 10^{-6}$, $C = 1{\times}10^{-6} - 10^{-5}$, $M = 1{\times}10^{-5} - 10^{-4}$, and $X \geq 1{\times}10^{-4}\ Wm^{-2}$. It is noted that each class is divided into a logarithmic scale from 1 to 9, for instance from X1 to X9, M1 to M9, etc. The energy of X2 is thus twice the energy as of X1.

Powerful solar flares (C5 or greater) always generate non-thermal emission (Benz et al., 2005, 2007), usually type III bursts in a frequency range that varies from a few MHz to a few GHz. Depending on the magnetic field configuration, weaker solar flares may or may not able to generate type III bursts (Reid and Vilmer, 2017). The type IIIs associated with hard x-ray solar flares were surveyed by Benz et al. (2005) from 100 MHz to 4 GHz. They selected 201 RHESSI flares larger than C5 and reported that meter-wave type III bursts were associated in 33% of all x-ray flares.

1.3 Coronal Holes

The corona always exists at all latitudes. During quiet solar periods, the corona has less dynamic activity but may have coronal holes (CHs) present, primarily visible in x-rays and EUV at low latitudes (Cranmer, 2009). Figure 1.8 shows a big CH at 193 $\mathring{A}$ obtained by the SDO. We see the CH as a clearly darker region compared to the surrounding corona. CHs are low-density regions in the inner solar corona that are darker regions in x-rays relative to the corona because the x-ray intensity is linearly dependent on the density squared. CHs are thought to be low-density regions due to their open magnetic field lines. As a result, energetic particles (*e.g.* ionized atoms, electrons, and protons) are not confined by the open magnetic field and thus easily escape from CHs, leading to lower densities. Usually, near solar minimum, plasma particles are ejected along the open magnetic fields of CHs to form the highest speed components of the solar wind that flows into the interplanetary space and even past the Earth

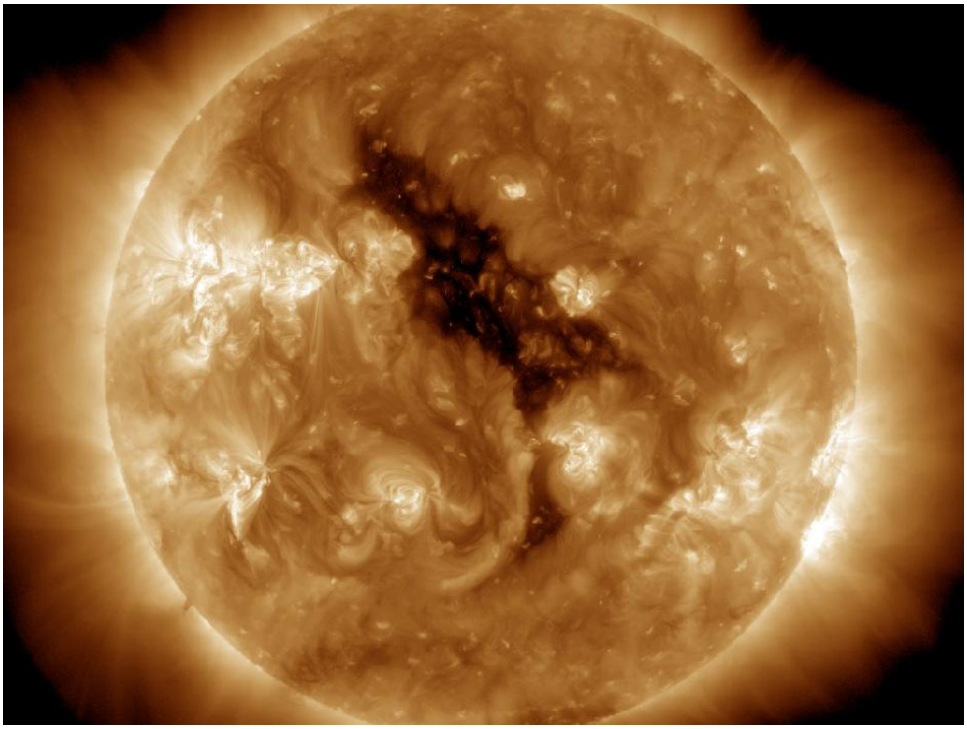

Figure 1.8: 193 $\mathring{A}$ image of coronal hole on 2012/06/02 at 23:25:32 UT obtained from NASA/AIA.

(Verbanac et al., 2011).

1.3.1 Types of Coronal Holes and Their Importance in Solar Physics Research

Based on the position of CHs in the corona, there are two types of CHs: polar and low-latitude CHs. During times of low solar activity, the Sun's magnetic field is dominated by a rotationally-aligned dipole component and CHs exist near the north and south poles of the Sun. On the other hand, CHs exist at all solar latitudes during more active periods of the solar cycle.

CHs are important for not only scientific reasons but also their impact on space weather during solar minimum. CH plasmas have a lower density which

is suitable for studies of collisionless kinetic processes that are the ultimate dissipation mechanisms for many theories of coronal heating (Cranmer, 2009). CHs produce fast solar wind streams that result in ionospheric turbulence and geomagnetic storms (Verbanac et al., 2011) near solar minimum which cause disruptions in radar and satellite communications. In addition, radio observations have revealed that some CHs are seen as darker regions at higher frequencies (≥ 150 MHz) as compared to the surrounding corona and some other CHs are observed as regions of brightness enhancements at lower frequencies ≈ 100 MHz or below (McCauley et al., 2017; Rahman et al., 2019).

The reason for observing radio-dark CHs at higher frequencies and radio-bright CHs at lower frequencies is worthy of more detailed investigation. This is done in Chapter 2 of this thesis (Rahman et al., 2019). Our conclusion is that this transition is real and is due to the refraction and propagation effects caused by the density inhomogeneities, as suggested by Alissandrakis (1994). We also characterized the appearance of CHs and their plasma properties, density and temperature at different radio frequencies and heights from surface of the corona.

1.4 Magnetoionic o- and x-Modes

The magnetoionic theory (Hartree, 1931) is one of the two oldest branches of plasma theory. It is a theory of cold, magnetized plasma where the thermal motion of the electrons is neglected and the ions form a uniform positively charged background but otherwise have no role in the system (Melrose, 1986). The motion of the electrons in a uniform magnetic field is taken into account in the theory. This theory was developed in connection with the propagation of radio emission in the ionosphere. There are two independent parameters in magnetoionic theory: the (angular) electron plasma frequency ω_p and the

(angular) electron cyclotron frequency $\Omega_e = eB/m_e$. The Equation for the dispersion relation of waves in this medium may, in this case, be written as a quadratic equation for n^2 which is known as the Appleton-Hartree formula for the refractive index n (Hutchinson, 2005):

$$n^2 = 1 - \frac{X(1-X)}{1 - X - \frac{1}{2}Y^2 sin^2\theta \pm ((\frac{1}{2}Y^2 sin^2\theta)^2 + (1-X)^2 Y^2 cos^2\theta)^{1/2}}. \quad (1.1)$$

Here the magnetoionic parameters are $X = \omega_p^2/\omega^2$ and $Y = \Omega_e/\omega$, ω is the radial frequency, and θ is the angle between the magnetic field vector $\vec{B}$ and the wave vector $\vec{k}$. Equation (1.1) has two (double) solutions for ω that are real, referred to as the o- (ordinary) and x- (extraordinary) modes.

Figure 1.9 plots the dispersion curves for the o-, x-, and z-modes. The z-mode is the lower frequency branch of x-mode, which is of no interest here since it has $\omega \leq \omega_p$ and so cannot propagate to a distant observer (only radio waves with $\omega > \omega_p$ can do this). Radio waves are evanescent at frequencies which are below the cutoff frequencies for both o- and x-modes, where $n^2 = 0$. The cutoff frequency for the o-mode is $\omega_o = \omega_p$. For the x-mode, the cutoff frequency is $\omega_x = \frac{\Omega_e}{2} + \frac{1}{2}(4\omega_p^2 + \Omega_e^2)^{1/2}$. The '$\pm$' sign in Equation (1.1) refer to the o- or x-mode: for propagation perpendicular to the magnetic field, the '+' sign denotes the o-mode and the '$-$' sign indicates the x-mode. It is noted that for propagation parallel to the magnetic field, the '+' sign denotes left hand circularly polarized mode and the '$-$' sign indicates the right hand circularly polarized mode.

Radio waves associated with the so-called "plasma emission" mechanism have fundamental (f_p) and harmonic ($2f_p$) components that exhibit circular polarization (Melrose, 2009). An important aspect concerning the polarization is that nonlinear fundamental emission processes involving Langmuir waves

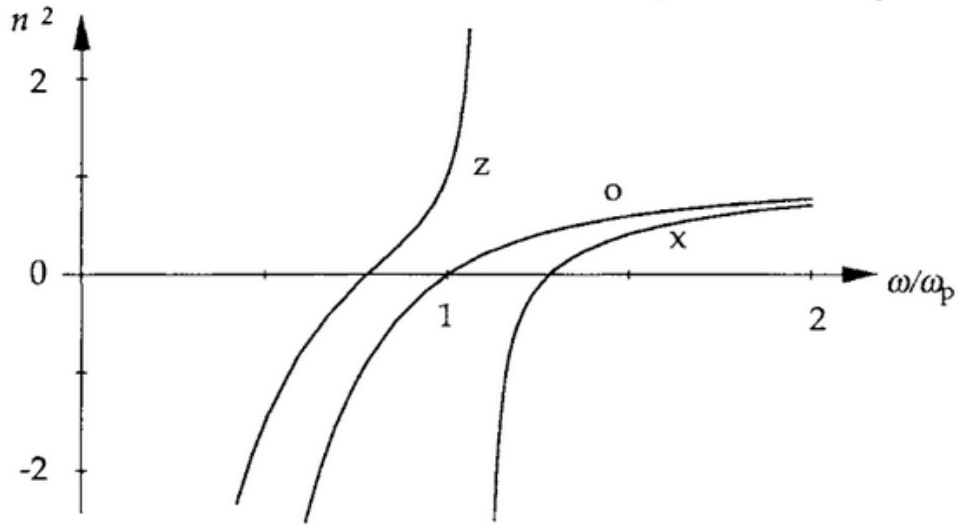

Figure 1.9: Dispersion curves for the magnetoionic o- and x- mode waves (the z-mode is of no interest here). The squares of the refractive indices are considered for frequencies near the plasma frequency and an angle θ greater than 0 (Kirk et al. 1994, p-120).

produce radiation between the plasma frequency ω_p and the cutoff frequency of the x-mode $\omega_x = \frac{\Omega_e}{2} + \frac{1}{2}(4\omega_p^2 + \Omega_e^2)^{1/2}$ (Melrose, 1986; Kirk et al., 1994). It is noted that in this frequency range, only the o-mode can propagate. Thus, fundamental emission exhibits 100% circular polarization in the o-mode. This actually happens only for type I solar radio bursts, as explained more below. Type II and III bursts also exhibit fundamental emissions but are never 100% circularly polarized in the o-mode (Melrose, 2009). The percentage of circular polarization is up to $\approx$ 70% for fundamental type II and III bursts (Kirk et al., 1994). In comparison, second harmonic emission is weakly polarized or even unpolarized (Dulk and Suzuki, 1980; Suzuki et al., 1980; Suzuki and Dulk, 1985; Kirk et al., 1994; Robinson and Cairns, 1998; Reid and Ratcliffe, 2014). The polarization of type III bursts observed by the *Murchison Widefield Array* (MWA) is addressed in detail in Chapter 3 of this thesis.

1.5 Radio Emission from Solar Corona

Different radio emission mechanisms are briefly described in this Section. The bremsstrahlung, gyromagnetic, and plasma emission mechanisms are presented in Sections 1.5.1, 1.5.2, and 1.5.3, respectively.

1.5.1 Bremsstrahlung Emission

The solar corona is a fully ionized plasma where electrons can move freely. The radiation emitted by unbound free electrons due to their acceleration by the electric fields of other charged particles (mainly protons) is called free-free or bremsstrahlung emission. In this case, the free electrons are deflected by the Coulomb fields of ions. As a result, some kinetic energy of electrons convert into radiation. In the corona, this is often referred to as free-free emission because it does not involve charged particles moving between bound states in an atom.

The free-free or bremsstrahlung emission, due to the interaction between electrons and protons, occurs in the corona and results in observable thermal radio emission. Indeed, the radio radiation originating from the quiet Sun, coronal holes, streamers, and active regions is due to the bremsstrahlung emission mechanism (Kundu, 1965; Rybicki and Lightman, 1979; McLean and Labrum, 1985; Aschwanden, 2005).

1.5.2 Gyromagnetic Emission

In an ionized plasma medium with a magnetic field $\vec{B}$, the charged particles spiral along and gyrate around the magnetic field lines. Therefore, the associated emission mechanism is called gyromagnetic emission. Based on the speed of rotation of the particles, the emissions originated are classified into three types: 1) if the electrons gyrate with non-relativistic speeds around $\vec{B}$, the emission produced is called gyroresonant emission (Aschwanden, 2005), 2) if the electrons

have mildly relativistic speeds then the radiation is known as gyrosynchroton emission, and 3) if the electrons gyrate with relativistic speeds about $\vec{B}$, the radiation is called synchroton emission. It is noted that all three mechanisms produce non-coherent emission that is proportional to the amount of particles involved (Rybicki and Lightman, 1979; McLean and Labrum, 1985).

Gyroresonant/Cyclotron Emission: In this mechanism, the electrons spiral along the magnetic field lines and gyrate in a hyperbolic trajectory. The frequency of the electron gyration is called the electron gyro (or cyclotron) frequency f_B and is

$$f_B = \frac{eB}{2\pi m_e c}, \tag{1.2}$$

where e and m_e are the charge (1.6×10^{-19} C) and mass (9.1×10^{-31} kg) of electrons, respectively, B is the magnetic field in T, and c is the speed of light (3×10^{8} ms^{-1}). By using these values in Equation (1.2) we obtain f_B[Hz] = $93.3B$[T]. Thus we can easily estimate the gyrofrequency or magnetic field from one another. When the electrons are non-relativistic then they emit circularly polarized electromagnetic radiation near f_B and at harmonics such that f/f_B <10 (White and Kundu, 1997).

Gyrosynchrotron Emission: This emission mechanism is for electrons with mildly relativistic gyro speeds. Gyrosynchrotron emission is concentrated at the harmonics 10< f/f_B <100 (Dulk and Marsh, 1982).

Synchrotron Emission: When the electrons have relativistic gyro motions then the emission spectrum is power-law and extends to very high harmonics >> 100 (Wild et al., 1963). It is possible for hot electrons to produce synchrotron emission in the solar corona with brightness temperatures $\approx 10^{11}$ K (Tsvetanov and Charugin, 1981). Synchrotron emission exhibits linear polarization. An old interpretation is that some type IV solar radio bursts are due to synchrotron emission mechanism (Ramaty and Lingenfelter, 1967).

1.5.3 Plasma Emission

The solar corona is an ionized plasma medium. If it is in thermal equilibrium then the plasma particles have Maxwellian distributions. Any perturbation in the medium can cause plasma oscillations. As a result, some complex phenomena can happen which give rise to radio emission. The emission process can happen in two stages: 1) Energetic electrons are accelerated during some transient phenomenon like a solar flare, CME, shock, etc, and 2) The accelerated electrons interact with plasma particles and either directly produce transverse electromagnetic waves at the (electron) plasma frequency f_p or its harmonic frequency $2f_p$ or else electronic Langmuir waves near f_p that are then converted into f_p or $2f_p$ radiation. The expression for the electron plasma frequency f_p (Gurnett and Bhattacharjee 2005, p-11):

$$f_p = \frac{1}{2\pi}\sqrt{\frac{N_e e^2}{\epsilon_0 m_e}}. \tag{1.3}$$

Here N_e is the electron number density and ϵ_0 is the permittivity of free space. If we substitute parameters $e = 1.6 \times 10^{-19}$ C, $\epsilon_0 = 8.8542 \times 10^{-12}$ Fm^{-1}, and $m_e = 9.1 \times 10^{-28}$ kg into Equation (1.3) then we find $f_p = 8.98 \times \sqrt{N_e}$ [m^{-3}]. We note that type I (storms), II, and III solar radio bursts are associated with plasma emission (Kirk et al. 1994, p-193).

1.6 Propagation of Radio Waves

In an ionized system such as a cold plasma medium, the electric fields of an electromagnetic wave force the electrons and ions to oscillate about their equilibrium positions. The net effects of electron motion change the refractive index. Radio waves propagating in a plasma medium in the absence of a magnetic field experience: 1) bending of their ray paths due to changes of refractive index,

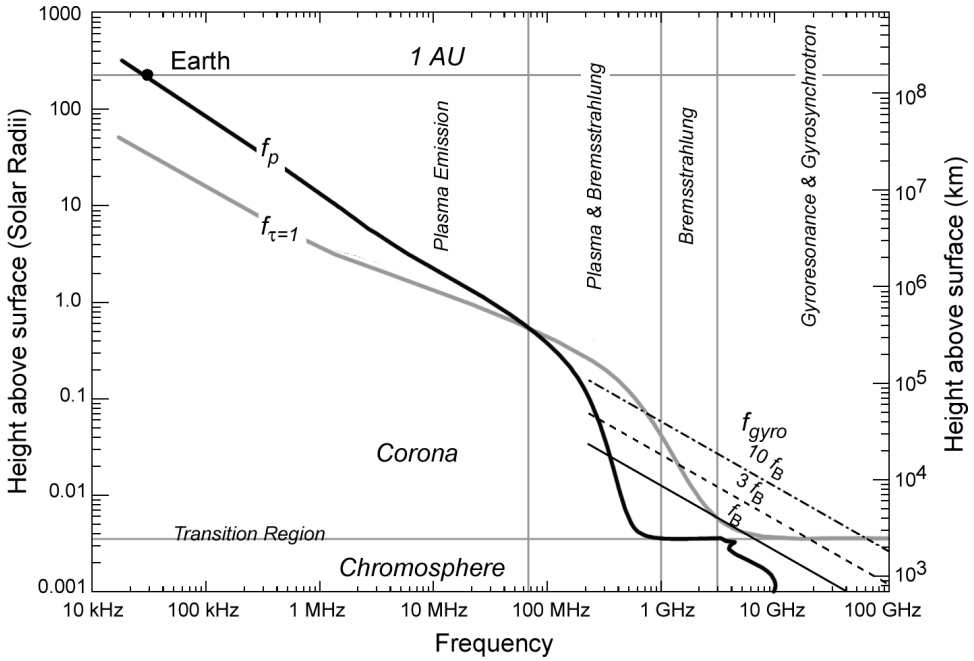

Figure 1.10: The plot describes different radio emission mechanisms operating in the solar atmosphere at various heights and frequencies. At meter wavelength ranges and sufficient heights, the magnetic field is weak. Thus gyromagnetic frequency f_B is negligible and the plasma frequency f_p is dominant. The plasma emission and bremsstrahlung mechanisms are expected at meter wavelength ranges. On the other hand, gyroresonant and gyrosynchrotron emissions occur at microwave frequencies. It is clear from the plot that microwave frequencies and meter wavelengths correspond to chromospheric heights and the solar corona, respectively. Image credit: Gary and Hurford (2005).

refracting towards smaller n, and 2) attenuation due to absorption (Kundu, 1965). We consider the medium to be homogeneous and non-conducting (specifically, the conductivity $\sigma = 0$). The refractive index n of the medium is (Rohlfs and Wilson, 2004):

$$n = \frac{c}{\nu} = \sqrt{\epsilon\mu} = \frac{ck}{\omega}, \tag{1.4}$$

where c is the speed of light, ν is the phase speed of the radio wave propagating into the medium, ϵ and μ denote permittivity and permeability of the medium,

and k is the wave number.

If the medium under consideration is conducting ($\sigma \neq 0$) and unmagnetized, the dispersion Equation (1.1) for radio waves yields,

$$n = \sqrt{1 - \frac{f_p^2}{f^2}}, \tag{1.5}$$

where $f_p = \omega_p/2\pi$ is the electron plasma frequency and f is the frequency of the radio wave.

Equation (1.5) is very significant for radio wave propagation in the solar corona. We see three things: 1) If $f > f_p$, then the refractive index is real and radio waves will propagate. In this case n is less than unity and the wave will refract towards a less dense medium. 2) If $f = f_p$, then $n = 0$. 3) If $f < f_p$, then the refractive index is imaginary and the radio waves will not propagate through the medium but reflect back towards where they originated. An important situation in this thesis is when the radio waves are produced near the local f_p (fundamental emission) and its second harmonic $2f_p$ (harmonic emission).

The electron plasma density will decrease as we move radially outward from the solar corona, as suggested by Newkirk (1967). Thus the plasma frequency will be smaller at larger heights and smaller electron densities as implied by Equation (1.3). As a result, the radio waves will be produced first at higher frequencies or lower heights and then they will drift to lower frequencies or higher heights. As a result, radio waves originating from the complex phenomena associated with solar flares, CMEs, shocks, etc can be observed at different frequencies that correspond to different heights in the solar corona.

1.7 FORWARD Software Package and MAS Model

FORWARD is a software package that is used to compute the thermal coronal radio emissions, coronal magnetic field configurations, etc. based on input density, temperature, magnetic field, and thermodynamic models. It is a set of about 200 IDL procedures and functions that form a Solar Software package (Freeland and Handy, 1998) for synthesizing observables and comparing them to coronal data from EUV imagers, UV polarimeters, white light coronagraphs, and radio telescopes, etc. FORWARD includes several analytic or numerical models in its distribution (Low and Hundhausen, 1995; Gibson et al., 2010), which then create synthetic 3D models of the Sun's plasma parameters, usually through solutions of the MHD equations.

A user-defined interface is available into the software package, which then specifies the input global model of the 3D distribution of plasma and magnetic fields to generate a desired observable quantity. This observed quantity or observable arises from different physical processes (e.g. thermal bremsstrahlung, gyroresonant emission, Thomson scattering (scattering off of free electrons by photospheric light and results in emission of polarized and even unpolarized radiation), etc.) that can be manifested at different wavelengths of light in the corona. Detailed information about the functions of the FORWARD software package is given by Gibson et al. (2016).

One of the MHD codes that produces the input data is the MAS code. MAS stands for the "Magnetohydrodynamic Algorithm outside a Sphere" model (Linker et al., 1999; Lionello et al., 2009) which is capable of calculating the plasma density, temperature, and magnetic field in the corona for a certain range of heights. The MAS model has been used by some authors to predict the thermal radio emissions (bremsstrahlung), coronal plasma density, temperatures,

magnetic field strength in the corona and to compare these radio emissions with observations (McCauley et al., 2017, 2018; Rahman et al., 2019).

1.8 MWA Radio Telescope and Its Science Targets

The *Murchison Widefield Array* (MWA) is a radio telescope situated in Western Australia that is capable of taking images of the solar corona, solar radio bursts, and multiple astrophysical objects from 80 to 300 MHz (Lonsdale et al., 2009; Tingay et al., 2013a). It has 128 aperture arrays (known as tiles) accessible at a time, each having 16 dipole polarization antennas. Figure 1.11 shows an MWA tile. The 128 tiles or aperture arrays are distributed in a centrally condensed configuration with an area approximately 3 km in diameter (Mohan and Oberoi, 2017). The standard time and frequency resolution of MWA are 0.5 s and 40 kHz, respectively. There are 12 broad frequency channels, each having a bandwidth of 2.56 MHz, that can be spaced from 80 to 300 MHz. The MWA and its functions are described by Tingay et al. (2013a) and the science targets are presented by Bowman et al. (2013) and Tingay et al. (2013b).

Recently, a significant amount of research work has been done using MWA observations of type III solar radio bursts (McCauley et al., 2017, 2018; Cairns et al., 2018; Mohan et al., 2019), low frequency emission of bright fast radio bursts (Sokolowski et al., 2018), circular polarization of the quiescent corona (McCauley et al., 2019), and coronal holes in emission (Rahman et al., 2019) observed from 80 to 240 MHz.

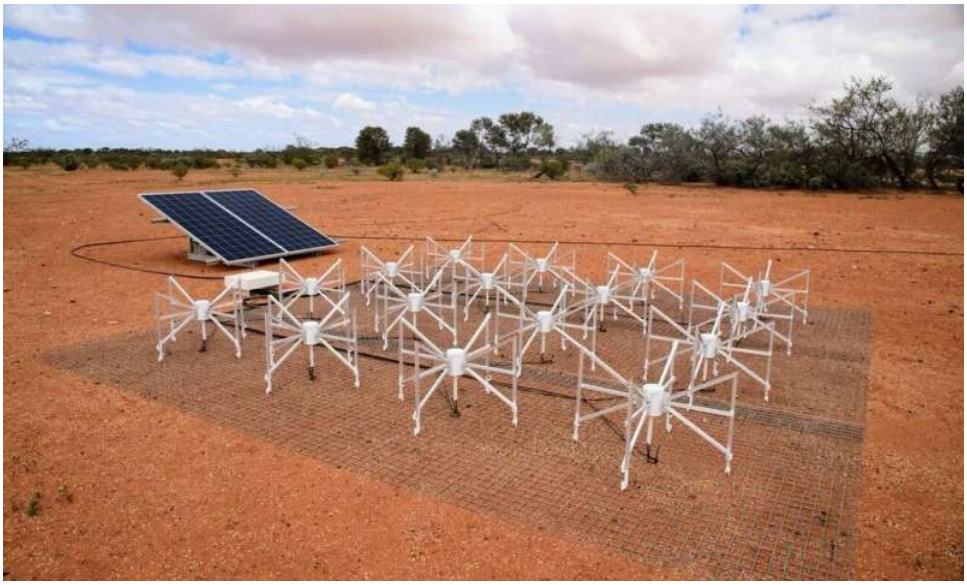

Figure 1.11: 1 out of 128 tiles of MWA radio telescope. Source: https://phys.org/news/2017-12-mwa-radio-telescope-expansion-completeexploration.html

1.9 Radio Observations of Coronal Holes

Coronal holes (CHs) were first observed at the optical wavelengths 5303, 5694, and 6374 $\mathring{A}$ by Waldmeier (1956) at the Swiss Federal Observatory in Zürich. Munro and Withbroe (1972) later studied CHs and suggested that the density and electron temperature are lower in these darker CH regions as compared to the surrounding corona. The first radio observations of CHs were reported by Dulk and Sheridan (1974), measured using the *Culgoora radioheliograph* at 80 and 160 MHz. They found darker CHs at higher frequency and relatively brighter CHs at lower frequency. A few years later, quiet Sun studies were made in the frequency range from 80 to 160 MHz using the *Culgoora radioheliograph* (Sheridan, 1978), where disk centered CHs were also observed to be darker at higher frequency as compared to the surrounding corona. Measurements of the plasma properties of CHs and importance of these measurements on theoretical

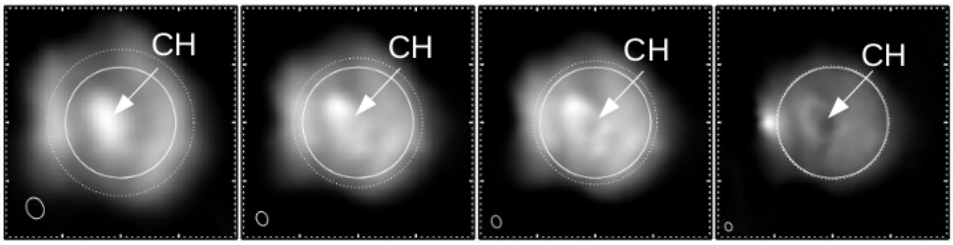

Figure 1.12: MWA observation of a CH at 80, 132, 161, and 240 MHz (from left to right) on September 21, 2015 near 05:13:33 UT (Rahman et al., 2019). The inner solid circles indicate the optical disk and the outer dotted circles indicate the height of the plasma layer for each frequency given by the Newkirk (1961) density model. The ellipses at the lower left corners indicate the MWA synthesized beam sizes.

models of coronal heating and solar wind acceleration have appeared in the literature during the past few decades (Harvey and Sheeley, 1979; Parker, 1991; Hudson, 2002; Cranmer, 2009; Wang, 2009).

CHs were reported to be regions of depressed brightness in the observations of Alissandrakis et al. (1985); Lantos et al. (1992); Lantos and Alissandrakis (1999) using the *Nançay Radioheliograph* at 169 and 408 MHz. Some CHs near the disk center show brightness depressions at higher frequencies range from 327 to 432 MHz and are not easily discernible near 250 MHz (Mercier and Chambe, 2009). In studying the quiet corona at frequencies from 150 to 450 MHz using the *Nançay Radioheliograph*, Mercier and Chambe (2012) reported low-latitude CHs to be darker near the disk center at higher frequencies and less visible as frequency decreases near or below 200 MHz. They found that CHs may become brighter than their surroundings at lower frequencies. Using the Potential Field Source Surface model, they revealed that CHs are regions of open magnetic field lines at their observing frequencies of 150, 164, and 432 MHz. On the other hand, CHs are regions of brightness enhancement at 80 MHz (Lantos et al., 1987).

Thus, the characteristic feature of CHs from radio observations is that near

the disk center they are seen as darker regions at higher frequencies and as brighter regions at lower frequencies (Lantos et al., 1987; Mercier and Chambe, 2012). Figure 1.12 shows such a CH. McCauley et al. (2017) reported the transition of a disk-centered CH from being darker at higher frequencies to being brighter at lower frequencies using the MWA observations from 80 to 240 MHz. They added that the transition frequency took place near 120 MHz for that CH.

The second Chapter of this thesis (Rahman et al., 2019) investigates this dark-to-bright transition of CHs in detail. It follows on from McCauley et al. (2017) by observing four CHs near the disk center using the MWA at frequencies ranging from 80 to 240 MHz, confirming and examining in detail the claim that CHs become brighter at lower frequencies and darker at higher frequencies. The dark-to-bright transitions of these CHs were smooth and did not occur at the same frequency for all the CHs. Some CHs had their transition frequency at 120 MHz with others at 132 MHz. We came to the conclusion that this dark-to-bright transition of CHs is due to the refraction and propagation effects caused by density inhomogeneities, as suggested earlier by Alissandrakis (1994). The orientation of a CH radial magnetic field relative to an observer may affect in principle whether the CH is radio-dark or radio-bright at low frequencies, being radio-bright when CHs are near disk center and radio-dark near the limb (Golap and Sastry, 1994). Thus we suggest that radio CHs can be observed as darker regions near the disk center at higher frequencies and as brighter regions at lower frequencies but that CHs are always darker near the limb at any frequency.

1.10 Solar Radio Bursts

Solar radio bursts are non-thermal emissions produced from rapidly varying phenomena of the solar corona like active regions, solar flares, CMEs, prominences, and shocks. They are characterized by a coherent emission mechanism, that is different from the incoherent emission mechanisms relevant to CHs and the quiet Sun. The distinguishing feature of coherent emission from incoherent emission is a high brightness temperature ($\geq 10^7$ K) (Melrose, 2009), much greater than the plasma's thermal temperature ($\leq 10^7$ K). Radio bursts are polarized or unpolarized depending on the magnetic field configurations and dispersion and scattering effects they may face during their release from the source regions.

There are five types of solar radio bursts that are classified according to their drift rates and appearance on dynamic spectra: type I, II, III, IV, and V bursts (Wild and McCready, 1950). Figure 1.13 is a schematic example of a dynamic spectrum for these radio bursts. The ranges of frequencies, frequency drift rates, and basic classification of a burst can be found easily from the dynamic spectrum. The brightness temperatures of bright type I−V radio bursts in the corona and solar wind are non-thermal (above $\simeq 1{-}3{\times}10^6$ K) ranging from 10^8 K to 10^{15} K (Kirk et al. 1994, p-194).

Type I Bursts/Noise Storms: Type I emission occurs in noise storms and can involve continuum emission and discrete bursts which are not associated with flares (Melrose, 2009). This emission can be frequently observed in the solar corona at meter wavelengths typically in the frequency range $\approx 50{-}500$ MHz (McLean and Labrum 1985, p-415; Hamidi and Shariff 2019). Noise storms can last for days to weeks, varying slowly or abruptly, and have low frequency drift rates (≈ 5 MHz s^{-1}). Noise storms are strongly circularly polarized and so are usually interpreted in terms of emission near f_p (Kirk et al., 1994).

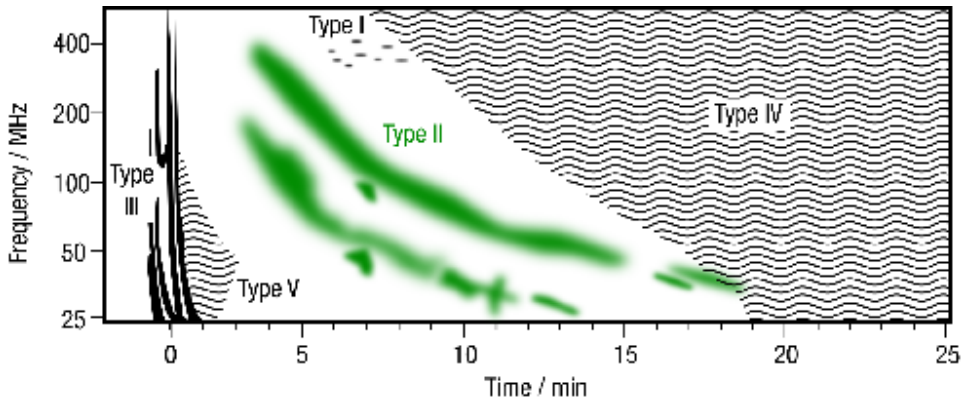

Figure 1.13: Schematic example of type I, II, III, IV, and V radio bursts in dynamic spectrum. The spectrum shows frequency drift from high to low as a function of time (Ganse et al., 2012).

Type II Bursts/Slow Drifting Bursts: Type II bursts drift slowly from high to low frequency with a drift rate $\approx$ 1 MHz s^{-1} that is slightly slower than type I bursts and much slower than type III bursts (Nelson and Melrose 1985, p-337). These type of bursts are associated with shock waves produced by a solar flare or coronal mass ejection and last for a few minutes. They can be observed in the frequency range $\approx$ 40−240 MHz for the corona and then also down to $\simeq$ 20 kHz for interplanetary type II bursts (Cairns et al., 2000). It is noted that type IIs are not produced by all shock waves. These bursts have weak circular polarization ($\leq$ 10% usually) or even have no polarization (Nelson and Melrose, 1985). They are usually interpreted in terms of plasma emission near f_p and $2f_p$, as reviewed elsewhere (Nelson and Melrose, 1985; Cairns, 2011).

Type III Bursts/Fast Drifting Bursts: Type III bursts drift rapidly from high to low frequency at a drift rate $\approx$ 100 MHz s^{-1} which is much faster than type II bursts. They are associated with a stream of high speed electrons released from the magnetic reconnection site of solar flares and propagating outward through the solar corona at speeds $\geq$ 0.1c. These bursts are of three types: 1) isolated type IIIs, 2) groups of type IIIs, and 3) type III storms. Type

III bursts are usually relatively weakly circularly polarized with a maximum degree of circular polarization ≈ 50% (Suzuki and Sheridan, 1977). Details of the characteristic properties of type III bursts are reviewed by many authors (Melrose et al., 1980; Melrose, 1989a,b; Robinson and Cairns, 1998; Reid and Ratcliffe, 2014; Cairns et al., 2018).

Type IV Bursts/Broad-band Continuum Emissions: Type IV bursts involve smoothly varying, broadband, continuum emission (Kundu, 1962). They are weakly polarized and last for a few minutes to a few hours. Type IV bursts occur at centimeter, meter, and decameter wavelengths. The origin of these type of bursts is uncertain. It is thought that they are produced by the gyro-synchrotron emission processes (McLean and Labrum 1985, p-361). Some type IV bursts are also considered to be produced by the plasma emission process.

Type V Bursts/Continuum Meter Wave Emissions: Type V bursts are often referred to as continuum emissions. They last for a few seconds to a few minutes. They are observed at meter wavelengths following type III bursts. Type V bursts are usually observed at frequencies near or less than 200 MHz (Weiss and Stewart, 1965). They are very weakly polarized emissions (≈ 0.1%) with broadband spectra as compared to type IIIs (Zheleznyakov and Zaitsev, 1968).

Besides these, complex bursts such as U- and J-type bursts are sometimes seen in the radio spectrograms (Maxwell and Swarup, 1958). U bursts initially drift like type III bursts but later drift in the reverse direction so as to appear like an inverted "U" in the dynamic spectrum. J-type bursts are similar to the U-type bursts but do not exhibit the reverse drift.

We will emphasize only type III radio bursts in later Sections of this Chapter and in Chapters 3 and 4. Specifically, type III solar radio bursts and their theory are presented in Sections 1.11 and 1.11.1, respectively. A more extensive summary of their properties from an observational point of view is detailed in

Section 1.11.2.

1.11 Type III Solar Radio Bursts

Type III solar radio bursts are non-thermal radio emissions produced by semirelativistic electron beams propagating through the corona and solar wind from magnetic reconnection sites activated in solar flares. It is well known that type III bursts involve emission at the fundamental and second harmonic of the electron plasma frequency (Dulk and Suzuki, 1980; Suzuki and Dulk, 1985; Kirk et al., 1994). Their drift rates vary from burst to burst. Type IIIs can be observed from kHz frequencies (Krupar et al., 2011) up to frequencies of 8 GHz (Ma et al., 2012). Some type IIIs drift from higher starting frequencies near 900 to 200 MHz (Benz et al., 2009) and others begin to drift at relatively lower frequencies below 50 MHz (Ganse et al., 2012). *Coronal* type III bursts are those which have frequencies above about 20 MHz. Besides, *interplanetary* type III bursts originate when the electron beams escape along the open field lines and continue to stimulate Langmuir waves in the solar wind plasma. They have frequencies from about 10 MHz down to frequencies of 20 kHz and below near 1 AU (Lin et al., 1973; Leblanc et al., 1998).

Figure 1.14 is a dynamic spectrum of type III bursts on October 21, 2011, near 12:56 UT. These type III bursts cover the frequency range from 400 to 10 MHz. We also see multiple type IIIs starting from ≈ 200 MHz down to 30 MHz from 12:56:20 to 12:56:50 UT.

Type III bursts are precious diagnostic tools for understanding the acceleration, propagation, and preservation mechanisms of electron beams propagating through the coronal and solar wind (Lin, 1974). Moreover, the density profile of the ambient plasma can also be traced out by the accelerated electron beams via their frequency drift rate and source locations (Reid and Ratcliffe, 2014).

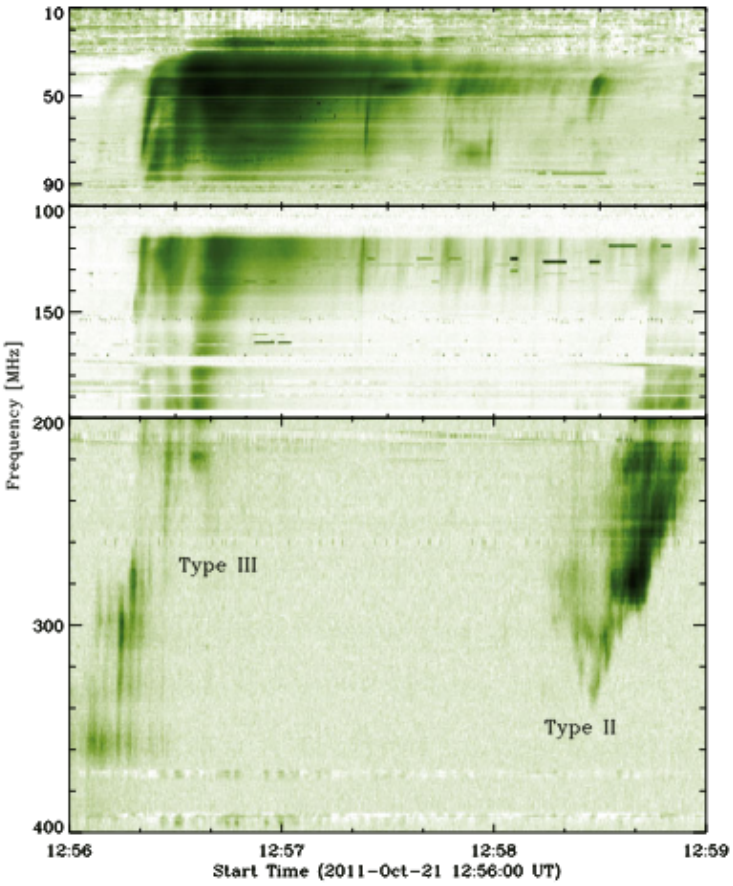

Figure 1.14: Type III radio bursts observed by Zucca et al. (2012) on October 21, 2011 at Rosse Solar Terrestrial Observatory (RSTO). The dynamic spectrum shows multiple type IIIs over the entire frequency range, as well as a possible type II burst between 140 and 330 MHz.

The important observational properties of type III bursts include the frequency drift rate, motion, fundamental and harmonic structures, circular polarization, and brightness temperature. These properties are measured in Chapters 3 and 4 below using data from the MWA.

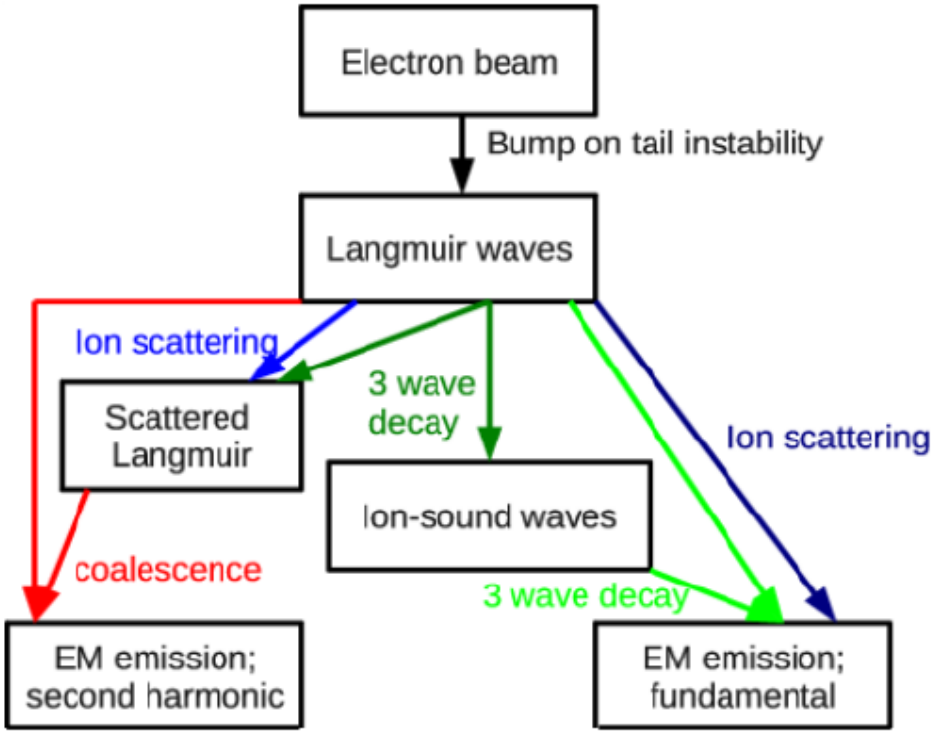

Figure 1.15: A flow diagram depicting the steps in modern versions of plasma emission (Melrose, 2009; Cairns, 2011; Reid and Ratcliffe, 2014).

1.11.1 Theory of Type III Radio Bursts

The first detailed theory of type III bursts was given by Ginzburg and Zheleznikov (1958). Modern versions of the emission are outlined schematically in Figure 1.15 (Melrose, 2009; Cairns, 2011; Reid and Ratcliffe, 2014): it involves four steps: 1) generation of Langmuir waves (plasma oscillations) in the background plasma by the electron beam through the bump-on-tail instability, 2) production of fundamental plasma emission by scattering of Langmuir waves into transverse waves by either thermal ions or ion acoustic waves, 3) production of backscattered Langmuir waves by either scattering off thermal ions or the electrostatic decay process which also produces ion acoustic waves, and 4) generation of second harmonic plasma emission when two Langmuir waves

coalesce to form a transverse wave.

The modern picture (Melrose, 1982; Cairns, 1987a,b, 1988; Cairns and Robinson, 1992; Robinson et al., 1993; Li et al., 2005; Cairns, 2011; Graham and Cairns, 2013) is that fundamental emission occurs due to the decay of beam-driven Langmuir wave into a radio wave and an ion sound wave, $L \rightarrow T + S$ (where L, S, and T denote Langmuir, ion sound, and transverse waves respectively), stimulated by the electrostatic decay process in which a beam-driven Langmuir wave decays into a backscattered L' wave and an ion sound wave via $L \rightarrow L' + S$. The second harmonic emission is due to the coalescence process $L + L' \rightarrow T$. Each step of the theory has been updated several times as ideas based on underlying plasma theory are established, as reviewed by Robinson and Cairns (2000), Melrose (2009), and Cairns (2011).

1.11.2 Radio Observations of Type III Bursts

Many authors have studied the drift rate, motion, brightness temperature, fundamental and harmonic structures, and polarization properties of type III bursts in the past few decades using different radio instruments. We now briefly review the characteristic properties of type III bursts from an observational point of view.

Frequency Drift Rate: The defining property of type III bursts as compared to the other solar radio bursts is their high drift rate df/dt. How the drift rate is calculated varies, with some authors using the drift rate near the burst onset and other authors using the drift rate of the burst near peak flux at each frequency (Reid and Ratcliffe, 2014). The frequency drift rate of type III bursts between 3.5 MHz and 50 kHz was studied by Alvarez and Haddock (1973b). They deduced an empirical formula for the drift rate $\mathrm{df/dt} = -0.01\ f^{1.84}$ MHz s^{-1}. Melnik et al. (2011) established a linear dependence of the drift rate with

frequency (df/dt $\propto f$) for lower frequency type IIIs ranging from 30 to 10 MHz, with drift rate similar at 10 MHz to Alvarez and Haddock (1973b) but smaller at 30 MHz. In order to incorporate higher frequency drift rate studies, Aschwanden et al. (1995) investigated type III bursts drift rate between 200 MHz and 3000 MHz, and they found an average drift rate df/dt = 0.01 $f^{1.4}$ MHz s^{-1}, which is smaller than expected from the Alvarez and Haddock (1973b) drift rate relation.

Decay Time: The decay time t_d of type III bursts is the time scale obtained from the exponential decay of the peak intensity of bursts at a particular frequency f. Coronal type III bursts have smaller decay times than interplanetary type III bursts (Alvarez and Haddock, 1973a; Evans et al., 1973; Robinson et al., 1993; Robinson and Cairns, 1998). Usually, t_d varies inversely with f, as described next. In particular, Evans et al. (1973) observed 35 simple type III bursts from 2.8 MHz to 67 kHz and showed that the decay time varied as $t_d = 2.0 \times 10^8 f^{-1.09}$ using a least squares fit to the data. In the same year, Alvarez and Haddock (1973a) estimated that $t_d = 10^{7.7} f^{-0.95}$ for type III bursts in the frequency range 200 MHz to 50 kHz. In the 3-5 GHz range, the decay time of type IIIs is roughly inversely proportional to the frequency $t_d \propto f^{-1}$ (Staehli and Benz, 1987). More recently, Robinson and Cairns (1998) summarised observations and then developed a theoretical model for the decay times for coronal and interplanetary type III bursts at 25 MHz and 25 kHz, respectively: they found that $t_d \propto f^{-1.1\pm0.1}$. Their model for the decay considers the diffusion and absorption (by linear mode conversion) of fundamental radiation by density turbulence, with the frequency dependence coming from radial variations in the plasma density and turbulence.

Brightness Temperature: Type III bursts have high brightness temperature T_b that can vary from 10^6 K to even as high as 10^{15} K (Suzuki and Dulk, 1985). The brightness temperature can be calculated from the burst flux density and

source size, using the standard expression e.g., (Cairns, 1986):

$$T_b = \frac{V_\phi^2}{2k_B f^2} \frac{F(f)}{\Delta\Omega}, \tag{1.6}$$

where V_ϕ is the phase speed of the radio waves at the observer at frequency f, k_B is Boltzmann's constant, and $F(f)$ is the frequency dependent flux density. The source solid angle $\Delta\Omega = A/4\pi r^2$ where A is the burst source area seen by the observer, and r = 1 AU is the distance from burst source to observer. It is noted here that the phase speed is equivalent to the speed of light when $f >> f_p$. As noted before, the high brightness temperatures of most type III bursts are due to their production of highly non-thermal levels of Langmuir waves and their conversion into radio emissions, both of which involves collective or coherent emission processes.

Saint-Hilaire et al. (2013) performed a statistical survey of 10,000 type III radio bursts using the *Nançay Radioheliograph* for a decade at 150 to 450 MHz and studied the peak brightness temperatures. They found that the brightness temperature varied with f as $T_b \propto f^{-1.8}$. They also showed that T_b varied from 10^6 K to 10^{10} K for all six frequencies considered. For a few burst events, they found T_b near 10^{11} K. There is a trend that at lower frequencies, T_b increases as frequency decreases up to 1 MHz and then T_b either decreases or remains constant (Dulk et al., 1984). Type III emission at the fundamental is thought to generate higher T_b than that of second harmonic emission (Dulk et al., 1984; Melrose, 1989a).

Circular Polarization: The polarization properties of type III bursts have attracted considerable interest from the solar physics community. Theoretically, fundamental type III emissions are 100% circularly polarized. But from the observational point of view, they are not more than 60% circularly polarized for fundamental emission. On the other hand, the harmonic emission is weakly

polarized or unpolarized (Kirk et al. 1994, p-194). We note that some type IIIs may not be polarized at all.

We now detail the work of some researchers on the polarization properties of type III bursts. Mercier (1990) studied the degree of circular polarization of type III solar radio bursts observationally using the *Nançay Radioheliograph* from 164 to 435 MHz. He found that the degree of circular polarization (maximum 23%) increases as the frequency increases on average. He also studied the total and circularly polarized fluxes for a couple of burst events and showed that the circularly polarized flux has a narrower time profile than the total flux at 164 MHz and has a peak 0.2 s before that of the total flux for one burst event on June 30, 1988. This event was an extreme case and the peak in the circularly polarized flux did not lead the peak in the total intensity for all the isolated type IIIs considered.

It is well established that the polarization can be high when type III bursts originate near the solar disk center and that relatively low polarization is obtained for type IIIs originating near the solar limb (Suzuki et al., 1980; Kirk et al., 1994). For type I bursts or noise storms, the same trend of position dependence of polarization is obtained: higher polarization near the disk center and lower polarization when sources are closer to the solar limb (Aschwanden, 1986).

Source Motion: We know that the energetic electron beams originating during magnetic reconnection site in solar flares are the ultimate sources of type III bursts (Cairns et al., 2018), and these electrons have typical speeds $\approx$ c/3 in the corona, which obviously can vary from burst to burst. Imaging studies of these high speed burst sources have recently become available with good frequency resolution using the *Murchison Widefield Array* (MWA) (McCauley et al., 2017; Mohan et al., 2019). Recently, McCauley et al. (2017) observed type III bursts at 80 to 240 MHz using the MWA and studied a splitting motion

of burst source regions, in which a single source at high frequency separates into two components at lower frequencies (from 135 MHz to 80 MHz) with an average speed ≈ 0.28 c. Their interpretation is that this is due to gradient of magnetic field connectivity that the burst driven electron beams move into. One year later, McCauley et al. (2018) studied coronal density profiles for three type III burst sources using the MWA. They estimated that the electron beam speed ranged from 0.2 to 0.6 c (where c is the speed of light) using the time- and frequency-varying burst source positions. Morosan et al. (2014) studied spectral and spatial characteristics of multiple type III bursts using the LOw Frequency ARray (LOFAR) at frequencies ranging from 30 to 60 MHz, and reported high radial motions of type IIIs which were between 0.2 and 0.5 c.

Recently, Cairns et al. (2018) investigated the detailed connections between type III bursts, magnetic reconnection, x-ray events, and solar flares. They established a causal link between magnetic reconnection events and type III bursts, tracing the electron beams producing type IIIs to magnetic reconnection sites identified in SDO/AIA data which sometimes produced x-ray events and sometimes type IIIs.

Source Size: Saint-Hilaire et al. (2013) surveyed 10,000 type III radio bursts using the *Nançay Radioheliograph* for a decade at 150 to 450 MHz and observed full width at half maximum (FWHM) rms burst source sizes ≈ 15 and ≈ 5.5 arcmin per day at 150.9 and 432 MHz, respectively. Very recently, Mohan et al. (2019) have reported spectroscopic imaging study of weak type III burst source areas using data from MWA in the frequency ranges from 111 to 126 MHz and investigated the second scale quasi-periodic oscillatory behaviour in burst source sizes with time. They estimated source areas that are between 12 and 33 arcmin^2 on average at that frequency range. Earlier investigations of burst source sizes were performed by Dulk and Suzuki (1980). They found burst source sizes on average (half widths to 1/e brightness) of 11 arcmin at 80

MHz and 20 arcmin at 43 MHz. Burst source sizes are ≈ 1 AU at 20 kHz for interplanetary type IIIs (Lin et al., 1973). These data suggest that burst source sizes increase as frequency decreases.

1.12 Structure of the Thesis

This introductory chapter (**Chapter 1**) briefly described the solar corona, quiet Sun, active regions, solar flares, and coronal holes (CHs). It then described the magnetoionic theory, the gyromagnetic, bremsstrahlung, and plasma emission mechanisms, the generation and propagation of radio waves in the corona, the FORWARD software package and MAS model, the *Murchison Widefield Array* (MWA) radio telescope, solar radio bursts, and their classifications. Thereafter, the observations, theory, properties of CHs, type III solar radio bursts were described, leading up to recent work using the MWA and other instruments.

Chapter 2 (Rahman et al., 2019) demonstrates the dark-to-bright transitions of four radio CHs using the data from MWA in the frequency range from 80 to 240 MHz. The observational results are then compared with synthetic images obtained from FORWARD. CH density and temperature parameters are then extracted from the MAS-FORWARD model and compared with the observations, finding significant differences. The dark-to-bright transitions of these CHs are then interpreted in terms of refraction and propagation effects.

Chapter 3 demonstrates novel imaging and circular polarization measurements of multiple type III radio bursts using data from MWA in the frequency range 80 to 240 MHz and then describes the position dependence of the polarization fractions near the onset and peak of bursts. We find larger polarization fractions for the burst source near burst onset, which is interpreted in terms of fundamental emission being dominated and then relatively smaller polarization fraction near the time of burst maximum intensity, corresponding to a mixture of fundamental

and harmonic plasma emission. During the decay phase the fundamental component dominates again, becoming weaker with time due to scattering effects. This pattern of fundamental, fundamental and harmonic, and then fundamental emission with time is consistent with the interpretations of Dulk et al. (1984), Robinson et al. (1994), and Robinson and Cairns (1998). We study the total intensity (Stokes I), circularly polarized intensity (Stokes V), and polarization fraction ($\mid V \mid/I$) profiles of a type III event with no source motion and two events with source motion as a function of position at times when the intensity of bursts is maximum. For the burst event with no source motion we find symmetric profiles for Stokes $\mid V \mid/I$, but we find asymmetric $\mid V \mid/I$ profiles for those burst events which have source motion. We argue that this is due to the motion of the burst source. The total intensity and circularly polarized fluxes of the bursts are then analyzed as a function of time. The total intensity is found to large than polarized flux. The time-varying images, relative motion and spatio-temporal profiles of burst sources are then studied as functions of frequency and time. We find speeds 0.23 and 0.25 c for two burst sources along the direction of source motion. Finally, the decay time (t_d) as a function of frequency (f) is measured for multiple events, finding $t_d \propto f^{-2.0\pm0.1}$ from 80 to 240 MHz and larger t_d as compared with low-frequency observations ($t_d \propto f^{-1.1\pm0.1}$).

Chapter 4 presents analyses of low-frequency observations of type III solar radio bursts using the MWA from 80 to 240 MHz. Specifically, near times at burst maximum intensity, the burst source sizes, flux densities, and brightness temperatures are studied for 10 type III events in both total (Stokes I) and polarized intensity (Stokes I) images. We find that the source area A increases as f decreases and varies as $A \propto f^{-2.4\pm0.4}$ and $A \propto f^{-2.6\pm0.4}$ in both Stokes I and Stokes V images, respectively, whereas the MWA beam area varies as $A \propto f^{-2.5\pm0.2}$. We propose that the burst source sizes once separated from the

effects of the MWA beam, do not support scattering (which predicts $A \propto f^{-4}$) as the primary physical effect determining the observed source sizes. We interpret the observed area changes as due to divergence of open magnetic field lines, which causes the source sizes to increase at lower frequencies and larger heights. On average, flux densities are also found to increase as frequency decreases. We find total fluxes (in Stokes I) on average 550 and 50 SFU at 80 and 240 MHz, respectively, whereas logarithmic flux density of type IIIs ranges from 0.2 to 4.8 at 80 MHz (Dulk and Suzuki, 1980). Our flux values lie within the range of their flux values. The brightness temperatures (T_b) decrease as a function of increasing frequency and do not have dependency on the source's position although we analyse a small number of burst events. We obtain a maximum T_b $4{\times}10^{11}$ K at 80 MHz and a minimum T_b $1.2{\times}10^{8}$ K at 240 MHz, which are consistent with previous observations ($\log T_b$: $7-11.5$ at 80 MHz) made by Dulk and Suzuki (1980). We argue that divergence of open field lines is a viable process for increasing source sizes as the frequency decreases.

Chapter 5 contains a final summary and suggestions for future work.

Chapter 2

On the Relative Brightness of Coronal Holes at Low Frequencies

Abstract

We present low-frequency ($80 - 240$ MHz) radio observations of coronal holes (CHs) made with the *Murchison Widefield Array* (MWA). CHs are expected to be dark structures relative to the background corona across the MWA's bandwidth due to their low densities. However, we observe that multiple CHs near disk center transition from being dark structures at higher frequencies to bright structures at lower frequencies ($\lesssim 145$ MHz). We compare our observations to synthetic images obtained using the software suite FORWARD, in combination with the Magnetohydrodynamic Algorithm outside a Sphere (MAS) model of the global coronal magnetic field, density, and temperature structure. The synthetic images do not exhibit this transition, and we quantify the discrepancy as a function of frequency. We propose that the dark-to-bright transition results from refraction of radio waves into the low density CH regions, and we develop a qualitative model based on this idea and the relative optical depths inside and outside a CH as a function of frequency. We show that opacity estimates based on the MAS model are qualitatively consistent with our interpretation, and we conclude that propagation and relative absorption effects are a viable explanation for the dark-to-bright transition of CHs from high to low frequencies.

2.1 Introduction

Coronal holes (CHs) are low-density regions in the inner solar corona that were first quantitatively observed by Waldmeier (1956). CHs have open magnetic field lines that allow mass and energetic particles to escape from the Sun, which produces regions of low density as compared to closed-field regions. Polar CHs are found primarily near solar minimum whereas the low-latitude CHs that we are interested in form near solar maximum. The study of CHs is a crucial part of solar physics research because CHs are major factors in the mass and energy flows of the corona, and their associated high-speed wind streams are responsible for a significant fraction of major geomagnetic storms, especially near solar maximum (Cranmer, 2009).

The nature of CHs in radio observations remains unclear. Some low frequency observations find CHs to be regions of brightness depression relative to the background (Alissandrakis, 1994; Lantos and Alissandrakis, 1999) whereas others have reported CHs as regions of brightness enhancement (Lantos et al., 1987). Specifically, based on *Culgoora radioheliograph* data, Sheridan and Dulk (1980) reported that CHs appeared darker near disk center at 160 MHz and brighter than their surroundings at 80 MHz. They added that CHs are larger at 80 MHz than at 160 MHz. Earlier, Dulk and Sheridan (1974) used the *Culgoora radioheliograph* to measure the brightness temperatures of CHs as 0.8×10^6 and 0.6×10^6 K at 80 and 160 MHz, respectively. They also compared their coronal radio maps with the EUV maps of Fe XV at 284 $\mathring{A}$ and found brightness depressions as well as probably lower brightness temperatures in CHs compared with the quiet Sun.

When CHs are at the limb, they always appear as brightness depressions at all frequencies. Dulk et al. (1977) found CHs to be dark near the northern solar limb at 10.7 GHz, while Shibasaki et al. (1977) also found CHs as regions

of brightness depressions near the solar limb at 3.8 GHz. Later, Dulk (1985) reviewed quiescent Sun's radio emission at 10 GHz and reported that CHs are bright on the disk center at 100 MHz and dark at 1.4 GHz. While studying low brightness temperature regions in the quiet corona, Lantos et al. (1987) observed a CH as an intensity depression at 169 MHz using the *Nançay Radioheliograph*, in agreement with some other observations. However, Lantos (1999) reviewed low-frequency observations of large-scale structures such as CHs, coronal plateaus, and the background quiet Sun with different radioheliographs and found that CHs are also reported as regions of brightness enhancements near the disk center.

Thus CHs may appear either as intensity enhancements or depressions when observed at low frequencies near disk center, and they are always reported as depressions when observed at the limb. The mechanism by which a low-density CH region may appear as a low-frequency brightness enhancement is unclear. Alissandrakis (1994) suggested that opacity and refraction effects caused by density inhomogeneities are responsible for the radio corona being brighter at lower frequencies and darker at higher frequencies. These propagation and refraction effects can lead a CH structure to transition from being relatively dark to relatively bright from high to low radio frequencies. Alternatively, Golap and Sastry (1994) suggested that the orientation of a CH radial magnetic field relative to an observer may affect whether the CH is radio-dark or radio-bright at low frequencies, being radio-bright when near disk center and radio-dark near the limb.

Previous radio studies of CHs from ≈ 10.7 GHz to ≈ 80 MHz (Dulk and Sheridan, 1974; Dulk et al., 1977; Shibasaki et al., 1977; Sheridan and Dulk, 1980; Lantos et al., 1987; Alissandrakis, 1994) demonstrated that CHs are dark at higher frequencies and may occasionally be relatively bright features at the lowest frequencies, but the available instrumentation did not provide

simultaneous coverage across the bandwidth over which this transition occurs. Mercier and Chambe (2009) observed radio images of the corona at 150−450 MHz using the *Nançay Radioheliograph* and showed that some CHs have low brightness temperature and intensity depressions near the disk center at 432 MHz. They also found those CHs were not clearly distinguishable at frequencies less than 250 MHz, as their brightness becomes comparable to the background at the low end of the Nançay bandwidth.

Recently, McCauley et al. (2017) used the *Murchison Widefield Array* (MWA) in the range 80−240 MHz to study type III bursts but also found a gradual transition of a CH from being dark relative to the background at high frequencies to being bright at low frequencies. This dark-to-bright transition took place around 120 MHz for that CH. Motivated by these works, we first use the MWA at 12 frequency channels from 80 to 240 MHz for four CHs near disk center. In each case, a dark-to-bright transition is observed from higher to lower frequencies. We then analyze one of the events more quantitatively and develop a qualitative model for the observed dark-to-bright transition.

The rest of the Chapter is organized in the following sections: the MWA radio observations and results are presented and then compared with model images in Sections 2.2 and 2.2.1, respectively. The dark-to-bright transition of CHs is quantified in Section 2.2.2. A counter example of the dark-to-bright transition of a CH is presented in Section 2.2.3. Plasma density and temperature profiles for a CH and the surrounding corona are extracted from a global magneto-hydrodynamic (MHD) model in Section 2.3. A qualitative model involving propagation effects and refraction is developed in Section 2.4. Specifically, Section 2.4.1 contains an optical depth calculation and Section 2.4.2 describes a qualitative model based on refraction to explain the dark-to-bright transition of CHs. Finally, the discussion and conclusions are presented in Section 2.5.

2.2 MWA Radio Observations and Results

The *Murchison Widefield Array* (MWA) is a low-frequency interferometer in Western Australia (Lonsdale et al., 2009; Tingay et al., 2013a). Technical details of MWA and its overall design are described by Tingay et al. (2013a). The MWA science targets are reported by Bowman et al. (2013). The instrument is composed of 128 "tiles" each containing 16 dual polarization dipole antennas. The total bandwidth is 30.72 MHz, which can be distributed across the range 80 to 300 MHz, and the time and frequency resolutions are 0.5 s and 40 kHz, respectively (Tingay et al., 2013a). Significant amounts of solar research have been done by many authors using MWA observations (Tingay et al., 2013b; Oberoi et al., 2014, 2017; Mohan and Oberoi, 2017; Suresh et al., 2017; McCauley et al., 2017, 2018; Cairns et al., 2018).

In our observations of CHs, we observe at 12 frequencies ranging from 80 to 240 MHz. The MWA data are recorded with 0.5 s time and 40 kHz frequency resolutions, which we average across 2.56 MHz bandwidths to produce 0.5 s images at 80, 89, 98, 108, 120, 132, 145, 161, 179, 196, 217, and 240 MHz. We used WSClean (w-stacking clean) (Offringa et al., 2014) for imaging with a Briggs -2 (Briggs, 1995) weighting scheme in order to emphasize spatial resolution. The synthesized beam sizes range from $\approx$ 2.8 arcmin at lower frequencies to less than 1 arcmin at higher frequencies. Our data are reduced in the same manner as described by McCauley et al. (2017) and McCauley et al. (2018).

Figure 2.1 presents MWA radio images of CH structures for four periods: near 03:31 UT on 28 August 2014, 05:15 UT on 31 August 2015, 05:13 UT on 21 September 2015, and 02:29 UT on 11 November 2015. The data come from $\approx$ 5 min observing periods, from which we obtain 592 images *per* frequency channel. Each observing window also includes one or more type III bursts. To

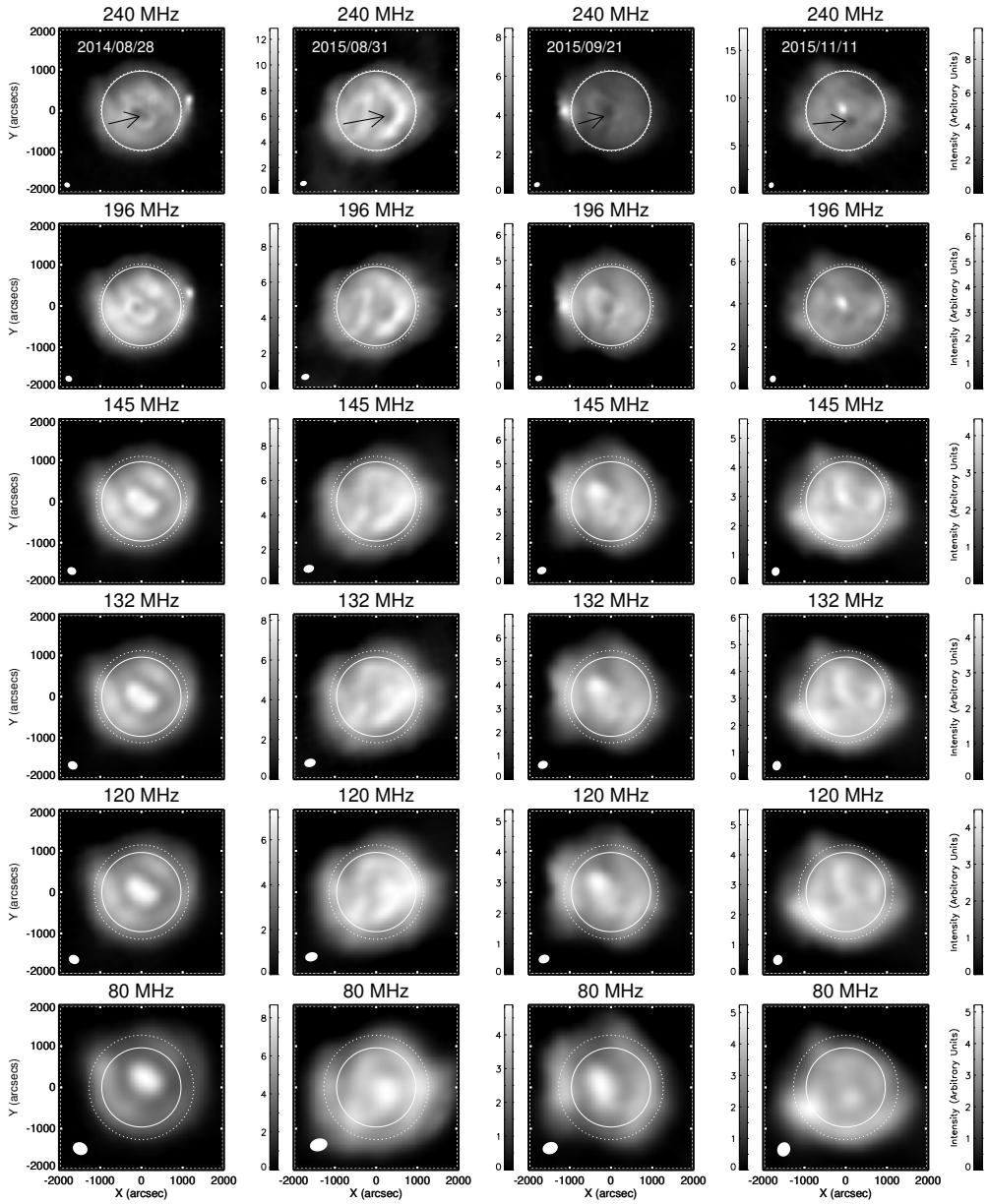

Figure 2.1: Dark-to-bright transition of CHs in MWA radio images for four periods: 03:31 UT on 28 August 2014 (*first column*), 05:15 UT on 31 August 2015 (*second column*), 05:13 UT on 21 September 2015 (*third column*), and 02:29 UT on 11 November 2015 (*fourth column*). The MWA images are plotted with linear scaling. The arrow signs in the top panels indicate the CH locations. The inner solid circles indicate the optical disk and the outer dotted circles indicate the height of the plasma layer for each frequency given the Newkirk (1961) density model. The ellipses at the lower left corners indicate the MWA synthesized beam sizes. Color bars refer to the intensity in arbitrary (uncalibrated) units.

produce higher signal-to-noise images of the quiescent corona, we average all of the images for a given frequency channel outside of burst periods. To exclude burst images from the average, we exclude all images that have a total intensity greater than 105% of an image manually identified as non-burst. Depending on the event and frequency, our final images are averages of between 409 and 541 individual 0.5 s integrations.

The six images in each column of Figure 2.1 show one of the four different CHs at six frequencies: 80, 120, 132, 145, 196, and 240 MHz. Each example clearly shows a dark-to-bright transition of a specific CH from high to low frequencies. Specifically, the CH structures are relatively dark at higher frequencies, from 145 MHz up to 240 MHz, and they become relatively bright as the frequency decreases from 145 MHz to 80 MHz. Each CH is observed as a region of depressed brightness compared with the surrounding corona above 145 MHz (up to 240 MHz) but a brightness enhancement from 145 MHz to 80 MHz. Figure 2.1 indicates that the transition frequency of CH structures from being darker to brighter is not the same for all CHs. Some CHs show the transition near 145 MHz while others show the transition near 120 MHz.

2.2.1 Comparisons Between Observations and Model Images

We now compare the radio CH structures with 193$\mathring{A}$ *Atmospheric Imaging Assembly* (AIA: Lemen et al. 2012) images to show the locations of the CH regions in both datasets. In order to accomplish this, the 240 MHz MWA intensity contours for CH regions are plotted on top of the AIA images in Figure 2.2 for the four observational events shown in Figure 2.1. The plotted contours are the inverse intensity, so that the radio contours exhibit a peak where the intensity is the lowest. The radio and AIA CH locations clearly agree very well.

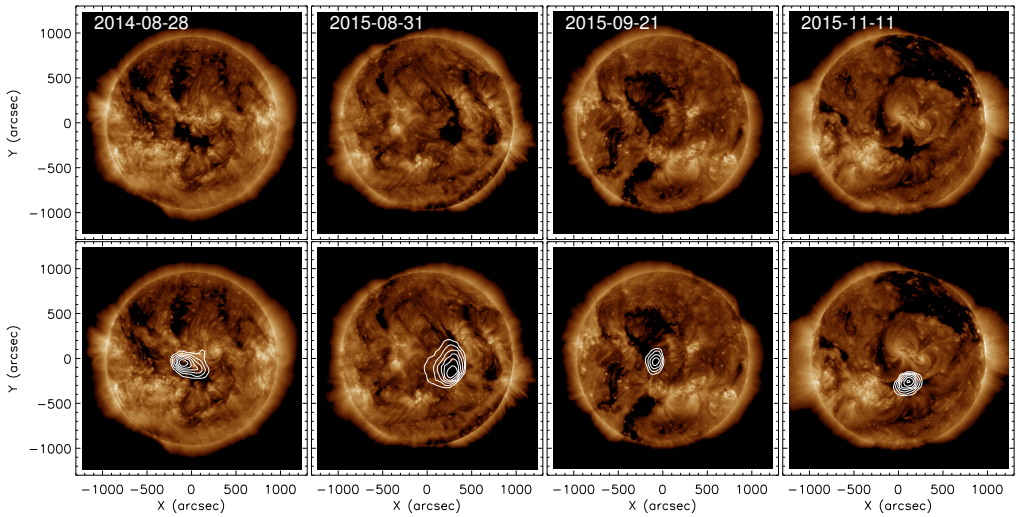

Figure 2.2: *Top*: AIA images of the corona at 193$\mathring{A}$ for the four days shown in Figure 2.1. The AIA images are plotted with log scaling. *Bottom*: 240 MHz MWA contours of inverse intensity on top of the AIA images. The columns in this montage are in the same order as in Figure 2.1.

We next compare the MWA CH structures with synthetic images generated using FORWARD, a software package that can compute the thermal bremsstrahlung and gyroresonance emission expected from a specific magnetic field and thermodynamic model. We note that FORWARD does not include any propagation effects like refraction or scattering. See Gibson et al. (2016) for details on those calculations and the other capabilities of the package. Our implementation uses the Magnetohydrodynamic Algorithm outside a Sphere (MAS, Lionello et al. 2009) model to specify the plasma and magnetic field structures for our events.

The MWA and synthetic images of the CH on 31 August 2015 are shown in the top and bottom panels of Figure 2.3, respectively. At higher frequencies (above 145 MHz), the agreement between the observed and model-predicted CH images is best. Figure 2.3 shows that the discrepancies between the observations and model are the greatest at low frequencies. Specifically, the CH becomes significantly brighter than its surroundings at 80 MHz in the MWA observation,

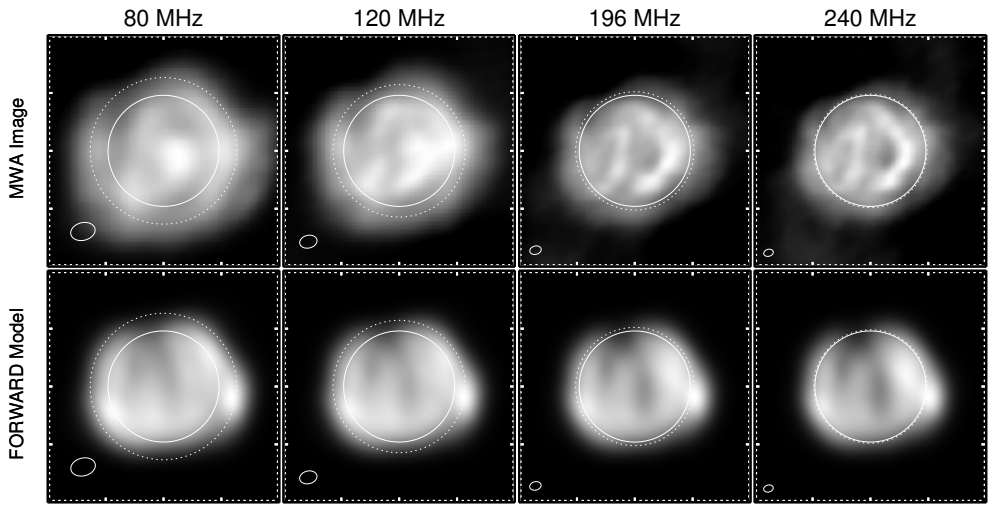

Figure 2.3: *Top*: MWA radio images of the CH at 05:15 UT on 31 August 2015. *Bottom*: FORWARD synthetic images based on the MAS model and convolved with the MWA beam. The inner solid circles indicate the optical disk and the outer dotted circles indicate the height of the plasma layer for each frequency given the Newkirk (1961) density model. The ellipses at the lower left corners indicate the MWA synthesized beam sizes.

which is not consistent with the model. However, the CH structure is relatively dark at 240 MHz in both the MWA observation and MAS model prediction. The crucial point is that the MAS–FORWARD predictions do not show the dark-to-bright transition for CHs observed in the MWA data.

2.2.2 Quantification of Dark-to-bright Transition

In order to quantify the dark-to-bright transition of a radio CH with frequency, we use the MWA data centered at 05:15 UT on 31 August 2015 and at 05:13 UT on 21 September 2015. We take a slice through each of the CHs, which are shown in Figure 2.4. Figure 2.5 presents normalized intensity profiles as a function of distance along the slice for all twelve frequencies on 31 August 2015 and 21 September 2015 in the top and bottom panels, respectively. The normalized intensity at each frequency and at each location is obtained by

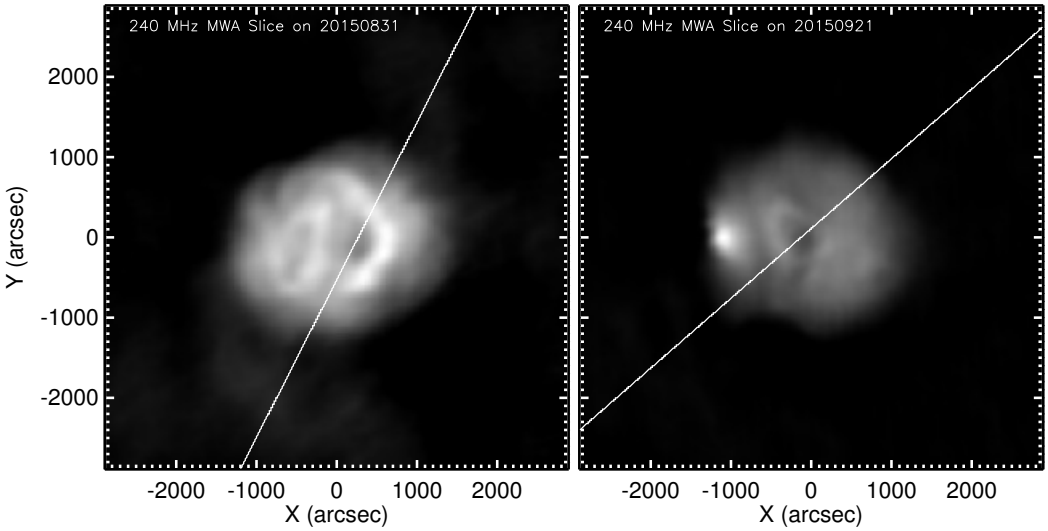

Figure 2.4: 240 MHz images obtained from MWA at 05:15 UT on 31 August 2015 and 05:13 UT on 21 September 2015, where the white lines correspond to the slices used for the normalized intensity plots shown in the top and bottom panels in Figure 2.5.

dividing the MWA data intensity by the median value of the pixels detected above 10σ, where σ stands for the signal-to-noise ratio. To calculate σ, we create a square box of 50×50 pixels at all four corners of the image and calculate the standard deviation of each box of pixels. We then average these standard deviations and multiply the averaged value by 10. The top panel in Figure 2.5 (31 August 2015) shows a clear transition from a profile with two peaks about a central minimum to a profile with one central maximum as the frequency decreases. The transition of the CH from being relatively dark to relatively bright takes place near 132 MHz, for which the intensity of the CH is roughly the same as the surrounding corona. The bottom panel in Figure 2.5 (21 September 2015) also shows an increase in intensity with decreasing frequency in similar fashion as the top panel. The transition for this CH similarly takes place around $\approx$ 132 MHz.

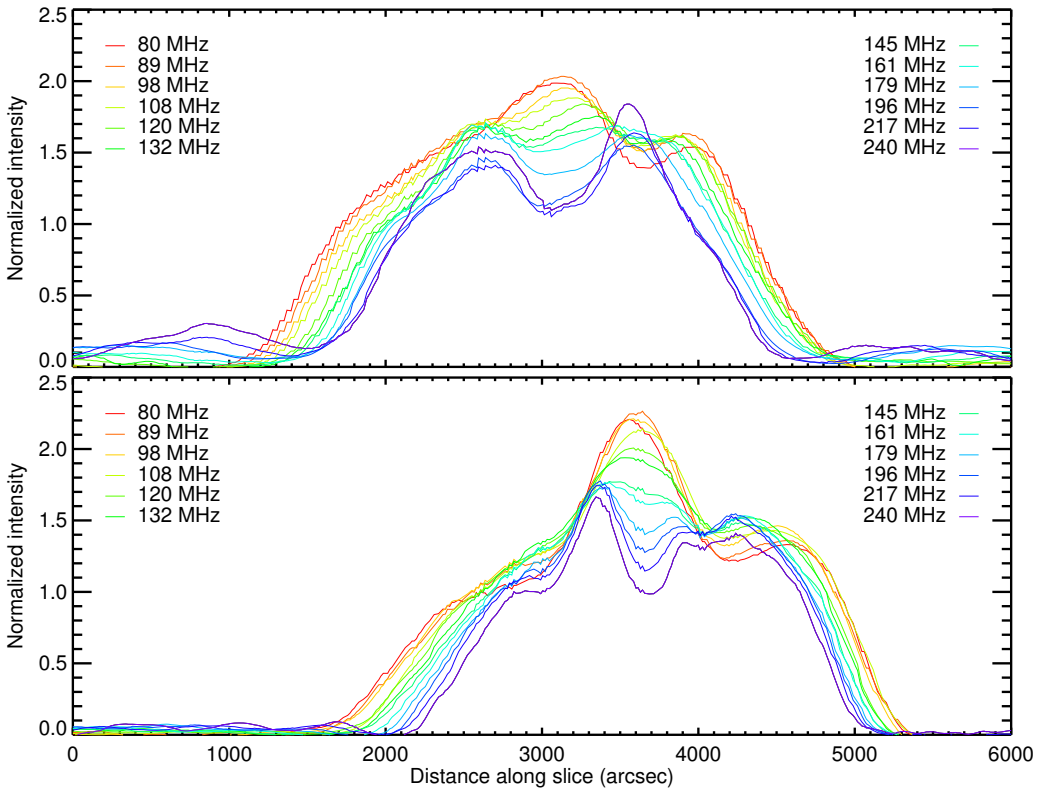

Figure 2.5: Variation in normalized intensity profiles with distance along the slice obtained from MWA data at 05:15 UT on 31 August 2015 (*top panel*) and 05:13 UT on 21 September 2015 (*bottom panel*).

2.2.3 Counterexample of Dark-to-bright Transition

Not all radio CHs show a dark-to-bright transition in the MWA frequency range. The CH at 03:43UT on 08 September 2015 shown in Figure 2.6 is a nice counterexample that has no dark-to-bright transition as the frequency decreases. Specifically, MWA observations reveal that the CH remains relatively darker at all frequencies. The CH location is still visible at 80 MHz, with a component that is slightly depressed relative to the surrounding corona and a component of comparable intensity. The contrast between different features on the Sun becomes smaller as frequency decreases in general. In this case, an active region (AR) is much more intense relative to the background at higher frequencies. Because our data are plotted with a linear scaling and the high end of the frequency range is enhanced by the AR, which makes the quiet Sun component look dimmer. The position of the CH also changes slightly as frequency decreases, shifting slightly towards the west from the solar disk center.

We also analyze the slice shown in the left panel of Figure 2.7, similar to Figures 2.4 and 2.5, to obtain the normalized intensity profile shown in the right panel of Figure 2.7. Clearly the relative brightness of the CH increases greatly compared with the side peaks in Figure 2.7 (right panel), but does not quite become bright compared to the side peaks. We next compare the normalized intensity profiles between the CHs shown in Figures 2.5 and 2.7. For CHs that show the dark-to-bright transition, the normalized intensity profile (Figure 2.5) has its highest intensity peak at lower frequencies, whereas this does not happen for the example of Figure 2.7. Even so, both Figures 2.5 and 2.7 show that the normalized CH intensity increases greatly with decreasing frequency for all three cases, showing that the same trend occurs for each example but to varying degrees. The difference is that in the counterexample, the CH increases

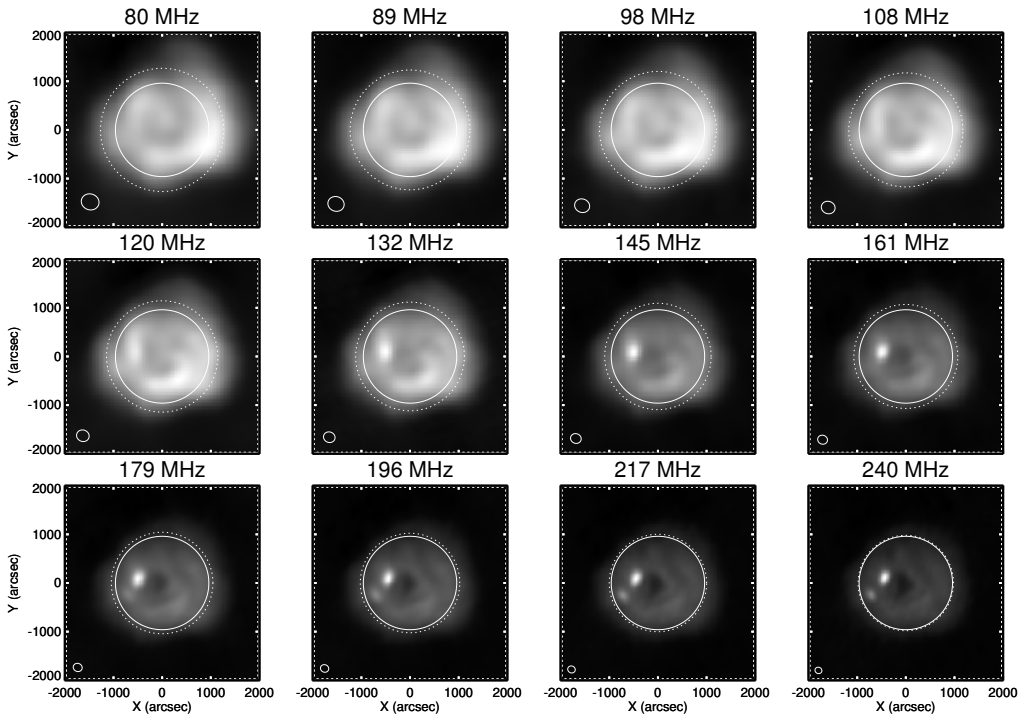

Figure 2.6: MWA observation of the CH structure at 03:43 UT on 08 September 2015 which has no dark-to-bright transition as frequency decreases in the MWA frequency range.

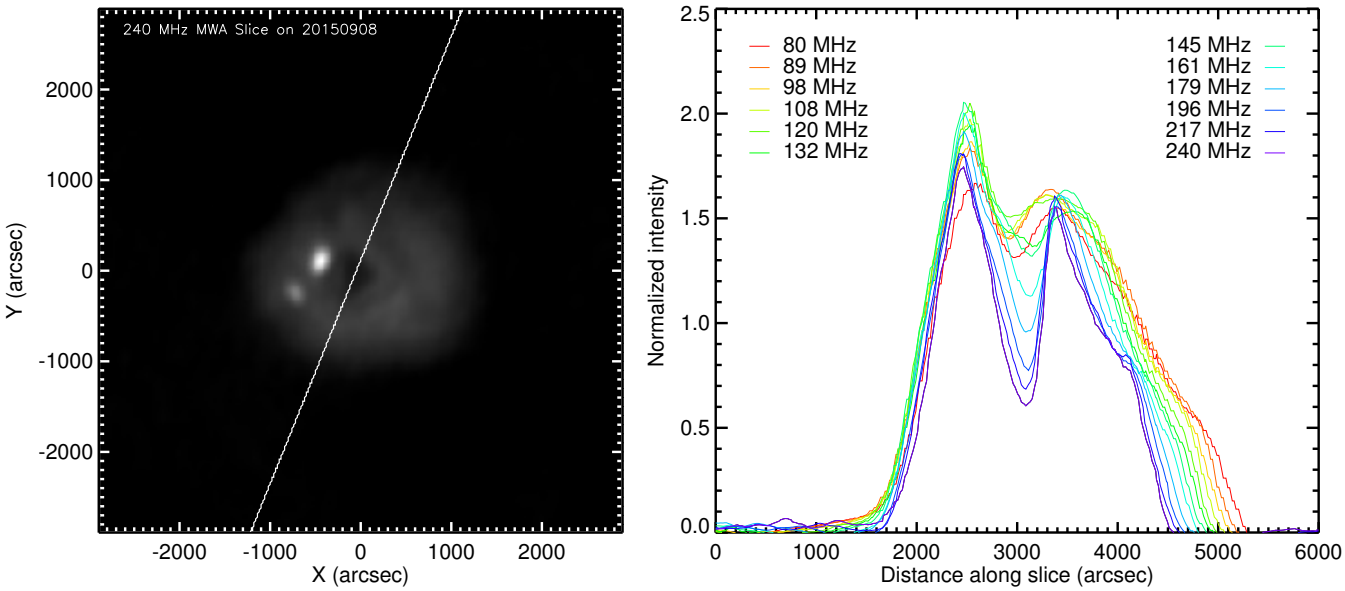

Figure 2.7: 240 MHz image obtained from MWA at 03:43 UT on 08 September 2015, where the white line corresponds to the slice (*left*) used for the normalized intensity plot (*right*).

in brightness with decreasing frequency but not to a level that exceeds the background intensity by 80 MHz. At 80 MHz, the dark-to-bright examples have around 60–70% greater intensities than that of the counterexample in the normalized units.

2.3 Modeled Coronal Hole Parameters

We extract density and temperature values from the MAS model using FORWARD at various radial heights to establish density and temperature profiles inside and outside the CH on 31 August 2015. Figure 2.8 shows the locations for which electron density and temperature profiles are extracted and shown in Figure 2.9. The "outside coronal hole" profile refers to an average of values along the white circle in Figure 2.8, and the shaded region denotes the standard deviation of values along the same circle for a given height.

The top panel in Figure 2.9 shows that inside the modeled CH the electron density decreases almost exponentially with radial distance. Moreover, below 1.4 $R_\odot$ the density inside the CH is less than the average density outside by a factor of four. This difference diminishes from 1.4 $R_\odot$ to 2.3 $R_\odot$, above which the density profile outside the CH is just 10−20% higher than inside with a very similar shape. Figure 2.9 demonstrates that the model successfully incorporates a low density region associated with the observed CH location.

The bottom panel in Figure 2.9 shows that the electron temperature inside the modeled CH increases steeply from 1.03 $R_\odot$ up to 1.4 $R_\odot$. Then it increases very slowly up to 3 $R_\odot$, being marginally hotter inside the CH than outside from ≈1.8−2.5 $R_\odot$. The CH is perhaps marginally cooler than the surrounding corona from 1.03 $R_\odot$ to 1.4 $R_\odot$. While the temperature increases monotonically inside the CH, the outside profiles peak near 1.1 $R_\odot$ and then decrease until 1.3 $R_\odot$ before increasing again. Above 1.4 $R_\odot$, the temperature profiles are very similar inside and outside the CH.

2.4 Propagation Effects and Refraction Idea

This section addresses the dark-to-bright transition of CHs by calculating the optical depth of radiation in the CH *versus* the background corona (Section 2.4.1) and then presenting a qualitative model involving propagation and refraction effects (Section 2.4.2).

2.4.1 Optical Depth Calculation

We now use the density and temperature profiles presented in Section 2.3 to calculate the optical depth τ inside and outside the CH. We assume that the side area $A_{CH}(\omega)$ of the CH is annular or ring-shaped and show that $A_{CH}(\omega)$ increases with decreasing radio frequency ω as required for the model in Section

2.4.2.

The amount of radio absorption is connected to the optical depth τ via a factor $e^{-\tau}$. We start from the equation for the absorption coefficient $\alpha(\omega)$ for free-free or bremsstrahlung radiation (Rybicki and Lightman, 1979),

$$\alpha(\omega) = \frac{1.8 \times 10^{-12} Z^2 n_e^2(r) g(\omega)}{\omega^2 T^{3/2}(r)}. \tag{2.1}$$

Here Z, n_e, and T are the atomic number, number density, and temperature of electrons, respectively, and g is the Gaunt factor, which is dependent on ω. Of course, n_e and T are dependent on the radial height r. The unit of $\alpha(\omega)$ is m^{-1}. Now τ is the integral of $\alpha(\omega)$ along the line of sight (Gelfreikh, 2004):

$$\tau = \int_{r_1}^{r_2} \alpha(\omega) dr. \tag{2.2}$$

We write $r_1 = 1\ R_\odot + h_{PL}(\omega)$ where h_{PL} is the height of the plasma layer where the angular electron plasma frequency $\omega_p(r) \propto n_e(r)^{1/2}$ first equals ω and the definition of r_1 corresponds to the radiation at ω only being generated above the associated plasma layer. We choose $r_2 = 3\ R_\odot$ since, as shown below, $\tau(\omega)$ reaches a constant ω dependent value below $r = r_2$ for the frequency range of interest here.

We cannot start the initial limit for integrations at the surface of the Sun because the MAS model does not include the photosphere. The actual height that we use for the integrations lies between 1.03 and 3 $R_\odot$.

The top panel in Figure 2.10 shows τ profiles inside the CH for twelve frequencies. The values of τ are calculated using Equation (2.2) and the density and temperature profiles obtained from the MAS model. For 80 MHz, τ starts rising from 1.07 $R_\odot$ and exceeds 0.5 at 1.2 $R_\odot$ inside the CH. Similarly for 145 MHz τ increases very steeply to more than unity at 1.15 $R_\odot$. These increases

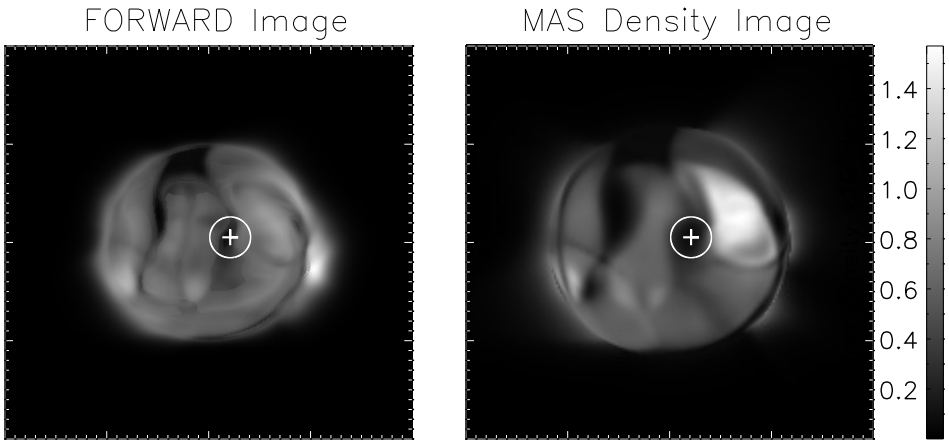

Figure 2.8: Positions inside (*plus sign*) and outside (*white circle*) the CH on 31 August 2015 at 05:15 UT in both FORWARD (*left*) synthetic and MAS density (*right*) images, respectively. The density image is obtained at 1.2 $R_\odot$. The color bar indicates density values in the order of 10^8 where the unit is cm^{-3}. These positions are used for the density and temperature profiles inside and outside the CH shown in Figure 2.9.

in τ take place very rapidly from 80 to 145 MHz below about 1.2 $R_\odot$. At lower frequencies, emissions accumulate a specified τ at larger heights. For each ω, τ asymptotes to a constant ω-dependent value below $r \simeq 1.2$ $R_\odot$. Moreover, the maximum value of τ occurs near 145 MHz and decreases towards both higher and lower frequencies in the range 80−240 MHz. Values of τ decrease above 145 MHz (up to 240 MHz). Thus from the top panel in Figure 2.10, we can say that as ω decreases radio emission starts at increasingly larger radial heights and has maximum τ near 145 MHz, with lower τ at lower ω.

The bottom panel in Figure 2.10 shows τ profiles outside the CH for twelve frequencies as a function of radial height using the average density and temperature profiles from Section 2.3. As expected, the resulting τ profiles are qualitatively very similar to those inside the CH. The plasma layers and $\tau = 0$ locations start at larger heights outside the CH as compared to τ profiles inside the CH for the same ω. For 80 MHz, we see that the τ profile starts from 1.17

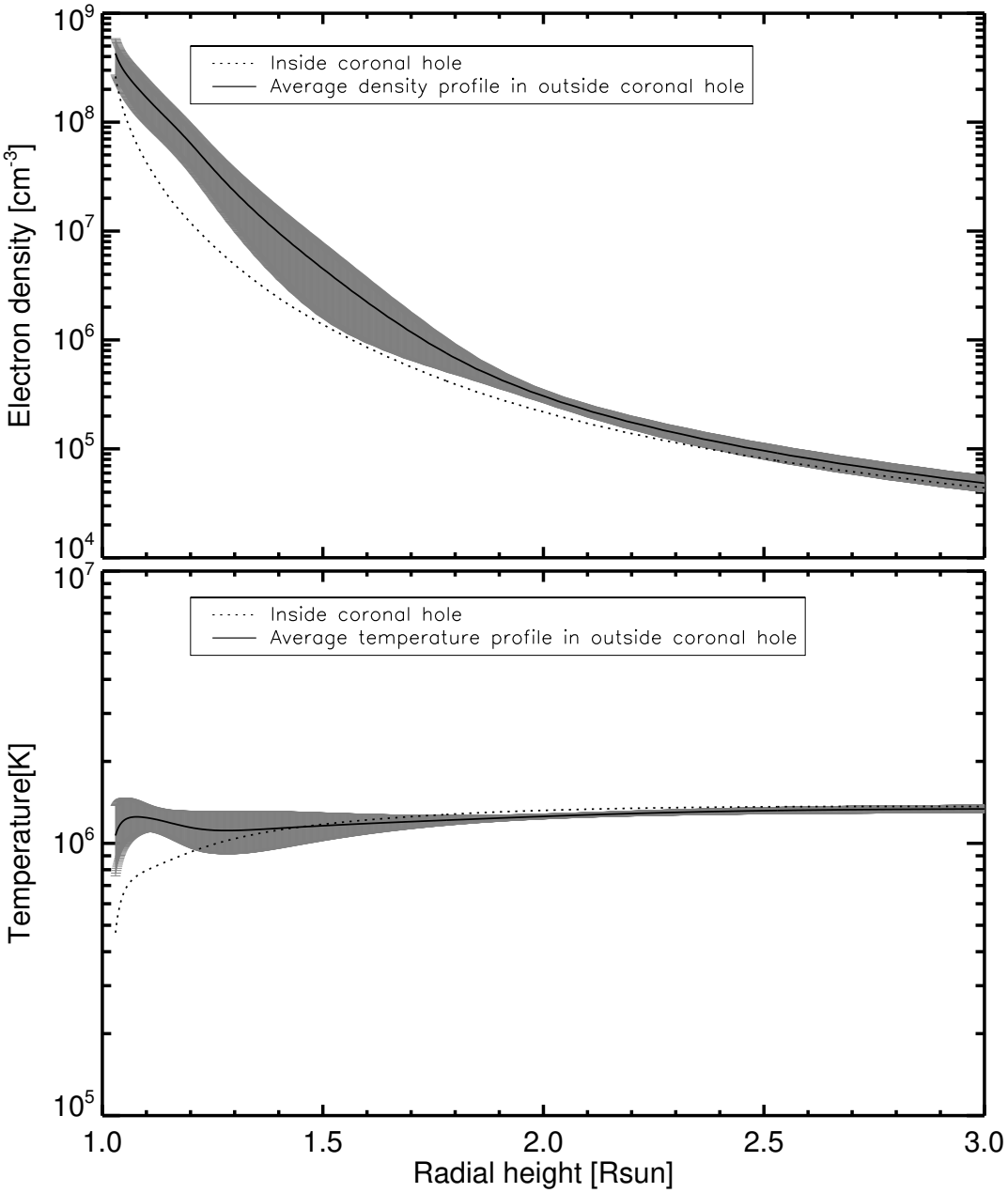

Figure 2.9: *Top panel*: Radial electron density profile inside the CH (dotted curve) and the averaged electron density profile outside the CH (solid curve). The thick gray colored shaded profile is for the standard deviation in the densities outside the CH (the white circle in Figure 2.8) plotted as error bars on top of the averaged electron density profile. *Bottom panel*: Radial temperature profile, in the same format as the top panel. The density and temperature values are from the MAS model at 05:15UT on 31 August 2015.

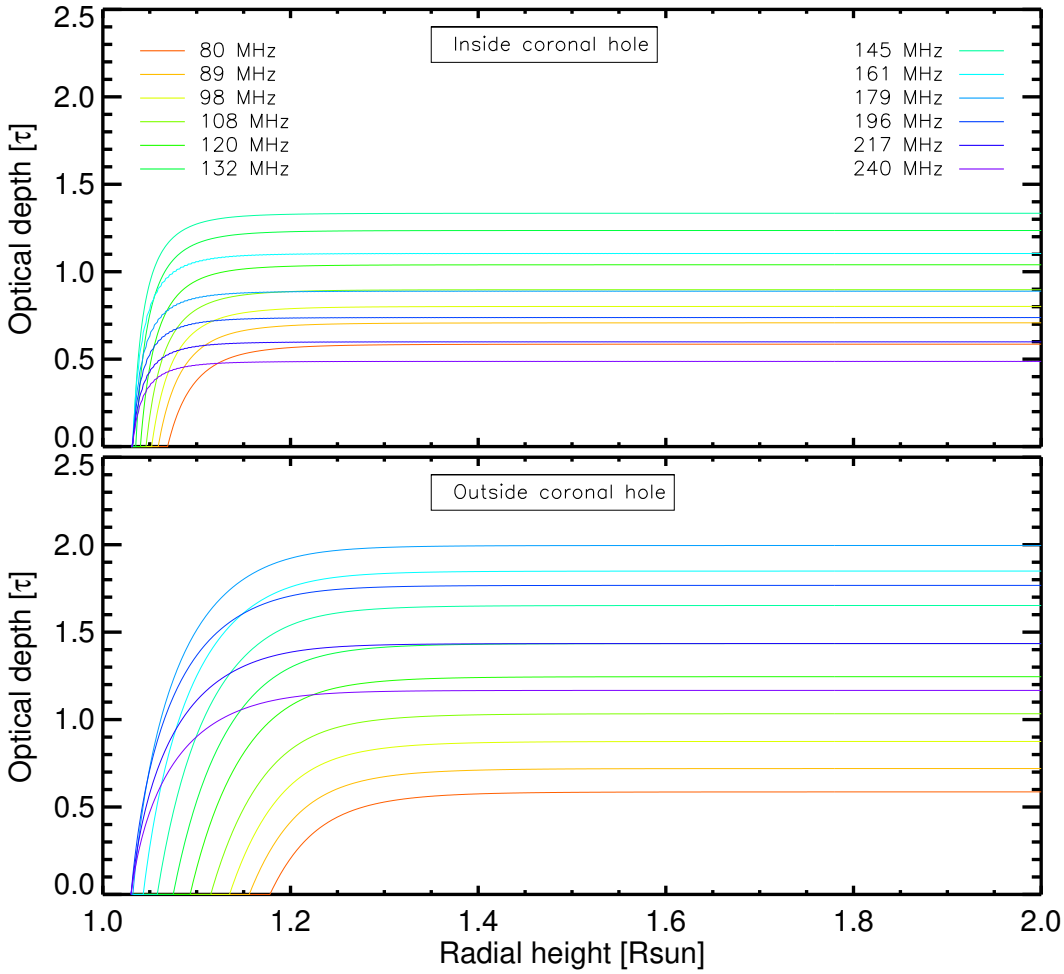

Figure 2.10: τ profiles inside and outside the CH in the *top* and *bottom* panels, respectively. These τ profiles are estimated by Equation (2.2) using densities and temperatures from the MAS model.

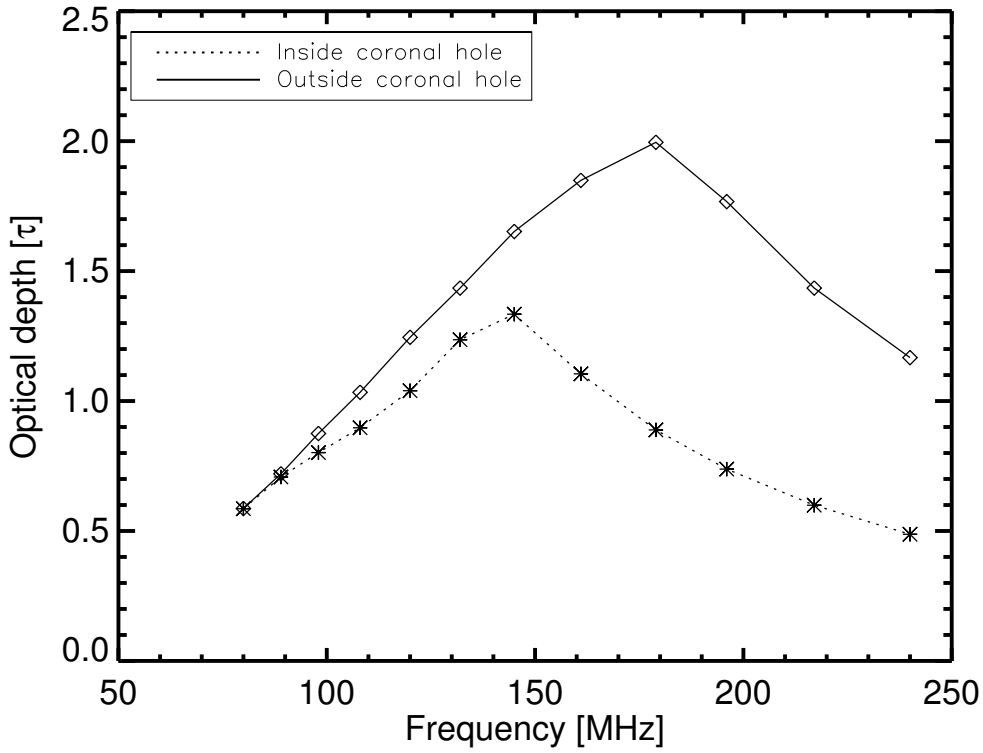

Figure 2.11: Variations in τ with frequency inside and outside the CH.

$R_\odot$ and goes to 0.5 at 1.3 $R_\odot$. As expected, the τ profiles start at lower heights for higher frequencies compared to the τ profile for 80 MHz. Note that the final values of τ reached above 1.2 $R_\odot$ are larger outside the CH than inside, except for frequencies below about 89 MHz.

Figure 2.11 shows how the final τ value changes with ω. τ increases almost linearly as ω increases up to 145 MHz inside and 179 MHz outside the CH, respectively. Then τ decreases almost linearly with increasing ω inside the CH from 145 MHz to 240 MHz, with a similar behavior from 179 MHz to 240 MHz outside the CH. Note that τ is larger outside the CH by a factor of two than inside the CH between 161 and 240 MHz. We also note that $\tau(\omega)$ is very similar in magnitude inside and outside the CH from 80 to 145 MHz, which means that those features should have similar intensities in absence of any additional

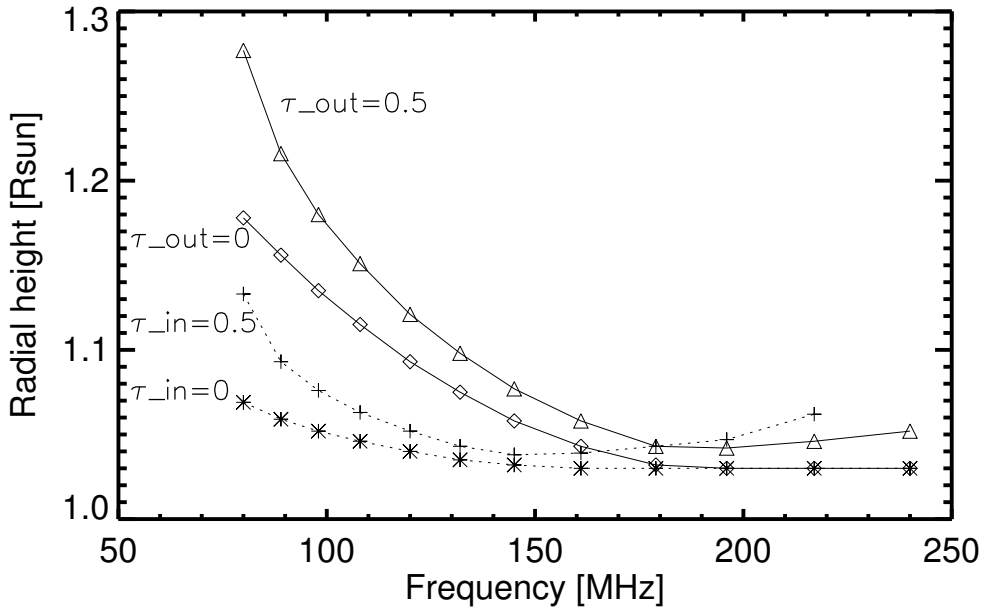

Figure 2.12: Variations in heights as a function of frequency. $\tau_{\rm in}$ and $\tau_{\rm out}$ are for τ = 0 and τ = 0.5 inside and outside the CH, respectively.

effects.

Figure 2.12 shows the variations in height with increasing frequency for different values of τ inside and outside the CH. The heights of the plasma layers (τ = 0) decrease with increasing ω inside and outside the CH. The heights where τ = 0.5 also decrease with increasing ω up to 145 and 179 MHz inside and outside the CH, respectively, before increasing slightly with ω. It is noted here a value of τ = 0.5 is somehow considered to be reached at 240 MHz inside the CH. These values of τ may be somewhat underestimated as the modeled densities do not reach those corresponding to the plasma frequency, and the chromosphere is not included in the MAS model. Note that the heights outside the CH are larger than inside the CH by a factor of two below 145 MHz for both τ = 0 and τ = 0.5.

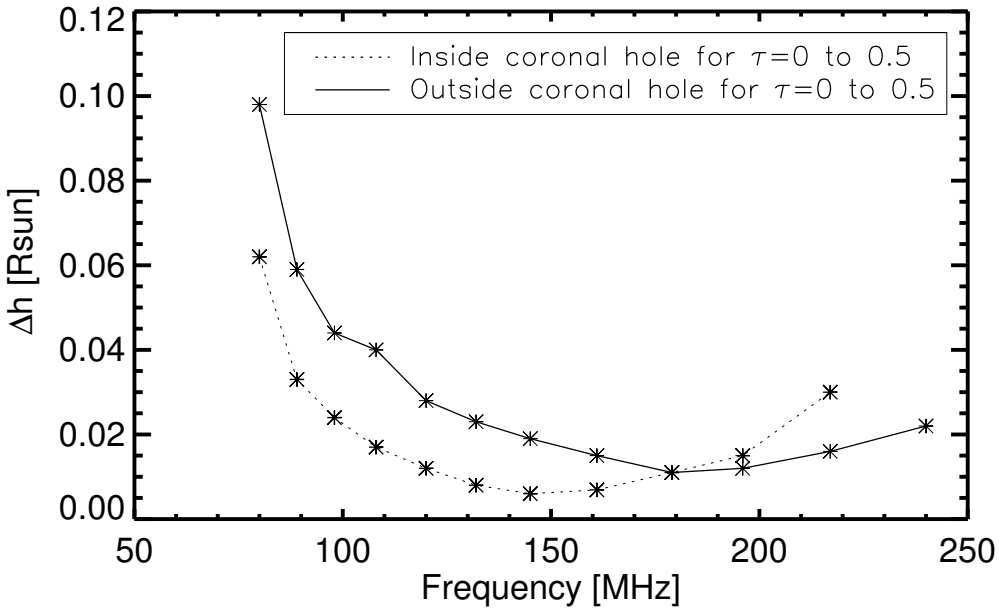

Figure 2.13: Difference in heights as a function of frequency inside and outside the CH.

We now consider the difference in height Δh between the $\tau = 0$ and 0.5 levels (*i.e.* $h_{\tau=0.5} - h_{\tau=0}$). Figure 2.13 presents Δh profiles inside and outside the CH. Δh decreases with increasing frequency ω up to 145 MHz inside and 179 MHz outside the CH, respectively, and then increases slowly with increasing ω. Figure 2.13 shows that below 161 MHz, Δh inside the CH is less than outside the CH by approximately a factor of 1.5.

2.4.2 Qualitative Model

A brief summary of the qualitative model for the dark-to-bright transition of CHs as the radio frequency decreases is as follows. First, the optical depth inside the CH is significantly lower than outside at higher frequencies, whereas there is only a slight difference in optical depth at lower frequencies, meaning

that the CH should be of comparable brightness to the surrounding corona absent of any other effects. Second, radiation generated in the surrounding corona that propagates toward the CH will be refracted at the CH boundary toward the radial direction, which happens to a greater extent with decreasing frequency. This insight provides a framework by which to constrain the possible underlying physical mechanisms, of which we speculate refraction at the CH boundary is most likely. Third, the combination of these two effects leads to the observed dark-to-bright (relative to the surrounding corona) transition as frequency decreases. We now consider the elements of this model in more detail.

Ray paths can be dramatically altered by refraction as radio waves propagate through the corona (Robinson, 1983). Refraction can happen due to small-scale or large-scale changes in density. Radio emission is refracted toward regions of higher refractive index, corresponding to moving from high to low density regions and so from elsewhere in the corona into a CH, as shown next. The refractive index n can be written in terms of wave number k, speed of light c, and wave frequency ω as

$$n = kc/\omega. \tag{2.3}$$

For radio waves in an unmagnetized plasma, the plasma frequency ω_p and ω are related by the dispersion relation

$$\omega^2 = \omega_p^2 + k^2 c^2,$$

whence

$$kc = \sqrt{\omega^2 - \omega_p^2}. \tag{2.4}$$

From Equations (2.3) and (2.4) we obtain

$$n = \sqrt{1 - \omega_p^2/\omega^2}. \tag{2.5}$$

Hence, $n = 0$ for $\omega = \omega_p$ and $n \cong 1$ for $\omega^2 \gg \omega_p^2$. Refraction happens from high ω_p to small ω_p from $n \simeq 0$ to $n \approx 1$. From Equation (2.5), it is clear that the refractive index increases as ω decreases for constant k.

We are interested in propagation effects due to refraction around a CH. Let us consider a CH as a low density funnel, as shown in Figure 2.14, into which radio waves can enter from adjacent source regions. $A_{CH}(\omega)$ indicates the side area of the CH, which is ω dependent. We consider the height $h_{\tau=0.5}$ where $\tau = 0.5$ and the height h_{PL} of the plasma layer where $\tau = 0$. The heights h_{PL} and $h_{\tau=0.5}$ vary with ω.

From Figure 2.11 we note that τ is not significantly different inside and outside the CH at low frequencies below 145 MHz but τ is smaller inside the CH by a factor of two from 161 MHz to 240 MHz. Thus, the brightness of a CH will approach that of the background with decreasing frequency as the difference in optical depths between different regions becomes smaller. Our optical depth estimates suggest that, absent of any other effects, a CH should have roughly the same intensity as a quiet-Sun region at 80 MHz. The dark-to-bright transition is therefore partly due to the difference in optical depths becoming smaller but mostly because additional physics is required to produce the large enhancements over the background level seen in our low-frequency data.

We now consider the propagation effect associated with refraction in which radio emission generated sufficiently close to a CH boundary will propagate toward the CH and be refracted radially into the CH, as considered in some detail below.

Radiation starts being emitted where $\tau = 0$ and continues to be emitted at larger heights but is also increasingly absorbed as τ accumulates with height, with power $P(\tau) = e^{-\tau P(0)}$ for radiation emitted only at $\tau = 0$. There are three cases considered here and in Figure 2.14. In case 1, radio emission is generated in a CH and stays there, in case 2, emission is generated in the surrounding

corona and propagates into a CH, and in case 3, emission is generated in the corona and stays there. Radiation propagating inside a CH is much less likely to be absorbed because of the lower opacities in case 1. For case 2, the radiation generated above the $\tau = 0$ layer is not absorbed, but instead is refracted into the low density CH from the adjacent higher-density corona. This results in additional flux appearing to come from the CH while having been generated elsewhere. For case 3, the radiation generated in the surrounding corona is absorbed at somewhat larger rate than inside the CH.

We propose that Δh increases as ω decreases outside the CH, as shown in Figures 2.13 and 2.14, and that this increases the side area $A_{CH}(\omega)$ of the CH through which radiation can enter the CH from the corona. We can write $A_{CH}(\omega) = 2\pi r_{CH}(\omega)\Delta h(\omega)$ for a cylindrical CH, where $r_{CH}(\omega)$ is the radius of the CH, and propose that $A_{CH}(\omega)$ increases as ω decreases since Δh (*i.e.* $h_{\tau=0.5}(\omega) - h_{PL}(\omega)$) increases as ω decreases. That is, at lower frequencies (*e.g.* 80 MHz), the side area of the CH goes up and more radiation propagates into the CH from the corona (*e.g.* due to refraction caused by the decrease in n), before eventually propagating upwards and out of the CH to the observer.

Figure 2.13 provides evidence that $\Delta h(\omega)$ and so $A_{CH}(\omega)$ indeed increase as ω decreases, as proposed. The radiation power P_{CH} entering into the CH can be written as

$$P_{CH} = \varepsilon(\omega) A_{CH}(\omega), \tag{2.6}$$

where $\varepsilon(\omega)$ is the energy density *per* unit volume. If $\varepsilon(\omega)$ is independent of ω, then an ω dependence for $A_{CH}(\omega)$ can drive changes in brightness of the CH as a function of ω.

Our idea suggests that the power of radio emission from the CH at high frequencies and from the corona at all frequencies is "thermal", with

$$P_{CH}(high\ \omega) = P_{CH\ Th}(high\ \omega) \tag{2.7}$$

and

$$P_C(\omega) = P_{C\ Th}(\omega), \tag{2.8}$$

for the CH and corona (C), respectively. We assume that

$$P_{CH}(low\ \omega) = P_{CH\ Th}(\omega) + P_{Prop\ CH}(\omega),$$

where using Equation (2.6),

$$P_{CH}(low\ \omega) = P_{CH\ Th}(\omega) + \varepsilon(\omega)2\pi r_{CH}(\omega)\Delta h(\omega). \tag{2.9}$$

Here P_{Th} is the power due to thermal emission, $P_{Prop\ CH}$ is the power of radio waves propagating from the corona into the CH, P_C is the power in the corona. Now the idea is that $P_{C\ Th}(\omega)$ and $P_{CH\ Th}(\omega)$ vary with ω in the same way as each other but that $P_{Prop\ CH}(\omega)$ increases as ω decreases. Thus to match the dark-to-bright phenomenon, it is necessary that $P_{Prop\ CH}(\omega)$ increases sufficiently more rapidly at low ω than $P_{C\ Th}(\omega)$ and $P_{CH\ Th}(\omega)$, so that the sum of power of radio waves entering into the CH is higher at low ω and lower at high ω. We can write these constraints at low ω as

$$P_{CH}(low\ \omega) = P_{CH\ Th}(\omega) + P_{Prop\ CH}(\omega) > P_{C\ Th}(\omega), \tag{2.10}$$

and

$$P_{CH}(high\ \omega) = P_{CH\ Th}(\omega) + P_{Prop\ CH}(\omega) < P_{C\ Th}(\omega), \tag{2.11}$$

whence

$$\frac{d}{d\omega}P_{CH}(\omega) < \frac{d}{d\omega}P_C(\omega) \tag{2.12}$$

and

$$\frac{d}{d\omega}P_{Prop\ CH}(\omega) < \frac{d}{d\omega}[P_{C\ Th}(\omega) - P_{CH\ Th}(\omega)]. \tag{2.13}$$

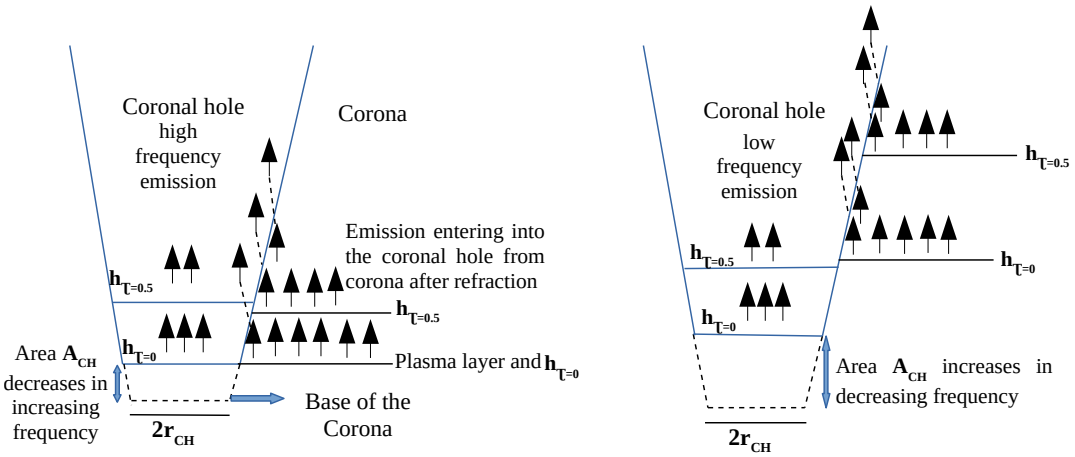

Figure 2.14: Cartoon representation of the dark-to-bright transition of radio CH at low frequencies. Filled arrows with straight lines indicate radio photons propagating straight to the observer in the CH or exterior corona. Arrows with dotted lines show more photons refracting into the CH from the corona as the frequency decreases through the increased side areas of the CH. Blue and black colored horizontal solid lines indicate different optical layers inside and outside the CH, respectively.

Equation (2.10) assumes that $P_{CH}(\omega)$ increases as ω decreases and that the $P_{Prop\ CH}(\omega)$ term arises at low ω due to higher power radio waves entering the CH from the corona at low ω. Thus we observe a radio-bright structure of the CH at low ω due to the term $P_{Prop\ CH}(\omega)$. But at high ω, we propose that the term $P_{Prop\ CH}(\omega)$ is small. As a consequence, we observe a radio-dark structure for the CH at high ω that is radio-bright at small ω. Thus following the suggestion of Alissandrakis (1994) that refraction effects can significantly change the radio map of the corona, we conclude that the radio-dark structure of a CH changes into a radio-bright structure with decreasing frequency is due to propagation and refraction.

2.5 Discussion and Conclusions

We have demonstrated observationally the dark-to-bright transition of CHs from high to low radio frequencies in MWA data in Figure 2.1. This dark-to-bright transition is not predicted by existing theory. The MAS-FORWARD model does not show the dark-to-bright transition that we observe. We argue that CHs observed in MWA radio data can be radio-dark at high frequencies but radio-bright at low frequencies due to propagation and refraction effects. It is well known that propagation effects due to refraction can change the spatial extent of a source and decrease its brightness (Thejappa and MacDowall, 2008; Ingale et al., 2015).

Possible explanations include refraction of radio waves due to density inhomogeneities (Alissandrakis, 1994; Shibasaki et al., 2011). Alissandrakis (1994) suggested that refractive effects could cause a low-frequency enhancement of CHs on the solar limb, whereas we develop our interpretation based on similar ideas but for CHs near disk center, where the low-frequency enhancements have been observed. Other proposed explanations exist for the dark-to-bright transition of CHs. Golap and Sastry (1994) proposed that the brightness of a CH near disk center depends on magnetic field but that a CH is always dark at the limb whatever the magnetic field strength is. An alternative suggestion given by Sheridan and Dulk (1980) is that the electron temperature is relatively higher in a CH than the surrounding regions, making the CH brighter at the disk center. This suggestion is inconsistent with the MAS simulation data of Figure 2.9.

At higher frequencies, the MWA data show that the radio CHs have sharp boundaries (*e.g.* Figures 2.1 and 2.6), while in the middle of our frequency range (as shown in Figure 2.6) CHs are indiscernible regions in the solar corona. The same phenomenon for CHs is described by Mercier and Chambe (2012)

at the bottom of their frequency range. At our lowest frequencies, CHs are often (but not always) distinguishable as intensity enhancements when observed near disk center. We note that the frequency at which dark-to-bright transition occurs (*i.e.* the frequency for which the CH intensity is closest to that of the surrounding corona) is not the same for all four CHs presented in Section 2.2. The dark-to-bright CH transition happens near 145 MHz (Figure 2.1) for the 28 August 2014 event, whereas the other CHs show transitions near 130 MHz for the 31 August 2015, 135 MHz for the 21 September 2015, and 145 MHz for the 11 November 2015 events, respectively. The reason for this variance is an interesting topic for further research.

If emission generated outside of a CH is systematically redirected into it, then a corollary of this effect should be diminished intensity in the region surrounding the CH. If the structure of the CH is such that this occurs uniformly around the exterior, then we would expect to see a dark ring around the CH. This feature is clearly apparent in at least two of our observations, on 28 August 2014 and 21 September 2015 (Figure 2.1), particularly at the lowest frequencies. Note that we would expect this only in the optically thin regime for which a photon that is redirected into the CH would still have been likely to escape outside of the CH. As τ increases above unity with increasing frequency outside the CH, a certain amount of emission can be refracted into the CH without significantly diminishing the apparent intensity outside. The magnitude of the intensity depression surrounding the CH should therefore be smaller at higher frequencies, which is also what we observe.

Some CHs are also found to change their positions as a function of frequency (Figures 2.1, 2.5, and 2.6). For instance the CH on 28 August 2014 is seen to change its position slightly to the north from the disk center as frequency decreases. This could be due to the shape of the CH as it expands with height, as dictated by its magnetic field configuration. But it could also be that ionospheric

refraction, which is stronger at lower frequencies, has shifted the position of the entire Sun to some extent due to changes in the ionosphere between the calibration and solar observations. Moreover, a sharp ring is observed around the boundary of the CH at 240 MHz which is not clearly observed at 80 MHz. We propose that the larger refractive effect at low frequencies, which helps more photons to propagate into the CH boundary from the outside corona, also causes the ring feature of the CH to vanish at low frequencies.

All disk-center CHs do not necessarily exhibit a strong low-frequency enhancement, as shown in Figure 2.6. CHs are typically thought of as expanding funnels, and we speculate that how fast a CH expands as a function of r may determine whether a CH is radio-bright at a particular frequency. Some CHs open fast, with larger opening angles and areas as a function of r, while other CHs open more slowly with smaller areas as a function of r. Accordingly, the faster the CH opens, the more radiation will enter into the CH via its larger side areas $A_{CH}(\omega)$, leading more easily to a larger intensity at a given frequency. If so, then the CHs in Figure 2.1 should open faster than the CH in Figure 2.6. Figure 2.13 provides evidence that $\Delta h(\omega)$ increases as ω decreases. Accordingly, $A_{CH}(\omega) = 2\pi r_{CH}(\omega)\Delta h(\omega)$ should increase as ω decreases and r increases provided that the dependences of r_{CH} on ω and r do not counteract those of $\Delta h(\omega)$. If a CH expands super-radially then $r_{CH}(\omega)$ increases faster than r. Some studies of CH morphology find boundary expansions that are radial (Woo and Habbal, 1999; Woo et al., 1999) and others super-radial (DeForest et al., 2001). The data in Figures 2.1 and 2.4 suggest that r_{CH} increases as ω decreases and r increases, as do the cartoons in Figure 2.14. Thus the available data and our theoretical calculations suggest that $A_{CH}(\omega)$ indeed increases as ω decreases and r increases, as proposed.

The cartoon representation (Figure 2.14) suggests that the brightness should be primarily enhanced at the CH boundary, which would lead to a bright ring

of emission around the edge. This is exactly what we see at higher frequencies, particularly in the 28 August 2014 observation. The bright ring gradually disappears with decreasing frequency until the CH becomes a uniformly bright feature at our lowest frequencies, which is likely due in part to the diminished spatial resolution at lower frequencies. Very large CHs should therefore exhibit this ring feature down to lower frequencies, but disk-center CHs do not often get much larger than our 80 MHz beam size. The higher spatial resolutions provided by the expanded Phase II MWA (Li et al., 2018) may thus be used to test this hypothesis in future work. However, we note that if scattering is sufficiently enhanced in some CHs over the background corona then the ring feature may become unobservable due to diffusive effects of scattering.

In Figures 2.5 and 2.7 we studied the intensity of CHs normalized by the median value of the quiescent Sun intensity for our twelve frequencies. We do this normalization so as to calculate a reasonable quiet-Sun background to which the CH intensity can be compared. It is noted that the position of the Sun seems to shift systematically to the right with decreasing frequency (right panel in Figure 2.7). The reason for this shift may be ionospheric refraction, which is stronger at lower frequencies and will noticeably impact our data if ionospheric conditions changed significantly over the ≈2 hours between the time of the solar observation and the calibration observation used to set the antenna phases. A flux-calibrated spectrum would aid in discriminating between different emission mechanisms. Future work may incorporate the flux calibration methods described by Oberoi et al. (2017) and Mohan and Oberoi (2017) for this purpose, but that is beyond the scope of this work.

Refraction effects and relative optical depths are important in our model for the CH dark-to-bright transition at low frequencies. A future quantitative calculation of ray tracing in suitable plasma structures, such as those provided by MAS, would allow a direct calculation of our model for the dark-to-bright

transition of many CHs.

The MWA data that we used for our analysis are for CHs near disk center but not near the solar limb. Our model would expect CHs to diminish in brightness with proximity to the limb, since the radiation is refracted radially on average and so not towards Earth, and future work could investigate this potential viewing angle effect by examining CHs continuously as they transit the Sun from limb to limb.

In summary, we presented, analyzed, and interpreted MWA observations of CHs in the frequency range 80−240 MHz. Since CHs are low-density regions relative to the corona, CHs are expected to be observed as dark structures across the bandwidth of MWA. However, we observed four CHs near disk center that transition from being relatively dark structures at higher frequencies ($\gtrsim$ 145 MHz) to relatively bright structures at lower frequencies ($\lesssim$ 145 MHz). We showed that some CHs have a transition frequency near 145 MHz and some other CHs have that transition frequency near 130 MHz or 135 MHz. We compared MWA observations to FORWARD synthetic images based on the MAS model. The synthetic images obtained from model data did not exhibit the dark-to-bright transition, so that this model is not consistent with our observations at lower frequencies. We proposed that the dark-to-bright transition results from refraction of radio waves from the surrounding corona into the low density CH regions, and we developed a qualitative model based on refraction and the relative optical depths inside and outside a CH as a function of frequency. The optical depths calculated based on the MAS model are qualitatively consistent with our interpretation. We have therefore shown that propagation and relative absorption effects are a feasible explanation for the dark-to-bright transition exhibited by these CHs from high to low frequencies.

Chapter 3

Spectropolarimetric Imaging of Metric Type III Solar Radio Bursts

Abstract

We present low-frequency (80−240 MHz) radio observations of circular polarization in sixteen isolated type III solar radio bursts using the *Murchison Widefield Array* (MWA) between August 2014 and November 2015. On average for most of the bursts, near burst onset, we find degrees of circular polarization 5−30% at 80 MHz and 15−40% at 240 MHz and these percentages are 3−15% and 5−25% near burst maximum. We measure polarization fractions as a function of burst source's positions. On average, near both burst onset and maximum, we find higher polarization near the disk center and lower polarization when the burst source is near the limb. We study total intensity (Stokes I), circularly polarized intensity (Stokes V), and polarization fraction ($\mid V \mid/I$) profiles for type III bursts with and without source motion as a function of position at times when the intensity of bursts is maximum. The burst event with no source motion, we find symmetric profiles for Stokes I, V, and $\mid V \mid/I$, we also find symmetric I, V, but asymmetric $\mid V \mid/I$ profiles for those burst events which have source motion. We argue that this asymmetric $\mid V \mid/I$ profile is due to the fundamental emission at the front of a type III electron beam and motion of the burst source. We then analyze the relative burst source motion and polarization fraction. At burst onset, we obtain relatively higher polarization fractions, which is considered to be due to a large contribution from fundamental plasma emission. At burst maximum, the polarization fraction is lower due to the combination of fundamental and harmonic components. After at peak intensity, the emission is dominated again by the fundamental component that decays until the end of a burst with lesser polarization fraction than earlier. We argue that the fundamental radiation that decays over time after peak burst intensity is strongly scattered. This pattern of fundamental, fundamental and harmonic, and then fundamental emission with time is consistent with the interpretations

of Dulk et al. (1984), Robinson et al. (1994), and Robinson and Cairns (1998). We propose that the scattering effect can be a viable reason for low polarization fractions for type III events. Finally, we investigate the variations of decay time (t_d) for three events with frequency (f) where $t_d \propto f^{-2.0\pm0.1}$ decreases more rapidly with increasing f compared with lower-frequency observations ($t_d \propto f^{-1.1\pm0.1}$).

3.1 Introduction

Solar radio bursts are classified based on their frequency drift rate (Wild and McCready, 1950), with type III bursts drifting faster than type II and I bursts. The frequencies of type III bursts have been observed as high as 10 GHz at the bottom of the corona down to 30 kHz at 1 AU. *Coronal* type III bursts have frequencies above about 10 MHz, whereas *interplanetary* type III bursts have frequencies from about 10 MHz to 20 kHz or below around 1 AU (Leblanc et al., 1998; Lin et al., 1973). Type III solar radio bursts are a crucial diagnostic tool for understanding the acceleration of solar electron beams (Goldman, 1984; Robinson and Cairns, 2000; Reid and Ratcliffe, 2014; Reid and Kontar, 2018), and they are one of the most familiar signatures of the magnetic reconnection process thought to drive solar flares (Cairns et al., 2018). They usually have high brightness temperatures that imply non-thermal emission from semi-relativistic electrons. The basic theory is that electron beams generate Langmuir waves by the bump-on-tail instability that then couple nonlinearly to produce radiation at the plasma frequency (f_p) and its second harmonic ($2f_p$). The theory of type III radio bursts has been developed by many authors (Ginzburg and Zhelezniakov, 1958; Goldman, 1983; Dulk, 1985; Cairns, 1987b, 1988; Robinson and Cairns, 2000; Melrose, 2009; Li et al., 2010; Kontar et al., 2017).

Type III solar radio bursts can be classified according to their frequency-

time structures in any of the sub-classes named as structureless (Mercier, 1990), fundamental (F), harmonic (H) (Suzuki and Dulk, 1985), and fundamental-harmonic (F-H) pairs based on their appearance in dynamic spectrum, range of frequencies they originate, F-H ratio, and polarization measurement, etc. Usually, type III bursts do not exhibit F-H structure at frequencies below ≈ 100 MHz (Dulk et al., 1984). There is still doubt as to whether both F and H components are present in type III bursts below that frequency. It is widely argued that above 100 MHz, type III bursts are predominantly H emission due to their generally low polarizations and lack of F-H structure (Suzuki and Dulk, 1985) although Li et al. (2016) provide arguments against this. At higher frequencies, from ≥ 100 MHz to a few hundred MHz, there is a significant percentage of F-H components in bursts where the F component starts from 60 MHz and H component starts at ≈ 200 MHz (Dulk and Suzuki, 1980). It is noted that for many (not all) *interplanetary* type IIIs, the radio emission is dominated by the F component at the burst onset, which would exhibit higher polarization fractions, than near the burst peak when the emission is a mixture of F and H emission (Dulk et al., 1984). In the decay phase, the F component dominates again and becomes weaker in polarization due to the scattering effect (Robinson, 1983; Robinson and Cairns, 1998). The precise theoretical idea about the dominance of F radiation at the burst onset and during the decay phase is given by Robinson et al. (1994) and Robinson and Cairns (1998). We will consider this idea of F emission at the burst onset, both F and H emission near the peak burst intensity, and F emission during the decay phase for our type III burst events using the *Murchison Widefield Array* (MWA) at frequencies from 80 to 240 MHz. The MWA is a low-frequency radio telescope capable of imaging the solar corona across frequencies from 80 to 300 MHz (Tingay et al., 2013a,b).

A significant amount of research on type III bursts has appeared in the

literature during the past few decades (McLean, 1971; Dulk and Suzuki, 1980; Suzuki and Dulk, 1985; Robinson and Cairns, 1998; Reid and Ratcliffe, 2014; McCauley et al., 2017, 2018; Cairns et al., 2018; Mohan et al., 2019). Type IIIs show fascinating properties in their drift rate, brightness, motion, F and H structures, circular polarization, etc. The circular polarization measurements of type III bursts can provide information regarding the structure of the magnetic field and its strength above active regions (Mercier, 1990). Theory predicts 100% circular polarization for F emission in type III bursts, but it is less than that observationally. For instance, Dulk and Suzuki (1980) analyzed the polarization characteristics of 997 type III bursts and found the average degree of circular polarization of F and H emission in F-H pairs was 35% and 11%, respectively, whereas structureless bursts had 6% circular polarization on average.

Some radio observations reveal that the degree of circular polarization can reach its maximum before the maximum of the total intensity of type IIIs (Benz et al., 1982; Mercier, 1990). Benz and Zlobec (1978) investigated the circular polarization and frequency drift rate of type III bursts at 237 MHz using the *Trieste Polarimeter*. They found an approximately maximum 60% degree of circular polarization and also established a correlation between frequency drift rate and circular polarization. Using the *Culgoora Radioheliograph*, the degree of polarization of 997 type III bursts was studied by Suzuki et al. (1980) from 24 to 220 MHz. They found a maximum 60% degree of polarization for the F components ($\leq$100 MHz). Mercier (1990) studied the degree of circular polarization of sixteen well-isolated type III solar radio bursts in the frequency ranges from 164 to 435 MHz using the *Nançay Radioheliograph* and found that the circular polarization increased as a function of increasing frequency on average. The maximum degrees of circular polarization was approximately 23% at 435 MHz and 5% at 164 MHz. Observationally, type III bursts with nearly 100% circular polarization at microwave frequencies are reported in the

literature (Wang et al., 2003).

Time-varying circularly-polarized emission during a burst permits us to know about the magnetic field polarity of that burst, whether it is unipolar or bipolar relative to the sense of polarization (Mercier, 1990), or about changes in the emission mechanism (e.g. from F to H or vice versa). Motivated by the previous work on polarization measurements referenced above, we study the circular polarization characteristics of type IIIs observed by the MWA. This instrument has a polarimetric capability to image the Sun with good frequency resolution from 80 to 240 MHz (McCauley et al., 2019). Such low-frequency polarimetry of type III bursts is convenient to perform due to their high intensities and large polarization fractions that are easier to detect with the MWA. Besides this, the Stokes I (total intensity) and V (circular polarization) imaging observations of MWA provide information on total and circularly polarized emissions of solar type III bursts (McCauley et al., 2018) and weak polarization signatures associated with thermal bremsstrahlung emission of the solar quiescent corona (McCauley et al., 2019) as functions of frequency, time, and position. The emission coming from the solar quiescent corona will not be described in this Chapter. Thus, we present unique low-frequency imaging and circular polarization MWA observations of sixteen isolated type III bursts from 80 to 240 MHz. Investigations on both the degree of circular polarization and polarimetric imaging have not been reported in the literature in this frequency range. Some of the events show a low percentage of circular polarization (on average $\simeq$ 5%) and others show a relatively high percentage of circular polarization (on average $\simeq$ 20% but up to 60%) at maximum burst intensity.

The Chapter is organized as follows. Observations and data reduction processes are presented in Section 3.2. The dynamic spectra of several type III bursts constructed from Stokes I, V, and $\mid V \mid / I$ images are presented in

Section 3.3. The spatio-temporal profiles of burst sources at 80 MHz revealing source motion and polarization fractions as a function of time and distance, are organized in Section 3.4. The total and circularly-polarized intensity profiles of type IIIs are described in Section 3.5. Section 3.6 describes the circular polarization characteristics of type III bursts: variations of the degree of circular polarization with frequency and position are described in Sections 3.6.1 and 3.6.2, respectively. The linear and logarithmic circularly-polarized flux profiles are described in Section 3.7. The decay time of three burst events is described and compared with existing theory and observation in Section 3.8. Finally, a discussion and conclusions are presented in Sections 3.9 and 3.10.

3.2 MWA Observations and Data Reduction Process

The *Murchison Widefield Array* (MWA) is a low-frequency interferometer in Western Australia (Lonsdale et al., 2009; Tingay et al., 2013a). The observations reported here were obtained using Phase I of the MWA. Technical details and the MWA's overall design are described by Tingay et al. (2013a), and its science targets are outlined by Bowman et al. (2013). The Phase I instrument is composed of 128 "tiles", each containing 16 dual-polarization dipole antennas. The total bandwidth is 30.72 MHz, which can be distributed across the range 80 to 300 MHz, with default time and frequency resolutions 0.5 s and 40 kHz, respectively (Tingay et al., 2013a). Significant amounts of solar research have been done by many authors using MWA observations (Tingay et al., 2013a,b; Oberoi et al., 2014, 2017; Mohan and Oberoi, 2017; Suresh et al., 2017; McCauley et al., 2017, 2018; Cairns et al., 2018; Rahman et al., 2019; Mohan et al., 2019; McCauley et al., 2019).

In our observations, we observe type III radio bursts in the "picket fence" mode, meaning in 12 2.56 MHz wide bands whose centre frequencies range from 80 to 240 MHz. The MWA data are recorded in fine-frequency channels with 0.5 s time and 40 kHz frequency resolution, which we average across 2.56 MHz bandwidths to produce 0.5 s images at 80, 89, 98, 108, 120, 132, 145, 161, 179, 196, 217, and 240 MHz. We used WSClean (w-stacking clean) (Offringa et al., 2014) for imaging with a Briggs −2 (Briggs, 1995) weighting scheme in order to emphasize spatial resolution. The synthesized beam sizes range from ≈ 2.8 arcmin at lower frequencies to less than 1 arcmin at higher frequencies. Our burst data are reduced in the same manner as McCauley et al. (2017) and McCauley et al. (2018).

We note that in order to obtain useful polarization fractions of type III bursts, it is necessary to account for "leakage" of the Stokes I (total intensity) signals into the Stokes V (circular polarization). This problem is described precisely by Lenc et al. (2017) and addressed in detail using the approach of McCauley et al. (2019), as summarized next. Leakage occurs due to differences between the actual instrumental response and the primary beam model used to convert instrumental polarizations into the standard Stokes parameters. These differences may include imperfections in the model itself, along with some instrumental effects, such as individual dipole failures during a particular observing event run, that may cause the true response to vary from that of an otherwise perfect beam model (McCauley et al., 2019). Sutinjo et al. (2015) consider a simple model where inter-element mutual coupling is utilized to measure Stokes Q leakage observed when the array is scanned away from the zenith. Q leakage is therefore identified by the model itself while predicting the imbalance between X (East-West) and Y (North-South) dipoles in 4×4 bow-tie antennas of each tile. The Sutinjo et al. (2015) beam model substantially reduced leakage from Stokes I into Stokes Q but increased the leakage from I into V.

We use a simple algorithm (McCauley et al., 2019) for leakage subtraction that minimizes the number of pixels with polarization fraction greater than 0.5% (*i.e.* $\mid V/I \mid > 0.005$) for quiescent images outside of burst periods, for which thermal bremsstrahlung is expected to dominate and produce polarization fractions $\mid V/I \mid < 0.5\%$. See McCauley et al. (2019) for details on the algorithm and its limitations.

The type III burst data that we analyze are part of an imaging survey of many type IIIs observed by the MWA during 45 separate observing periods in 2014 and 2015 (McCauley et al., 2018). We chose burst events occurring between August 2014 to November 2015 due to the existence of processed data and a catalog produced by McCauley et al. (2019). They focused on non-burst spectro-polarimetric observations of the solar corona and studied circular polarization of low-latitude coronal holes at frequencies 80 to 240 MHz using MWA. We, therefore, selected sixteen sufficiently distinct and locally isolated sets of type III burst events for detailed analysis. The data have been flux calibrated using the same manner described by McCauley et al. (2017).

In order to neglect the noise or unwanted signals in favour of burst emission, the burst images are background subtracted for a whole time period. The background levels for each frequency are estimated by taking the median intensity. It is noted here that the onset of a burst is defined to be when the burst intensity is greater than the background level by a factor of 1.3.

We select our burst events for analysis based on the following criteria: (1) the bursts are isolated in time from other bursts, (2) the burst intensity is at least a factor of 1.3 above background, and (3) the burst has to be present at most frequencies from 80 to 240 MHz. The first criterion ensures that the burst can be generated by a single packet of electrons. The second and third criteria restrict the analysis to bursts for which burst properties can be measured accurately.

Table 3.1 shows the date, onset burst time, duration, source position, and source motion of our bursts chosen for analysis.

3.3 Dynamic Spectra

We construct and display the dynamic spectra for the three type III bursts on 2015/08/25 near 03:14:58 UT, 2015/09/18 near 03:06:08 UT, and 2015/11/11 near 02:32:40 UT (Figure 3.1). The dynamic spectra are background subtracted. The right columns show expanded views of the regions of the selected type III bursts indicated by the vertical dashed lines in the left columns. These type III bursts are relatively isolated and clear. All are relatively slow drift, with the peaks moving from frequencies $\geq$ 200 MHz to 80 MHz in $\approx$ 3 sec.

Figure 3.2 shows the dynamic spectra for the Stokes I (total intensity), V (circular polarization), and V/I (polarization fraction) for the type III burst events of 2015/09/18 and 2015/11/11 shown in Figure 3.1. In order to exclude any emission coming from the background Sun, the background levels are subtracted from the Stokes I and V intensities to make the respective dynamic spectra shown. In contrast the Stokes V/I dynamic spectra are not background subtracted in frequency and time. From Figure 3.2, the dynamic spectra for Stokes V are relatively smaller in magnitude and narrower than for Stokes I. The intensity in polarized emission found in the dynamic spectra is less than that of the total emission. We find maximum polarization fractions ($\mid V \mid/I$) equal to 0.3 and 0.6, respectively, for the two burst events. Based on previous work (Benz and Zlobec, 1978; Dulk and Suzuki, 1980; Suzuki and Dulk, 1985), these values are too large for harmonic plasma emission and point towards the burst emission being at the fundamental of the plasma frequency.

We examine the type III burst events to make sure whether they exhibit fundamental-harmonic structure or and structureless. Figures 3.3 and 3.4 show

Table 3.1

Type III bursts chart					
Date	Start time (UT), Duration (s)	Position	Motion	% of polarization at burst onset (Figure 3.12)	% of polarization at burst maximum (Figure 3.12)
2014/08/26	03:49:21.20, 5	East limb	Yes, outward	Min:4.1, Max:34.6	Min:0.1, Max:3.3
2014/08/28	03:05:19.70, 5	East limb	Yes, outward	Min:0.2, Max:60.3	Min:0.2, Max:14.6
2014/09/15(a)	03:34:18.70, 5	West limb	Yes, outward	Min:3.0, Max:29.3	Min:0.3, Max:31.9
2014/09/15(b)	06:25:58.20, 4	Large radial height	No	Min:11.1, Max:37.7	Min:0.9, Max:21.6
2014/09/16	06:23:38.60, 3	East limb	Yes, limited motion	Min:1.6, Max:11.5	Min:2.1, Max:10.3
2014/09/26(a)	06:27:10.10, 3	Disk center	No	Min:1.2, Max:12.7	Min:0.5, Max:6.3
2014/09/26(b)	06:58:16.70, 5	Disk center	No	Min:28.2, Max:49.8	Min:8.6, Max:34.0
2014/10/14	03:05:18.70, 3	Large radial height	No	Min:2.1, Max:58.6	Min:0.4, Max:24.0
2015/08/25	03:14:58.70, 6	Disk center	No	Min:11.1, Max:37.7	Min:0.9, Max:21.6
2015/09/03(a)	01:55:02.70, 5	Disk/East limb	No	Min:0.5, Max:14.7	Min:0.4, Max:12.4
2015/09/03(b)	02:10:37.20, 4	Partial on disk	Yes, limited motion	Min:0.1, Max:6.6	Min:1.0, Max:15.0
2015/09/18	03:06:08.20, 6	Disk/West limb	Yes, outward	Min:5.3, Max:15.3	Min:13.6, Max:47.6
2015/10/27	02:55:33.70, 6	Large radial height	Yes	Min:0.2, Max:1.6	Min:0.1, Max:0.6
2015/10/29	02:06:06.20, 3	Large radial height	Yes	Min:7.2, Max:15.2	Min:2.9, Max:11.9
2015/11/04	01:32:58.70, 4	West limb	Yes, outward	Min:1.3, Max:56.3	Min:0.2, Max:4.6
2015/11/11	02:32:40.20, 6	Disk center	No	Min:13.4, Max:46.8	Min:10.7, Max:59.9

the light curves for the logarithmic intensity of the two type III events on 2015/09/18 and 2015/11/11 at frequencies ranging from 240 to 80 MHz. These examples do not have any signatures of simultaneous fundamental and harmonic emission, such as two peaks in the time profiles of a single burst at a given frequency f (first fundamental and then harmonic) in the intensity light curves. It is noted here that the data we used have a time resolution of 0.5 s, which may not be sufficient to distinguish fundamental-harmonic structures. Before we suggest that the burst events we analyze exhibit fundamental emission near burst onset and a mixture of fundamental and harmonic emission near the times of peak intensity.

3.4 Spatio-temporal Profiles of Type III Burst Source

We now analyze burst source motions and distance-time profiles for the two burst events in Figure 3.5, which shows 80 MHz images in Stokes I, V, and $|V|/I$ on 2015/08/25 near 03:15:02 UT (top panels) and on 2015/09/18 near 03:06:12 UT (bottom panels), both of which had source motion. It is noted that we restrict our analyses of the source motion and distance-time profiles at the lowest frequency but we also observe source motion of two events at higher frequencies $\geq$ 132 MHz which is not presented here. However, the red arrows show the directions of source motion, and the red lines correspond to the slices used to make the distance-time plots shown in Figure 3.6. The Stokes $|V|/I$ images in Figure 3.5 show that for each burst source a smaller polarization fraction is seen toward its back (tailing edge) side and a larger polarization fraction is observed toward the front (leading edge) side of the burst source in the direction of source motion.

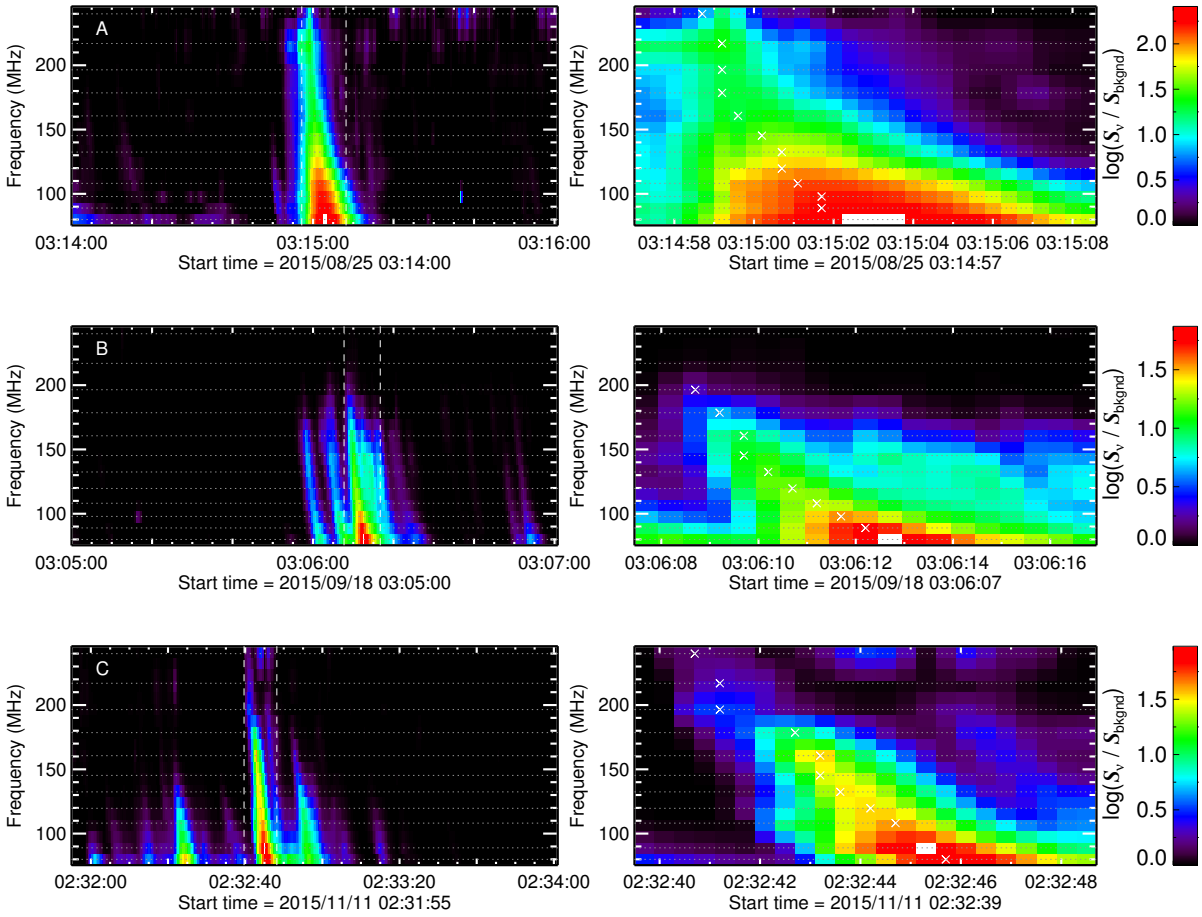

Figure 3.1: Dynamic spectra made from image intensities for the type III bursts near 03:14:57 UT on 2015/08/25 (row A), 03:06:07 UT on 2015/09/18 (row B), and 02:32:39 UT on 2015/11/11 (row C), respectively. The left columns show 2-min observing intervals, while the right columns indicate ≈ 10 s time periods surrounding the selected type III bursts (bounded by the vertical dashed lines in left columns), respectively. The horizontal dotted lines show the entire frequencies of the 12 channels that each have a spectral width of 2.56 MHz. The white crosses indicate peak burst times for each frequency channel. Intensities are divided by the background level and plotted on a logarithmic scale.

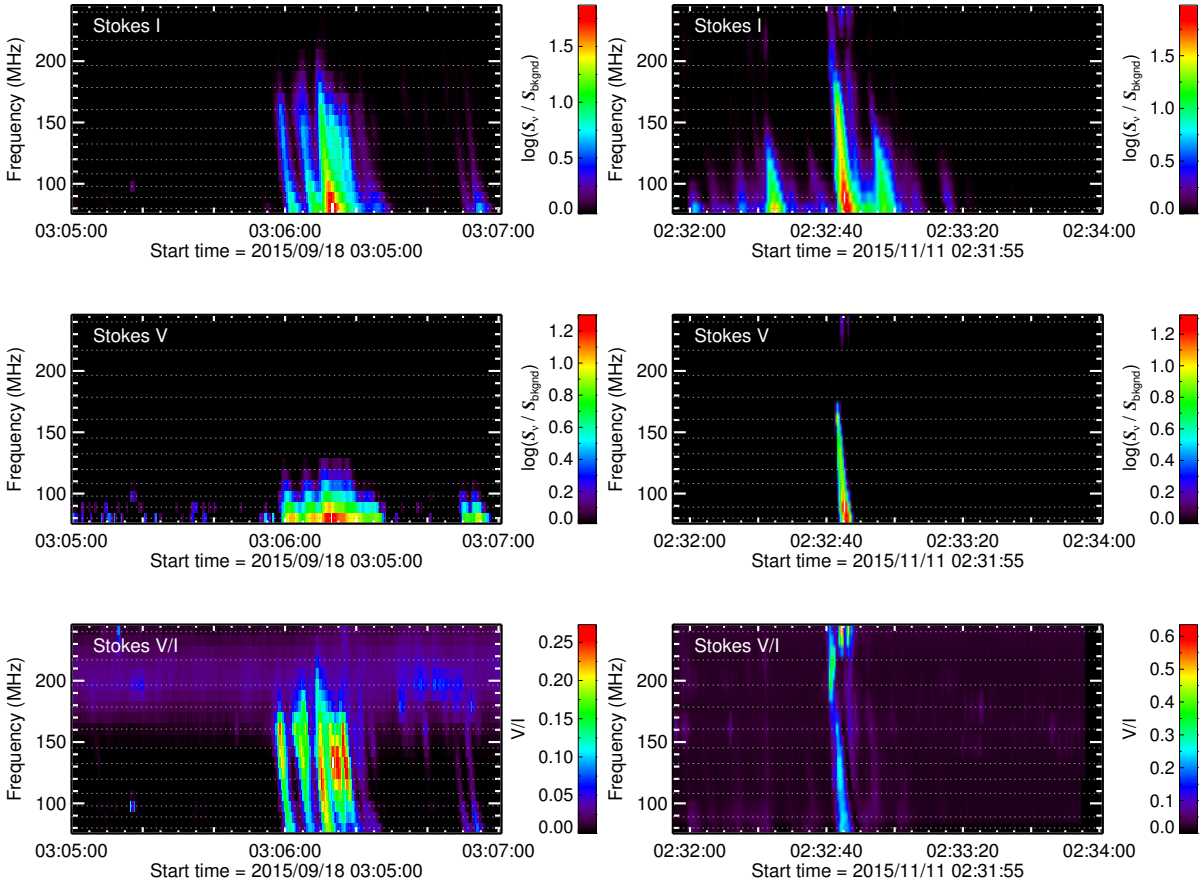

Figure 3.2: Dynamic spectra made from image intensities for Stokes I, V, and $|V|/I$ for the two type III events on (left) 2015/09/18 and (right) 2015/11/11, respectively. Plot axes and annotations are same as in Figure 3.1.

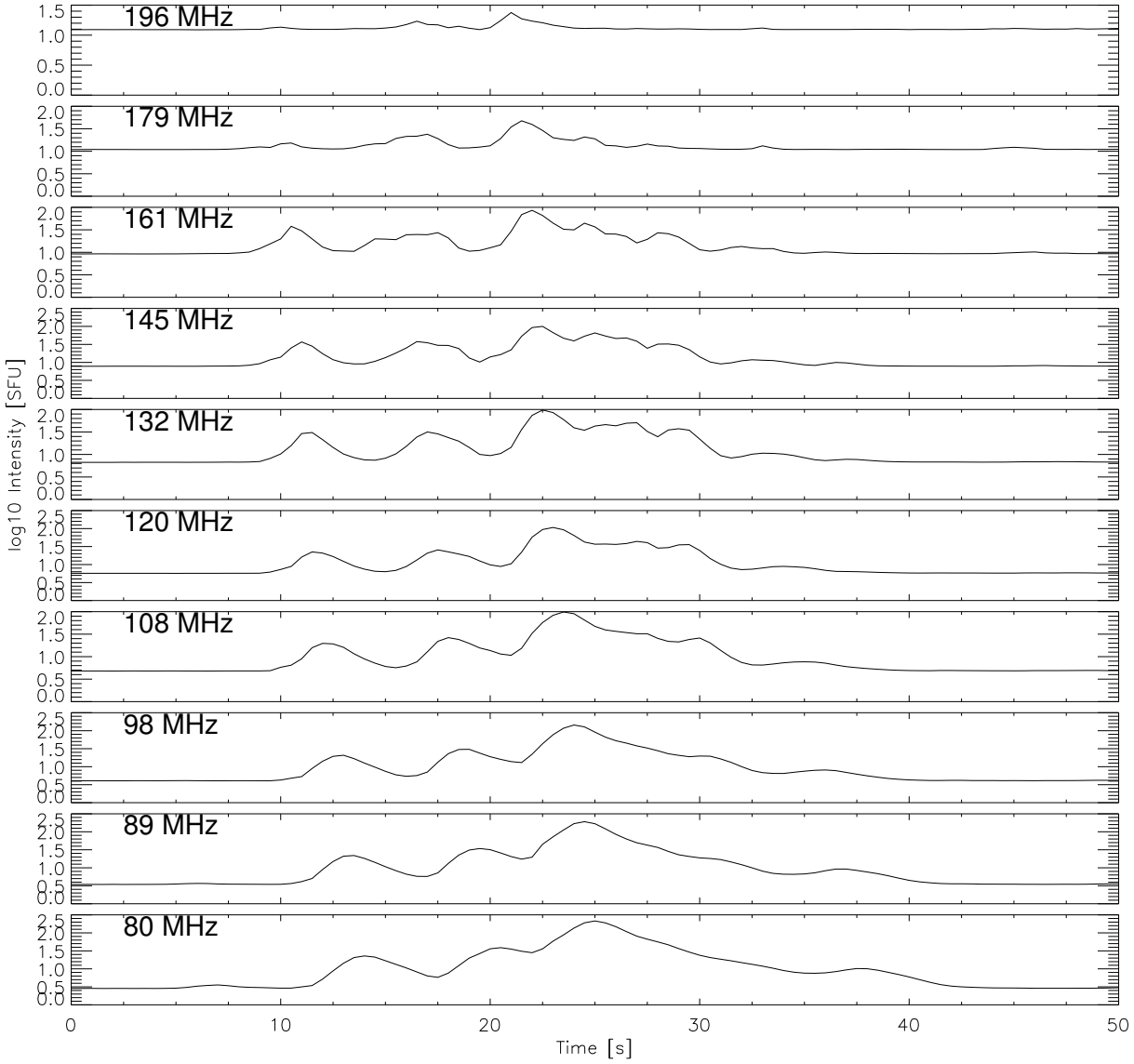

Figure 3.3: Logarithmic intensity plots of type III burst on 2015/09/18 for 10 frequencies (from top to bottom panel): 196, 179, 161, 145, 132, 120, 108, 98, 89, and 80 MHz, respectively.

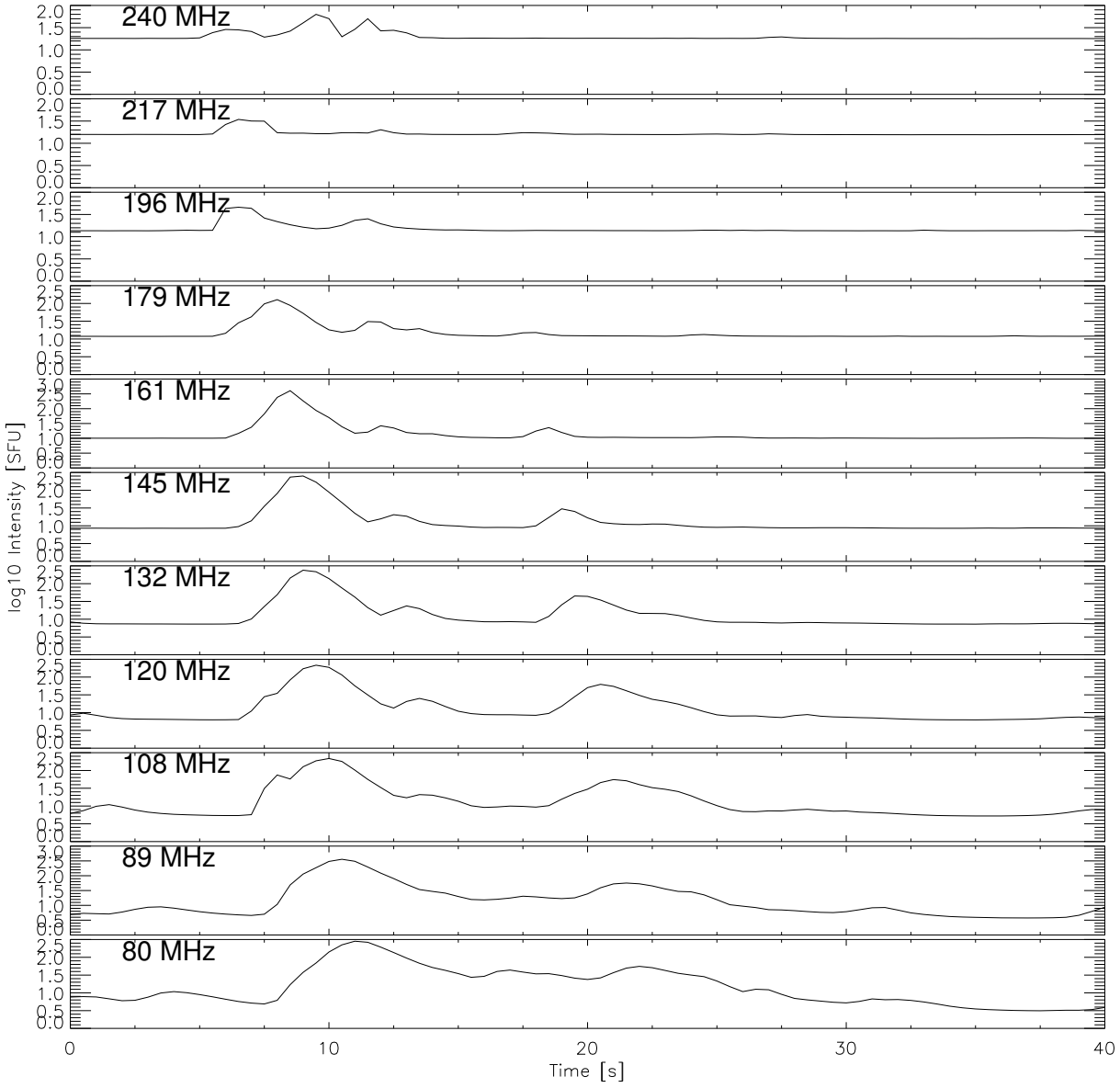

Figure 3.4: Same as Figure 3.3 but type III burst on 2015/11/11 for 11 frequencies (from top to bottom panel): 240, 217, 196, 179, 161, 145, 132, 120, 108, 89, and 80 MHz, respectively.

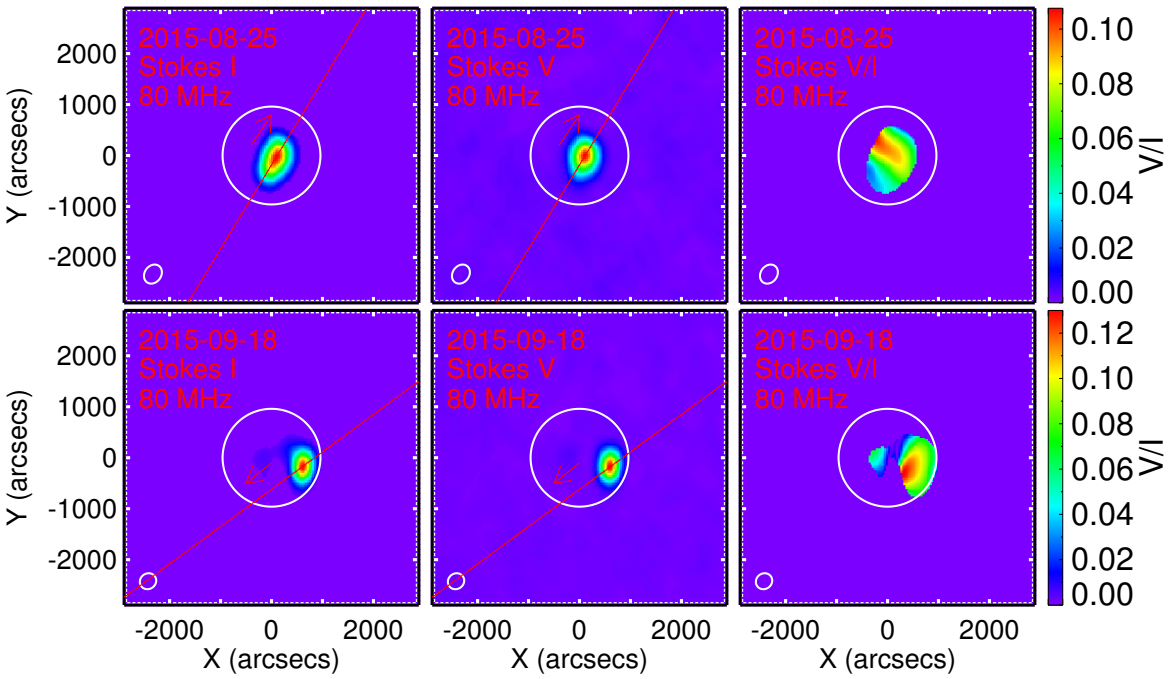

Figure 3.5: Top panels: 80 MHz images of Stokes I, V, and $\mid V \mid / I$ for the type III burst with source motion on 2015/08/25 near 03:15:02 UT where the red colored lines correspond to the slices used for distance-time profiles shown in top row of Figure 3.6. Bottom panels: Same as the top panels but for the type III burst with source motion on 2015/09/18 near 03:06:12 UT. The directions of burst source motion are indicated by the red arrows.

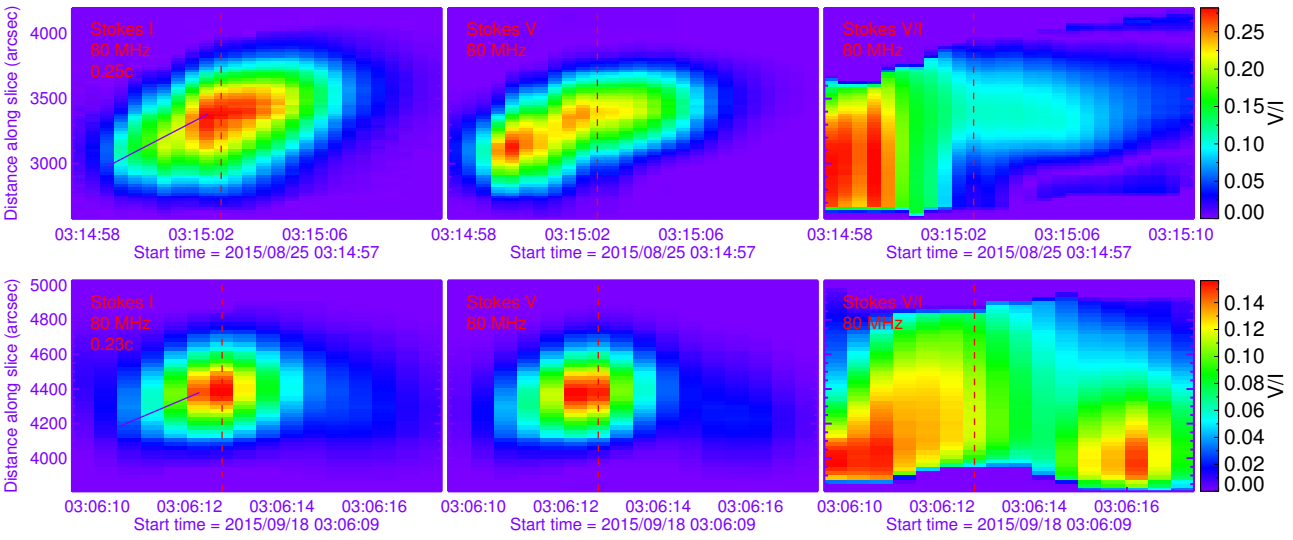

Figure 3.6: Distance-time profiles at 80 MHz for Stokes I, V, and $\mid V \mid / I$ for the type III bursts with source motion (top) on 2015/08/25 and (bottom) on 2015/09/18. These are constructed by stacking image strips at different times along the slices shown in Figure 3.5 (first two columns). The red colored vertical dotted lines represents the slices taken at the times in the top panels of Figure 3.5. The violet solid lines are a Polynomial fit to measure the speed of the burst source that goes through the maximum intensity values for each column of slice images.

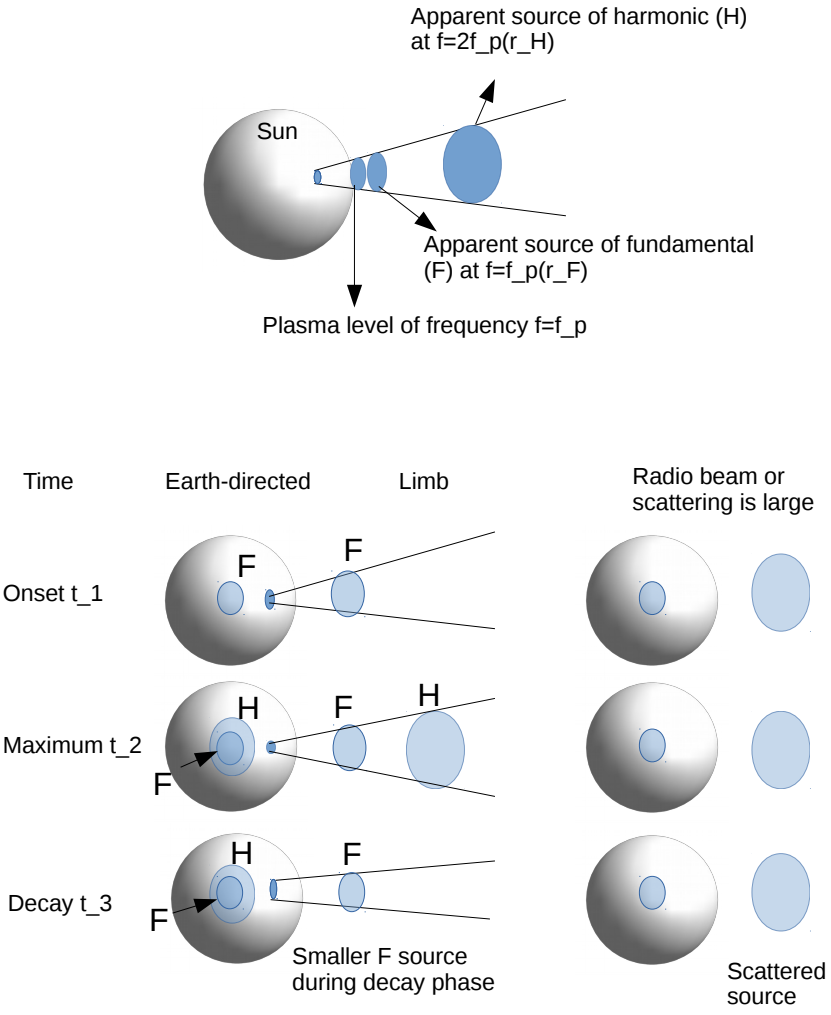

Figure 3.7: Cartoon representation of F and H sources and their associated plasma levels. The Earth-directed sources are shown (bottom left column) at three different times namely, burst onset t_1, burst maximum t_2, and decay phase t_3. The scattered source is shown as a single source (bottom right column) as being considered large radio beam or scattering.

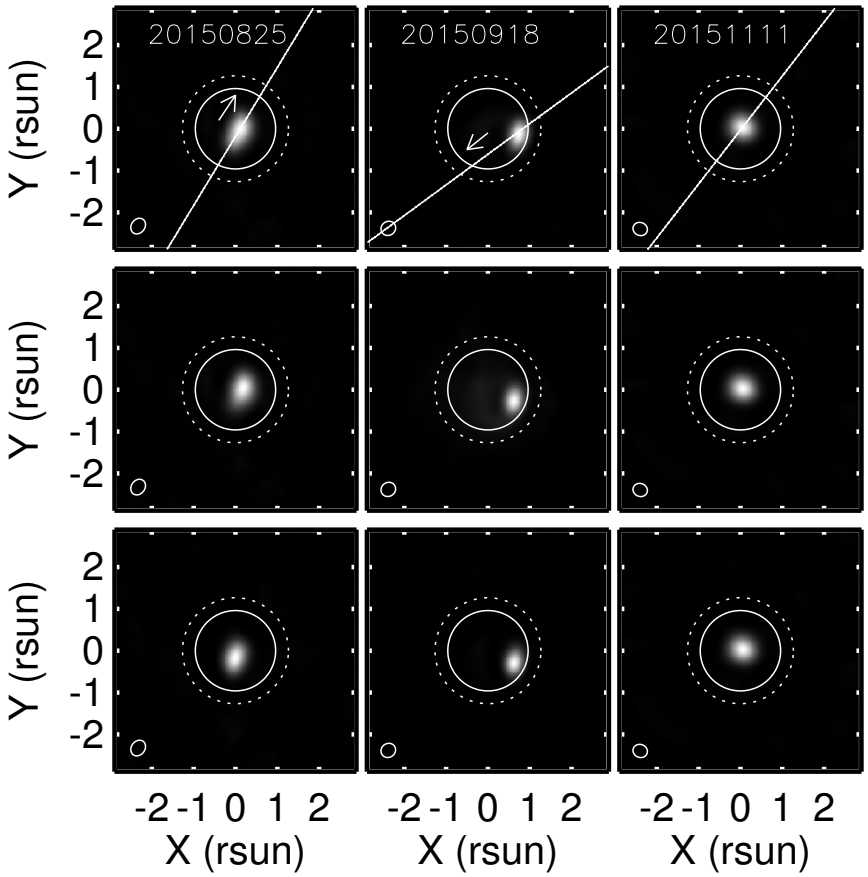

Figure 3.8: 80 MHz Stokes I images of burst sources obtained from MWA with 0.5 s time interval starting near 03:15:02 UT on 2015/08/25 , 03:06:12 UT on 2015/09/18, and 02:32:45 UT on 2015/11/11 (from top to bottom panel of each column) where the white lines correspond to the slices used for normalized intensity plots shown in Figures 3.9, 3.10, and 3.11, respectively. The directions of burst sources motion are indicated by the white colored arrows. The inner solid circles indicate the optical disk, and the outer dotted circles indicate the height of the plasma layer for a given frequency in the Newkirk (1961) density model. The ellipses at the lower left corners indicate the MWA synthesized beam sizes.

We now use the slices in Figure 3.5 to make distance-time images of the total intensity I, polarized intensity V, and polarization fraction $\mid V \mid/I$ of two type III sources along the direction of source motion, which are shown in Figure 3.6. These images are constructed by taking the strip of images like Figure 3.5 for a given time along the red line and then plotting the strip for next time sample vertically beside the first one, and then iterating. In order to exclude all possible noise signals from Stokes I and V images, we consider only pixels with signal-to-noise ratios above 10 σ.

We see in the Stokes I image from the first panel of Figure 3.6 (top row) that the burst source elongates along the direction of source motion with a speed $\approx$ 0.25c (where c is the speed of light), as shown by the violet line. This speed is similar to the speeds found in similar distance-time analyses by McCauley et al. (2017, 2018). The burst source in Stokes I has a larger width than in Stokes V at the time corresponding to the slice (indicated by the vertical red dotted line) and after that the source becomes narrower and weaker in intensity as time goes on. Clearly the source remains larger in Stokes I than in Stokes V at all times.

The distance-time profile of Stokes $\mid V \mid/I$ shows that polarization fraction is larger at the beginning of the burst ($\geq$ 0.25) for a couple of seconds. The source then becomes weaker in polarization fraction, ranging from 0.2 to 0.1, for several more seconds. After this, the burst source becomes increasing less polarized, with polarization fraction smaller than 0.1, with time until the end of the burst.

The burst source in the second event has an elongation speed $\approx$ 0.23c at 80 MHz and is more compact in Stokes I and V (bottom row of Figure 3.6) than the first event. From the distance-time profile of Stokes $\mid V \mid/I$, a clearly larger polarization fraction is found at the beginning of burst source ($\geq$ 0.14) decreasing to 0.07 in the middle of the time period. After that, the burst source exhibits relatively large polarization fraction at the end of the event.

By analyzing both of the Stokes $\mid V \mid/I$ images for burst sources depicted in the third column of Figure 3.6, we propose dominance of F radiation at the beginning of burst emission, with a higher polarization fraction, and afterward when the burst is near maximum intensity both F and H may contribute and so lead to a lower polarization fraction (Dulk et al., 1984; Robinson et al., 1994; Robinson and Cairns, 1998). During the decay phase of the burst, F radiation dominates again but the polarization fraction of the source becomes weaker due to the scattering effects that depolarize the emission (Robinson, 1983; Robinson and Cairns, 1998). The theory of Robinson and Cairns (1998) predicts this phenomenon in which scattering effects and loss by linear mode conversion cause exponential decay of F emission as it travels radially outward from a source located at a particular height in the corona. Scattering and linear mode conversion can also cause a decrease in the polarization of F emission, whether due to scattering off relatively sharp density irregularities (Hayes, 1985a,b) or by linear mode conversion (Kim et al., 2007, 2008).

In order to represent the F and H sources schematically, we show a cartoon in Figure 3.7. We consider the frequency associated with the plasma emission level is $f = f_p$ and F source originates at $f = f_p$ whereas the H source at $f = 2f_p$ (image shown in top). Our data are for a constant frequency as a function of time where the source is at different locations at different times namely, burst onset t_1, burst maximum t_2, and decay phase t_3 (lower left column). As mentioned in earlier and to match with the pattern of emission of a burst at different times, we propose that at t_1, dominant F emission releases with a contribution of larger polarization fraction. During t_2, both F and H emission contribute to the bursts and so lead to a lower polarization fraction. At t_3, F radiation dominates again but the polarization fraction of the source becomes weaker due to the scattering effects that depolarize the emission. It is noted here that we can not distinguish the F and H sources on the basis of position

measurements as suggested by Dulk and Suzuki (1980), and as likely to be shown in the cartoon (lower left column) because, at a given frequency, the positions of F and H sources always nearly coincide (Smerd et al., 1962; Bougeret et al., 1970). Importantly, instead of observing both components of the source, we only capable to observe a single scattered source if the radio beam is large or scattering is more prominent in the source and along the path (lower right column). Therefore, the cartoon representation and imaging results (Figure 3.6) are consistent with the theory predicted by Robinson and Cairns (1998).

3.5 Total and Circularly Polarized Intensities

Now we study the spatial profiles of the total and circularly polarized intensities of three type III events at different frequencies, two with source motion (on August 25, 2015 near 03:15:02 UT and on September 18, 2015 near 03:06:12 UT) and one with no source motion (on November 11, 2015 near 02:32:40 UT). We took a slice through each of the burst sources at times when the total intensity of bursts is maximum (Figure 3.8). Figures 3.9, 3.10, and 3.11 show the normalized total and circularly polarized intensities as a function of the position along the slice.

Figure 3.9 shows the profiles at 80, 120, 145, and 161 MHz for the type III burst on August 25, 2015, near 03:15:02 UT when the total intensity was maximum. The direction of source motion is displayed by the white colored arrow in the first panel in the upper row of Figure 3.8, this direction determines the positive direction for the distance axis in Figure 3.9. We normalize the Stokes I (total intensity), V (circular polarization), and $|V|/I$ (polarization fraction) parameters by dividing by their corresponding maximum values. We see from Figure 3.9 that the profiles of the normalized I and V plots are qualitatively very similar at the four frequencies, becoming narrower and smoother as frequency

increases. It is emphasized here that the $|\ V\ |/I$ profiles are qualitatively different from the V and I profiles at all frequencies. In particular, the $|\ V\ |/I$ profiles are not symmetric about their peaks but the V and I profiles are almost symmetric. The asymmetric profiles for $|\ V\ |/I$ at any frequency are evidently due to the source moving. Specifically, the burst source is located near the disk center and the $|\ V\ |/I$ profile has a peak in the direction along which the source moves (North-West direction) and a tail in the opposite direction. The $|\ V\ |/I$ profiles thus show a gradual increase in the direction that the burst source moves.

Figure 3.10 is analogous to Figure 3.9 but is for the type III burst on September 18, 2015 at 03:06:12 UT, near its maximum intensity. The direction of source motion is shown in the second panel in the upper row of Figure 3.8. Once again, the shapes of the I and V profiles are almost identical and symmetric at all frequencies but the $|\ V\ |/I$ plots exhibit a similar trend but flipped in X from those in Figure 3.9. That is, the $|\ V\ |/I$ profiles are not symmetric about their peaks but instead peak in the direction of burst motion and have a tail in the opposite direction. Note that in this case the burst source is located near the West solar limb, and the burst source moves inward towards the disk center, in the negative X direction (towards negative distance along with slice from centroid).

Figure 3.11 shows the normalized I, V, and $|\ V\ |/I$ profiles at 80, 120, 145, and 161 MHz for the type III burst on November 11, 2015, near 02:32:45 UT, that shows no source motion. We see from Figure 3.11 that the profiles of the normalized Stokes I, V, and $|\ V\ |/I$ plots are now almost symmetric at all frequencies, with $|\ V\ |/I$ peaking where I and V do.

Combining these results with Section 3.4, Figures 3.5−3.11 are all consistent with the fronts of the type III electron beams having higher polarization and so being fundamental emission. They also provide support for lower polarization

for slower regions of the beam whether intrinsic to the emission or due to release of previously generated and partially depolarized emission.

3.6 Analyses of Circular Polarization Characteristics

In this Section, we study the degree of circular polarization of sixteen type III burst events between August 2014 and November 2015 (Table 3.1). The variations of the degree of circular polarization with frequency and position are briefly discussed in Sections 3.6.1 and 3.6.2, respectively, both near event onset and near maximum intensity.

3.6.1 Variations of Degree of Circular Polarization with Frequency

Figure 3.12 shows the degree of circular polarization of those type III bursts as a function of frequency near event onset (when the intensity exceeds 1.3 times the background) and at the time of maximum intensity. First, on average the polarization fractions are typically much larger near event onset than at event maximum for all frequencies. Second, on average circular polarization fractions increase as frequency increases at both event onset and event maximum. Third, we see that at event onset, the degree of circular polarization is found to be $< 40\%$ for the majority of burst events and only a few of them show $> 40\%$ at higher frequencies. On the other hand, at event maximum, the circular polarization is found to be $< 20\%$ for majority of the events. Fourth, frequency-averaged polarization fractions of all the events as shown in Figure 3.13, on average event onset exhibits an increase in circular polarization ranging from 9% at 80 MHz to 22% at 240 MHz, whether event maximum exhibits an average

tendency to increase in polarization ranging from 5% at 80 MHz to 20% at 240 MHz. Fifth, we see that the uncertainty is relatively lower at lower frequencies but higher at some higher frequencies for most of the events (Figure 3.12).

We note that the leakage subtraction algorithm that we used accounts for the amount of signal leaking into the Stokes V from Stokes I. There is also a possibility for the Stokes V signal to leak into the I signal. We suspect this is one of the reasons for a few burst events having higher polarization fractions at higher frequencies (Figure 3.12). The uncertainty measurements for those higher polarization fractions at different frequencies include three effects: 1) signal leaking from Stokes V into I, 2) contributions of noise (σ) in both Stokes I and V, and 3) variability of leakage algorithm, as quantified by McCauley et al. (2019). Hence, our polarization fractions are somewhat biased due to these effects. Despite the uncertainties, the results that polarization fractions greater than 0.25 are common.

3.6.2 Variations of Degree of Circular Polarization with Position

We now study the position dependence of the degree of circular polarization, as shown in Figure 3.14 for all the events as a function of the source's X coordinate, separately near onset and near maximum intensity. First, the burst events in our sample include some near the disk center and more near the limb and beyond. Second, we see that most events show $\mid X \mid$ increasing as the frequency decreases, at both event onset and event maximum, which is consistent with burst sources having motion that is radially outward on average. Third, at both event onset and maximum intensity, the average polarization fraction is found to be larger for the source's X coordinate located near disk center and relatively smaller circular polarization is obtained near the limb.

We then consider the dependence of the percentage of circular polarization on the source's Y coordinate, as shown in Figure 3.15. First, most events do not show $\mid Y \mid$ increasing as frequency decreases on average as compared to the increase in $\mid X \mid$ shown in Figure 3.14. Second, at both event onset and maximum intensity, the average polarization fraction is found to be larger when the source's Y coordinate is located near disk center and relatively smaller near the limb (this is clearest near burst maximum).

Figure 3.16 plots the polarization fraction as a function of radial distance r from the Sun's center, again separately near event onset and maximum intensity. First, the polarization fraction increases as frequency increases for many but not all events at burst onset and maximum. Second, we see a higher degree of circular polarization on average near the disk center and a relatively lower degree of circular polarization near the limb during onset and maximum intensity (top panels). Third, it is clear that the frequency-averaged polarization fraction decreases as we move from the Sun center to near the limb (bottom panels). It is noted that the number of burst events we analyzed is smaller near the disk center than near the limb.

Observationally, the position dependence of polarization of type III bursts have been reported by Dulk and Suzuki (1980) at 80 and 43 MHz using the *Culgoora Radioheliograph*. For fundamental emission, they found maximum 60% degree of circular polarization near the disk center and 10% near the limb at 80 MHz. On the other side, similar percentage of circular polarization was found near the disk center but 5% near the limb at 43 MHz. In our case, type III bursts show frequency-averaged degree of circular polarization of 38% when the burst source is near the disk center and 9% near the limb at onset. These percentages are 35% and 6% near burst maximum. Thus our results are consistent with the observations of Dulk and Suzuki (1980), though we considered only a small number of type III events.

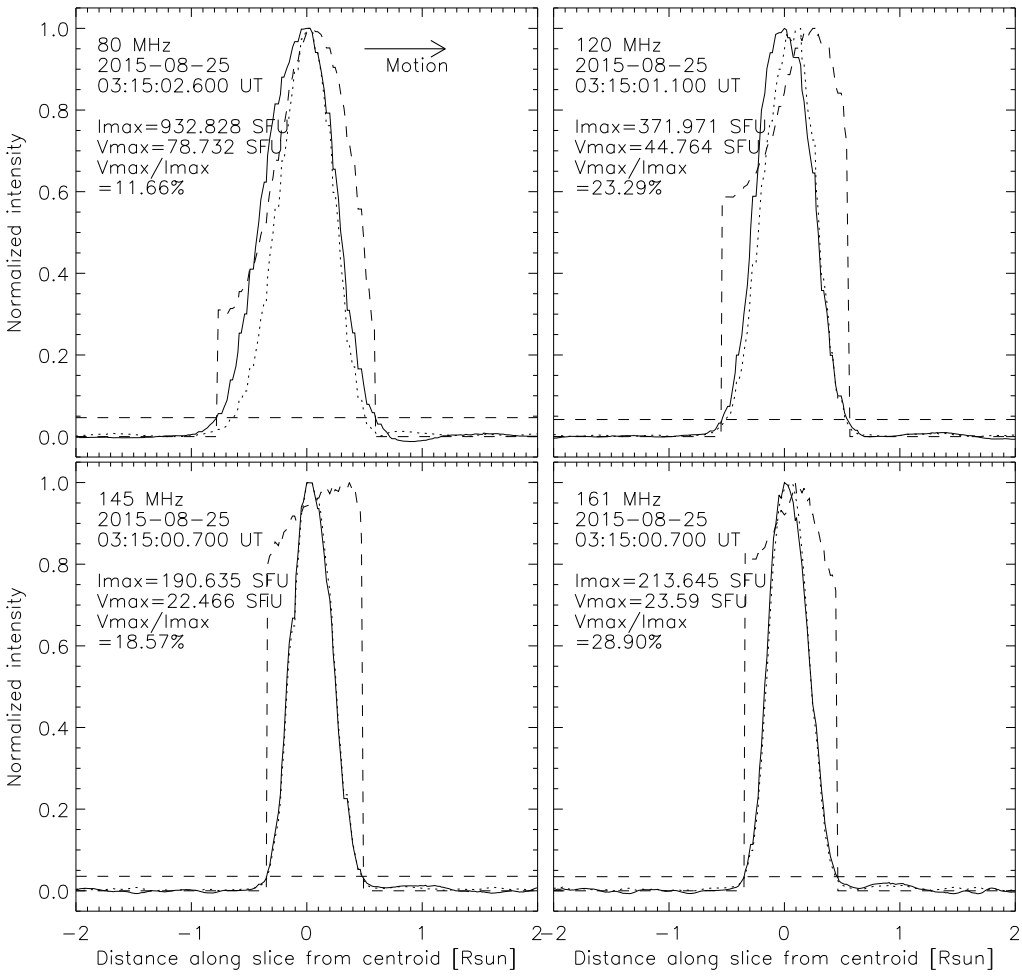

Figure 3.9: Stokes I (solid curve), V (dotted curve), and $|V|/I$ (dashed curve) intensity plots at four different frequencies as functions of the distance along the slice in Figure 3.8 for a type III burst on 2015/08/25 with source motion. The black arrow indicates direction of source motion. The horizontal dashed line indicates the 10σ threshold level, where σ stands for the signal to noise ratio.

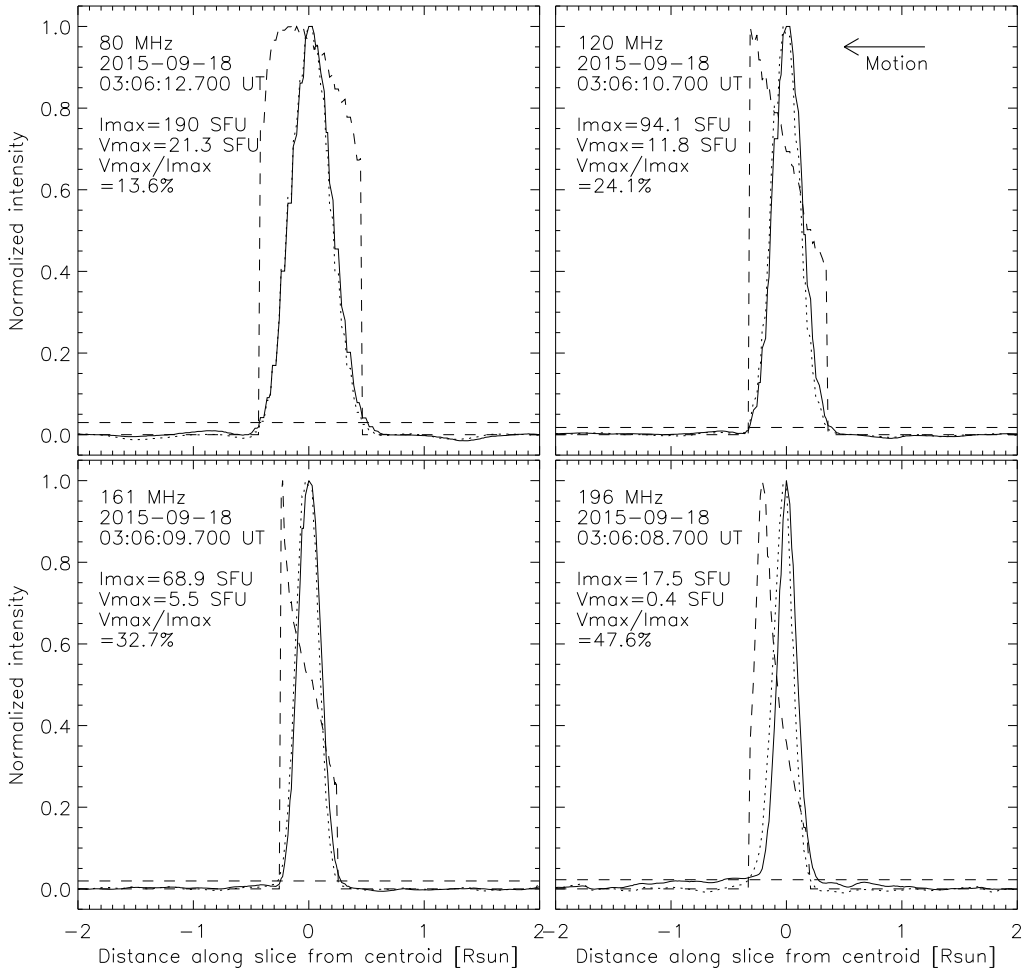

Figure 3.10: Same as Figure 3.9 but for the type III burst with source motion on 2015/09/18.

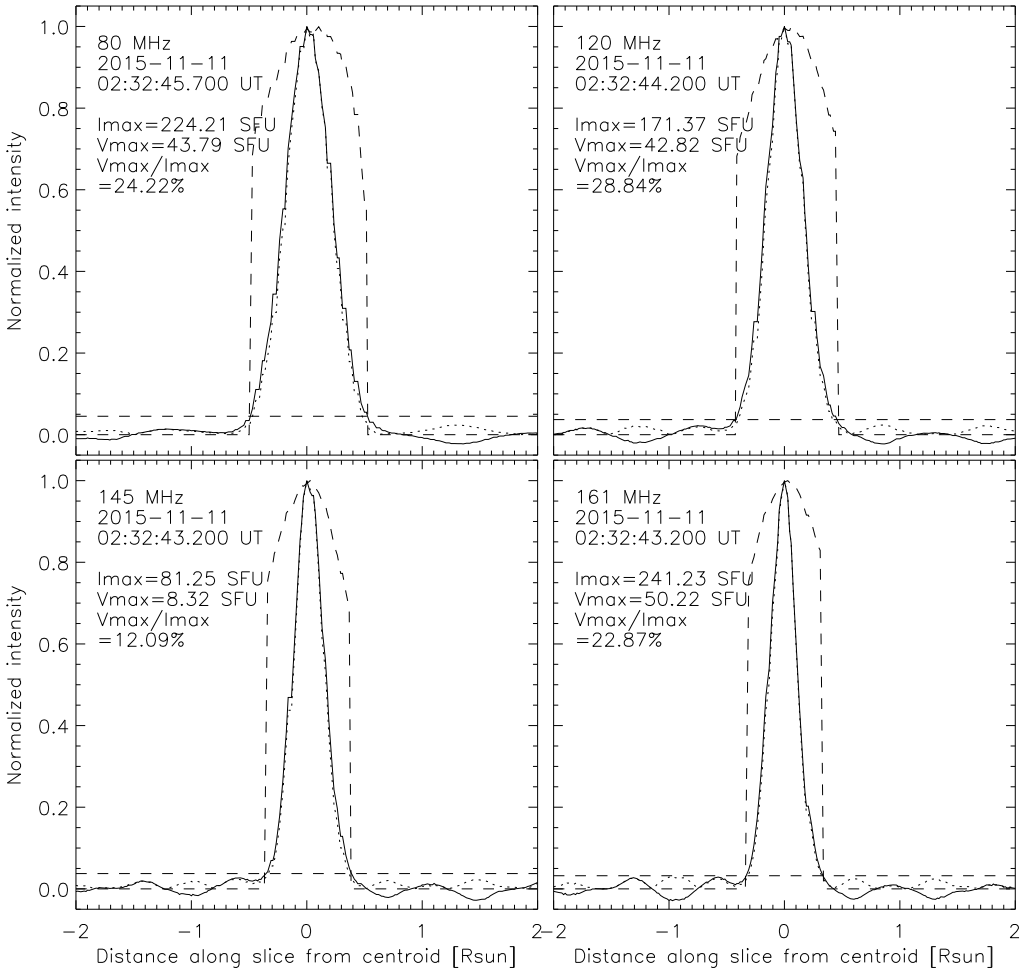

Figure 3.11: Same as Figure 3.9 but for a type III burst without source motion on 2015/11/11.

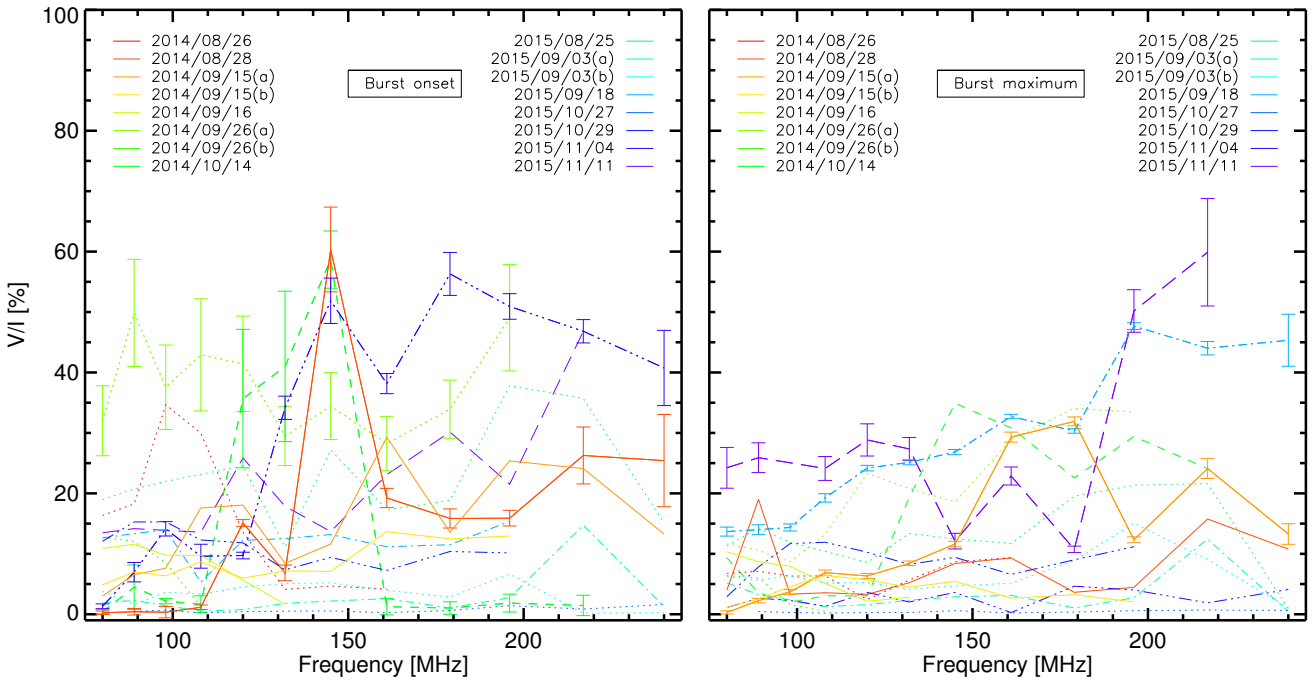

Figure 3.12: Variation of the degree of circular polarization with the frequencies range from 80 to 240 MHz for sixteen isolated type III radio bursts near (left) the burst onset and (right) maximum, respectively. Different colored lines indicate different events as identified in Table 3.1. The error bars indicate uncertainty measurements for few events with higher polarization fraction.

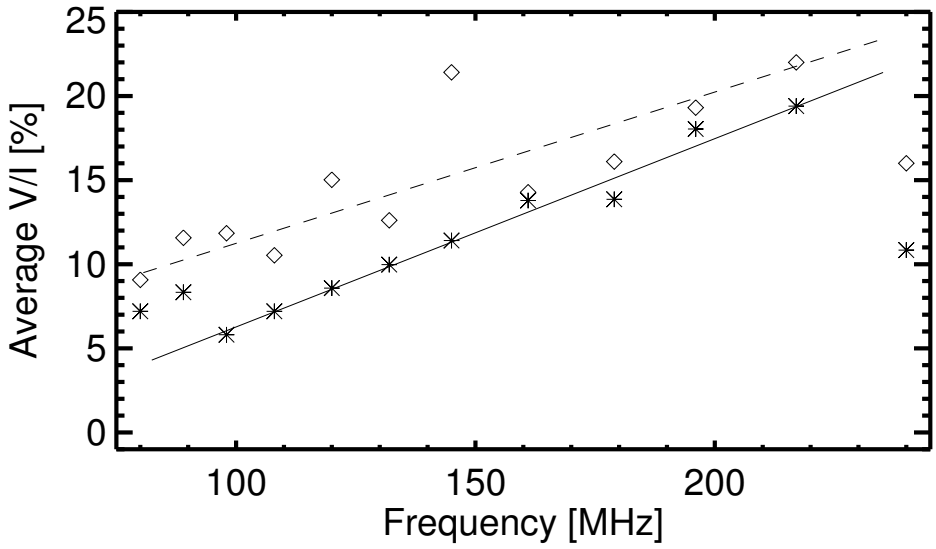

Figure 3.13: Frequency-averaged degree of circular polarization for the same events as in Figure 3.12. The dashed and solid straight lines indicate the least square fits through the average values at burst onset and maximum, respectively.

3.7 Variation of the Circularly Polarized Flux with Time

Figure 3.17 shows the time-varying total and circularly polarized fluxes of type III events on September 18, 2015, near 03:06:13 UT and on November 11, 2015, near 02:32:46 UT, respectively. Typically (but not always) the temporal profiles of the total flux and circularly polarized flux are very similar in our data. However, the maxima of the total and circularly polarized fluxes of the first set of bursts do not coincide with each other. In fact, the circularly polarized flux peaks before the total flux. However, this type of temporal offset does not occur for all the burst events: for the second event the maxima in I and V are simultaneous (bottom panel in Figure 3.17). Most bursts in our study are intermediate between the two sets of examples of Figure 3.17.

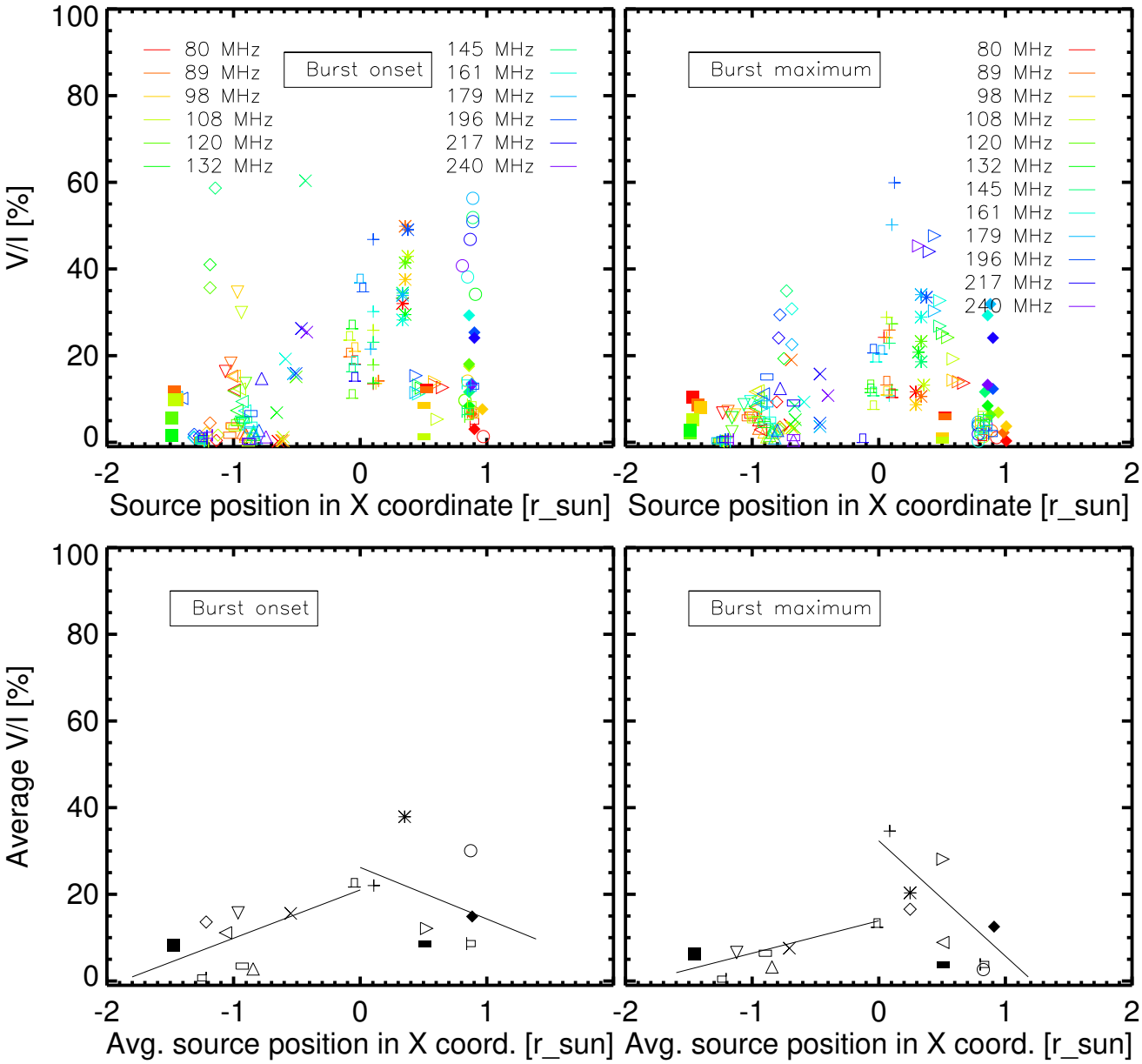

Figure 3.14: (Top panels) Variation of the degree of circular polarization with the X coordinate of the source position for our 16 type III events between 80 and 240 MHz near burst onset (left) and maximum (right). (Bottom panels) Variation of the frequency-averaged degree of circular polarization with the averaged X coordinate of the source position for each type III. Different symbols indicate different burst events, as identified in Table 3.1. The straight lines indicate the least square fits through the average values.

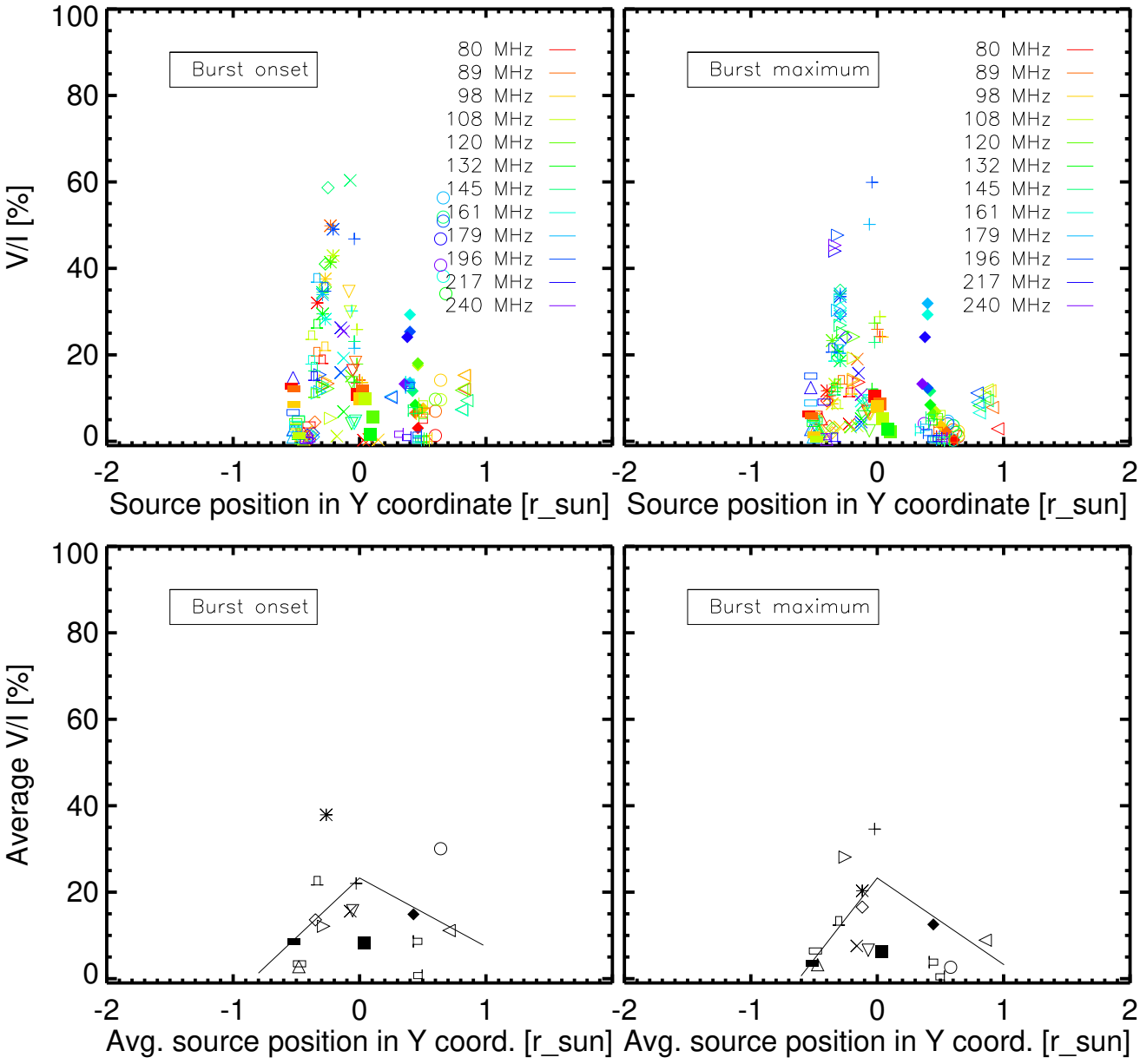

Figure 3.15: Same as Figure 3.14 but for the variations in the degree of circular polarization with source Y coordinate. The straight lines indicate the least square fits through the average values.

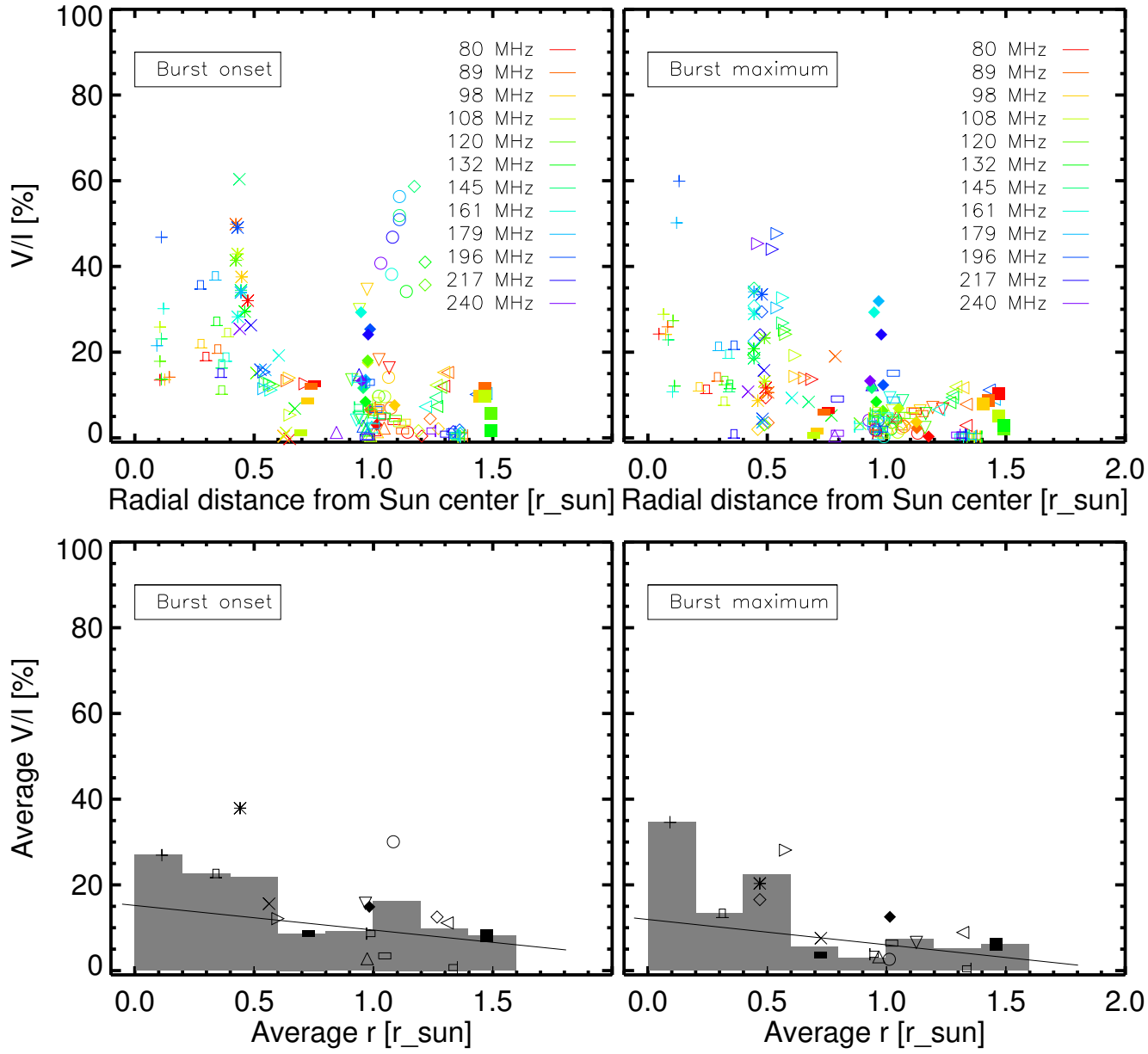

Figure 3.16: (Top panels) Variation of the degree of circular polarization with radial distance r (where r = $\sqrt{X^2 + Y^2}$) from the Sun's center. (Bottom panels) Variation of the frequency-averaged degree of circular polarization for each event with the average of r for each event. Each bin has width of 0.2 r_{sun}. The straight lines indicate the least square fits through the average values.

We note that the sense of circular polarization (left hand or right hand) does not change over frequency and time during a burst extent, consistent with the results in Figures 3.12 and 3.17. This indicates a particular mode of burst emission, either ordinary (o)- or extraordinary (x)-mode prevails for both F and H components. Based on the polarization measurements, it is generally accepted that the burst radiation is o-mode. Theory predicts that F emission is o-mode because the x-mode is blocked (Kai, 1970; Melrose and Sy, 1972). Observations find that the sense of polarization of type III bursts originating from a particular active region is the same as that of type I burst source (Kai, 1970; Kai and Sheridan, 1974), the later is known to be o-mode (Dulk and Nelson, 1973). Type III polarization is related to the polarity of the dominant spots in active region and the sense of polarization in the field associated with the spots corresponds to o-mode (Dulk and Suzuki, 1980). We consider our burst emission is likely to be o-mode as suggested by Dulk and Suzuki (1980).

Our results regarding the total and circularly polarized flux profiles agree well with the results of Mercier (1990), who investigated the one dimensional total and circularly polarized flux for two burst events in their Figure 1a−b. As we find, the maximum of the polarized flux often precedes the maximum of the total flux (Mercier, 1990) but does not follow it. We also confirm Mercier's (1990) result that the sense of circular polarization (left hand or right hand) does not alter during a burst over time.

Alvarez and Haddock (1973a) and Evans et al. (1973) studied the temporal decay of type III radiation, finding exponential decay with a time constant t_d proportional to $f^{-0.95\pm0.1}$ and $f^{-1.09\pm0.05}$, respectively. In order to generalise these analyses to both circular polarization and to the domain 80−240 MHz, we now study the time variations of the logarithmic total and circularly polarized fluxes of type III bursts (for the two events in Figure 3.17) as shown in Figure 3.18. We see for both sets of events the total flux exhibits a slow exponential

decrease over time after the time of peak flux (solid curves). In contrast, the polarized flux shows a relatively faster exponential decrease over time than the total flux (dotted curves). Indeed, there is weak evidence that the decay is faster than exponential at long times, due to the lack of a single straight line in $log_{10}V(t)$ after 02:32:47.0 UT in the bottom panel of Figure 3.18.

Benz et al. (1982) reported such an event where they found that the degree of polarization reached its maximum before the maximum intensity. This could happen after the mode conversion, where o-mode waves travel faster and reaches us first. That results naturally in a "spike polarization" which means polarization is maximum before maximum intensity (Santin, 1976; Benz and Zlobec, 1978). The polarized emission falls off more rapidly, perhaps even faster than exponentially than the total emission with time at a given f after the burst peaks (Figure 3.18).

The theory of Robinson and Cairns (1998) predicts that the intensity of fundamental emission falls off exponentially with time after the peak due to scattering by density irregularities and losses by linear mode conversion. Our results for exponential decay of the total flux with time are thus qualitatively consistent with the theory of Robinson and Cairns (1998). Similarly, the faster decay of the polarized flux with time than the total flux is expected on qualitative grounds, since reflection of pure o- or x-mode radiation from a sufficiently sharp density increase, produces radiation in both modes (Hayes, 1985a,b), thereby reducing the net polarization. Further extension of theory is required to assess this interpretation quantitatively.

3.8 Decay Time

We now consider the exponential decay time t_d of type III burst intensity as a function of frequency (f). Type III bursts on 2014/09/16, 2015/09/18,

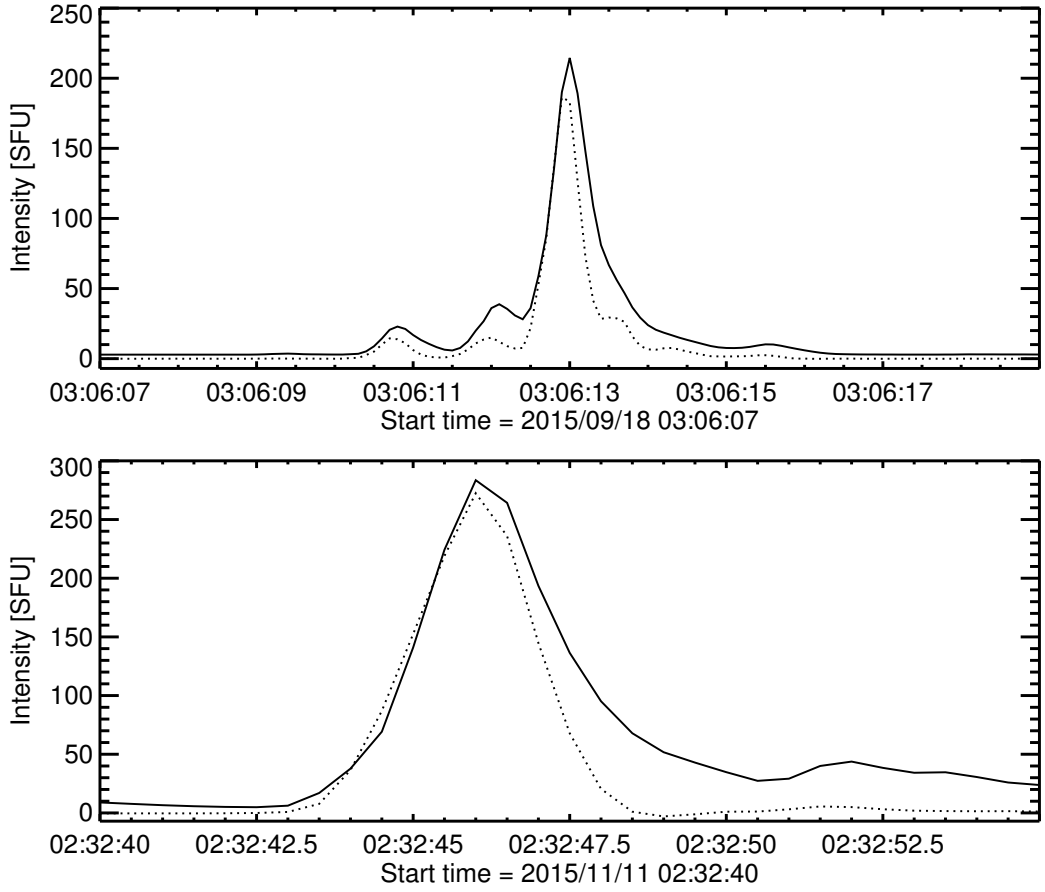

Figure 3.17: Variation with the time of the total intensity (solid curve) and circularly polarized flux (dotted curve) at 80 MHz for the type III bursts on (top) September 18, 2015 and (bottom) November 11, 2015. The scales of the polarized fluxes are enlarged by factors of 5 and 10, respectively.

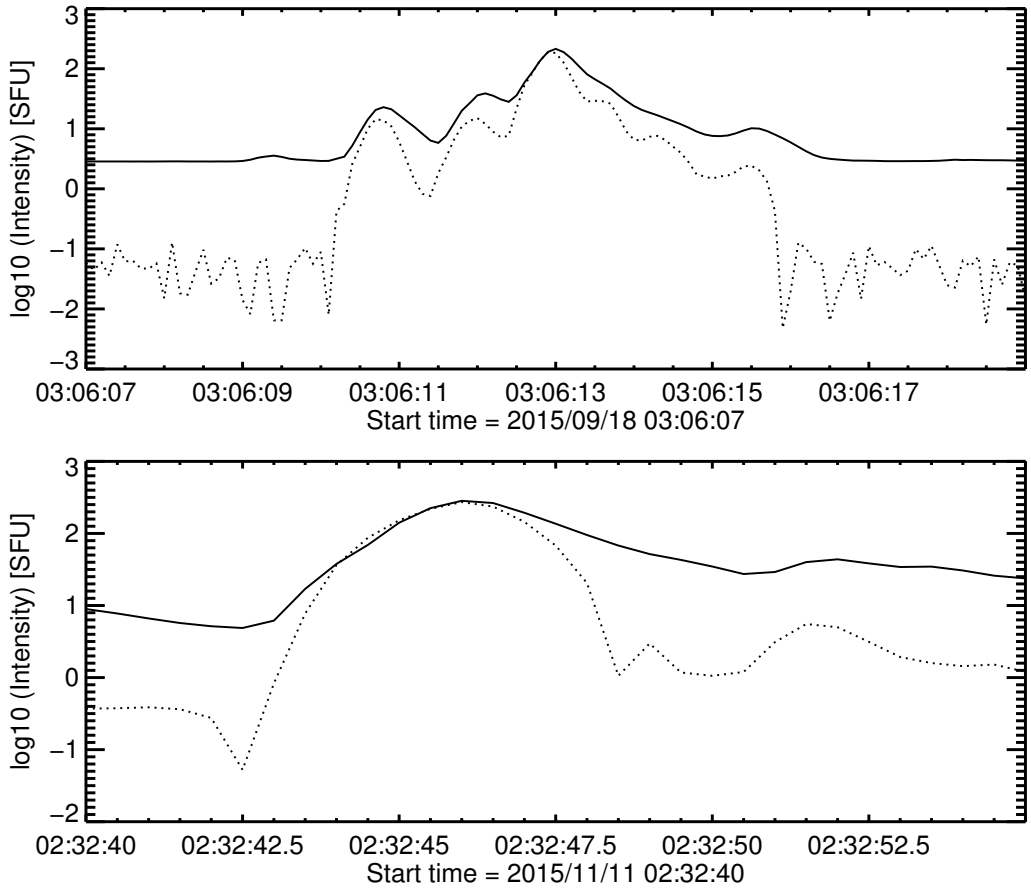

Figure 3.18: As for Figure 3.17, but displayed on a logarithmic scale. The magnitudes of the polarized fluxes are enlarged by factors of 5 and 10, respectively.

and 2015/11/11 are analysed with t_d obtained by fitting $logI(t)$ with a linear function from 80 to 240 MHz (Figure 3.19).

For our three events we find that a least square fit yields $t_d \propto f^{-2.0\pm0.1}$. This frequency dependence is significantly stronger than the dependences $f^{-0.95\pm0.1}$ found observationally by Alvarez and Haddock (1973a), $f^{-1.09\pm0.05}$ obtained theoretically by Evans et al. (1973), and $f^{-1.1\pm0.1}$ by Robinson and Cairns (1998). Note that these dependences were found for data with frequencies 50 kHz−200 MHz, 67 kHz−2.8 MHz, and 25 MHz, respectively. In particular, we find $t_d \approx 0.5 - 4.5$ s whereas the fits of Alvarez and Haddock (1973a), Evans et al. (1973), and Robinson and Cairns (1998) find $t_d \approx 0.5 - 2.5$ s, $\approx 0.15 - 0.5$ s, and $\approx 0.2 - 0.6$ s at the same frequencies, respectively. Our values of t_d are a factor of $\approx$ 3−5 larger than these fits yield. Thus, for our 3 events the values of t_d have a much faster frequency dependence ($\propto f^{-2.0\pm0.1}$ rather than $f^{-0.95\pm0.1}$, $f^{-1.09\pm0.05}$, and $f^{-1.1\pm0.1}$, approximately) than earlier work, although the values of t_d near 240 MHz are very similar in magnitude in our observations and these of Alvarez and Haddock (1973a).

3.9 Discussion

It is well established theoretically that the fundamental emission of type III bursts should be nearly 100% circularly polarized in the o-mode while harmonic emission is predicted to have significantly lower circular polarization fractions (Melrose, 2009). For second harmonic plasma emission, the circular polarization is that of the o-mode and depends theoretically on the distributions of Langmuir waves that participate in the coalescence process $L + L' \rightarrow T$ $(2f_p)$ (Melrose, 1982; Robinson and Cairns, 2000; Melrose, 2009; Cairns, 2011). Here L, L', and T denote Langmuir, scattered Langmuir, and transverse waves, respectively. Assuming the Langmuir waves are essentially parallel to the magnetic field,

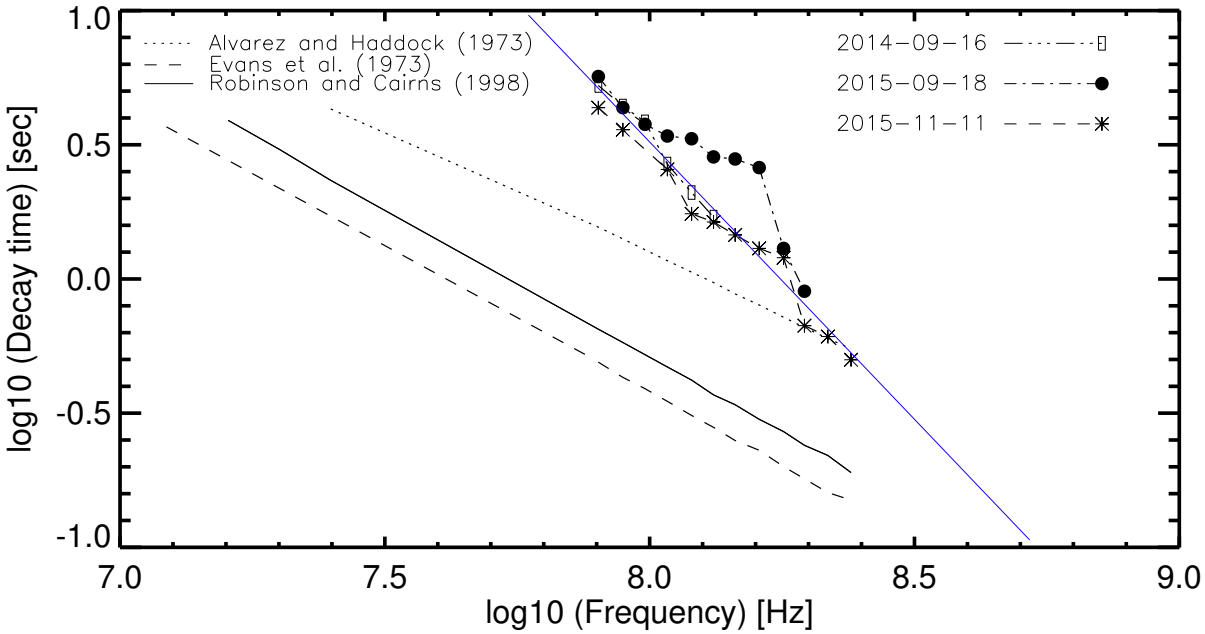

Figure 3.19: Variation of t_d with f for the type III bursts for 2014/09/16 (dashed three-dotted), 2015/09/18 (dashed-dotted), and 2015/11/11 (dashed line) events, respectively, in a log-log plot. The dotted, dashed, and solid lines show the fits of Alvarez and Haddock (1973a), Evans et al. (1973), and Robinson and Cairns (1998), respectively. The blue colored line indicates the fit to our data with $t_d \propto f^{-2.0\pm0.1}$.

the circular polarization is that of the o-mode (Melrose et al., 1980) and the predicted degree of second harmonic polarization r_p is

$$r_p = \frac{11}{48}\frac{f_B}{f_P} \mid cos\theta \mid = \frac{11}{24}\frac{f_B}{f} \mid cos\theta \mid, \tag{3.1}$$

where f_B is the electron gyro frequency, and θ is the angle between the magnetic field $\vec{B}(r)$ and the line of sight.

Equation (3.1) implies 3 things: (1) $r_p << 1$, for $f_B/f_P << 1$ and $r_p \leq 0.25$ for all θ and $f_B/f_P \leq 1$, so weak polarization is expected; (2) $r_p = r_p(\theta)$, so stronger polarization is expected near disk center and depolarization near the limb assuming, $\vec{B}(r) = \vec{B}(r)\hat{r}$; and (3) $r_p = r_p(r)$ since f_B/f_P is function of r. Here r is the radial distance. Since Figures 3.12−3.16 show $r_p >> 10\%$ mostly, both near burst onset and burst maximum, often our data are inconsistent with Equation (3.1). This provides a strong argument that our type III bursts are not primarily H emission, instead primarily being F emission.

We note that r_p is a function of (X,Y) positions of burst source in Figures 3.14−3.16, with weak trends that r_p is larger near disk center and decreases towards the limb, as predicted by Equation (3.1). A similar beaming effect is found for type I bursts (Aschwanden, 1986), which are usually interpreted in terms of F emission. Our results of r_p are thus not consistent with H emission. Instead, we interpret our type III burst emission with higher degree of circular polarization in terms of F plasma emission, even though standard theory predicts 100% circular polarization.

Large values of the circular polarization near burst onset (10−60%) and near burst maximum (10−40%) in Figures 3.6, 3.9−3.12, and 3.14−3.16 suggests that (1) F contribution is large near burst onset, (2) the F contribution is large, not small, near the peak, and (3) perhaps most of our bursts, which do not have distinguishable F and H contributions and so are classifiable as

structureless type IIIs (no F/H structure), are primarily F, not H. Due to the lack of time resolution, just by observing the dynamic spectra as in as Figures 3.1−3.4, we can not identify with certainty that type III burst emission is at F-H structure and so argue at the F or H of the plasma emission. We need better time resolution with polarization measurements to resolve this issue.

Clearly a depolarization effect occurs in type IIIs since always $r_p << 100\%$ in our data and in the previous works of Dulk and Suzuki (1980), Suzuki and Dulk (1985), Melrose (1989b), and Mercier (1990). One interpretation is that this is due to scattering effects as the radio emission propagates outward through the corona (Robinson, 1983). This is one of the most viable reasons for emissions being depolarized as they propagate but can not explain why fully polarized emission is never seen. An interpretation for this is that the emission can be depolarized to some extent within the source region itself due to propagation effect and this is inherent to the emission process (Wentzel, 1984). Another is that beaming effects relative to $\vec{B}(r)$ in the source region are important, as found in the position dependences of r_p(X,Y) in Figures 3.14−3.16, with a corresponding result for r_p(X,Y) for type I bursts, which are almost universally interpreted in terms of F plasma emission.

Another point is that the magnetic field strength is predicted to become weaker with increasing r, with f_B(r) decreasing faster than f_p(r), relative to f_p, and thus we get a smaller r_p at lower frequencies from (2) and Equation (3.1).

It is noted that finding the degree of circular polarization has the same sign for all frequencies of a given burst reveals that type III bursts originate from unipolar magnetic field regions. The electron beams propagate along with a bundle of $\vec{B}$ lines with the same directivity (which reasonably corresponds to reconnected $\vec{B}$ lines above or below the neutral sheet) and so the same sense of circular polarization.

In an inhomogeneous plasma medium, the oppositely polarized electromag-

netic o- and x- modes from magnetoionic theory are coupled to each other in density gradients and energy can be transferred from one mode to the other by reflection and from linearly from Langmuir waves to one mode to another at constant frequency via the Linear Mode Conversion (LMC) process. LMC is one of the fundamental emission processes for free space radiation from plasmas (Kim et al., 2007, 2008), relevant to radiation from the type III radio bursts from the corona. Theory suggests that LMC can produce both the o- and x-modes from Langmuir modes at a given density enhancement (Kim et al., 2007, 2008), thereby producing radiation less than 100% circularly polarized in the sense of the o-mode and so can produce relatively weakly circularly polarized radiation. Thus if LMC is important for F emission then the partial polarization of type IIIs can be explained without depolarization theories (Kim et al., 2007, 2008).

As we move to higher frequencies, the normalized total and circularly polarized intensity profiles are found to become almost identical, more symmetric, smoother, and narrower but the profiles for the polarization fraction are asymmetric when the source moves (Figures 3.9, 3.10, and 3.11). We propose that the burst source motion is responsible for this asymmetry. In particular, the source is most highly polarized in the direction of motion and less polarized in the opposite direction (Stokes $\mid V \mid/I$ images of Figure 3.5). A natural interpretation is that the front of the type III electron beam produces primarily F emission.

We found higher polarization fraction in the leading edge and lower polarization fraction at the tailing edge of the burst source in the direction of motion (Figure 3.5). The emission tail in interplanetary type IIIs comprise F than H radiation (Robinson and Cairns, 1998). We propose two things that 1) F emission will be delayed by a time Δt with respect to that of H emission originating from the same source location, due to its lower group speed, as suggested by Suzuki and Dulk (1985). On the other hand, H emission should

be observed with no delay in observational time interval (Robinson and Cairns, 1994). 2) Scattering lengthens the paths that F emission must travel. Thus F emission at the tailing edge will be the most scattered radiation of burst and thus lower polarization fraction. We assume that F emission is always dominant at the leading edge of our bursts and hence so higher polarization fraction.

On the basis of the imaging results that show higher polarization fraction near burst onset at the front of the source than maximum burst intensity (the Stokes $\mid V \mid/I$ images of Figure 3.6) but more intense and lower polarization emission behind, we consider that F emission is dominant at burst onset thus having higher polarization fraction for burst source. Then near burst maximum the emission continues both F and H components, thus having relatively lower polarization fraction near burst maximum. In the decay phase, the polarization fraction is then found to be smaller than for the burst maximum and to decrease with time. We propose that the decay phase of burst emission is dominated again by the F component, as suggested by Dulk et al. (1984) and Robinson and Cairns (1998), which is released slowly at lower polarization fraction by scattering of previously generated F emission in the source region. Hence, during the decay phase of burst emission, the F radiation will be scattered and depolarized, and so have weaker polarization till the end of burst emission.

One of the three possible alternative ways described by Melrose (1989b) to reduce the polarization of F emission scattering is that a large angle scatter can change polarization significantly; specifically a scatter through angle $\theta \approx 90^{\circ}$ reduces the polarization to ≈ 0. Some observations argue that depolarization mechanism that is happened in burst source region is due to the scattering effect (Wentzel, 1984).

The temporal variations of the polarized flux are faster than the total intensity for the type III bursts in Figures 3.17 and 3.18. This did not happen for all the events in our case. We found that the intensity of type III emission

decreases exponentially with time after the burst peak. In our cases, the polarized flux decreases faster with time than the total intensity, with weak evidence that the decay is faster than exponential. Qualitatively, faster decay of the polarized emission than the total intensity is expected if depolarization effects are occurring, for instance by scattering in the source and along the path.

The exponential decay time t_d of the burst intensity is found to decrease faster with frequency than previous observations find: $t_d \propto f^{-2.0\pm0.1}$ instead of $f^{-0.95\pm0.1}$, $f^{-1.09\pm0.05}$, and $f^{-1.1\pm0.1}$ from the observations of Alvarez and Haddock (1973a), Evans et al. (1973), and the theory of Robinson and Cairns (1998) (Figure 3.19). Moreover, while our analyses yield the same t_d at 240 MHz as Alvarez and Haddock (1973a), the theory of Robinson and Cairns (1998) predicts t_d that are a factor of 2−3 too small. t_d is found to be larger by a factor of 3−5 than those results of Alvarez and Haddock (1973a), Evans et al. (1973), and Robinson and Cairns (1998).

The theory of Robinson and Cairns (1998) balances diffusive transport of radiation with loss by LMC to predict the expression of t_d in the following:

$$t_d = \frac{1}{\lambda_1} \approx \frac{23}{(\pi + 2\phi_n)^2} u_c^{-3/2} \frac{\rho}{c} \left(\frac{\omega_p^2 < l >^2}{c^2} \frac{\Delta N}{N} \right)^{1/6}. \tag{3.2}$$

Here λ_1 is the eigenvalue for the first eigenfunction u_c (value of ≈ 2.63) describing the diffusive transport of the radiation, with $\phi_n \leq 2\pi$ a phase. The quantities $< l >$ and $\Delta N/N$ are the average spatial scale and normalized amplitudes of the density turbulence that scatters the radiation, while ω_p is the angular plasma frequency. All of ω_p, $< l >$, and $\Delta N/N$ are in principle functions of the radial distance $\rho = r - R_s$. The text and Table 1 of Robinson and Cairns (1998) provide more details and representative parameters. The frequency and radial dependence of t_d thus depend primarily on the radial dependences of $\omega_p(\rho) \approx \omega = 2\pi f$, $< l >$, and $\Delta N/N$. Note that if $\omega_p^2(\rho) \propto N(\rho) \propto \rho^{-2}$ and

both $< l >$ and $\Delta N/N$ are independent of ρ then $t_d(\rho) \propto \rho \times (\rho^{-2})^{1/6} \approx \rho^{0.67}$ and $t_d(f) \propto (f^{-1})^{0.67} \approx f^{-0.67}$. The variations $\omega_p^2(\rho) \propto \rho^{-2}$, $< l > \propto \rho^{-1}$, and $\Delta N/N \propto \rho^{-1}$ then yield $t_d(\rho) \propto \rho^{-1.34}$ and $t_d(f) \propto f^{-1.34}$ in our case. This result can be interpreted in terms of changes in the radial dependence of density turbulence with radial distance.

It is noted here that we do not have magnetic field and density data throughout the corona. From Equation (3.1), it would be interesting to compare the degree of circular polarization with the magnetic field and ratio f_B/f_p using some model predictions. As an example, the PFSS model (Schatten et al., 1969) along with the FORWARD software package (Gibson et al., 2016) would be a viable way to extract the magnetic field values at different heights from surface of the corona. This is beyond the scope of this work and will be addressed in future research.

3.10 Conclusions

We observed the degree of circular polarization of sixteen isolated type III solar radio bursts using the MWA at frequencies from 80 to 240 MHz. The degree of circular polarization increased as a function of frequency on average. At both burst onset and maximum intensity, higher polarization fractions were found when the burst source located near the disk center and lower polarization fractions near the limb. The shape of both the total intensity (Stokes I) and circularly polarized flux (Stokes V) profiles for one event without source motion became identical, symmetric, narrower, and smoother as frequency increased. On the other hand, two events with source motion showed asymmetric profiles for the polarization fraction (Stokes $\mid V \mid/I$), with higher polarization in the direction of the burst source motion. We found speeds 0.25 and 0.23 c for the two burst sources in the direction of source motion at 80 MHz. We observed larger

polarization fraction at burst onset and proposed that this was dominated by the F component. The emission was then rolled out by F and H components at burst maximum, hence so lower polarization fraction than onset. After the maximum burst intensity, the primary emission remaining was F emission, which slowly leaked from the source and decayed over time with scattering effects making the emission weaker and increasingly smaller polarization fraction until the end of the burst. This pattern of fundamental, fundamental and harmonic, and then fundamental emission with time was consistent with the interpretations of Dulk et al. (1984), Robinson et al. (1994), and Robinson and Cairns (1998). The observed polarization fractions are always less than 60%, well below the 100% ratio predicted for the typical nonlinear Langmuir wave mechanisms. This lower polarization fraction may be due to depolarization within the source region. The maxima in the polarized flux profiles sometimes preceded the maxima of the total intensity profiles, which was consistent with previous observations. We argue this happened due to the dominance of F emission with o-mode at early times with higher polarization fraction that travels faster and reaches us first. The decay time t_d that we found in this study varied $t_d \propto f^{-2.0\pm0.1}$ with a more rapid frequency dependences compared with previous works of Alvarez and Haddock (1973a), Evans et al. (1973), and Robinson and Cairns (1998), and yielded large values of a factor of 3−5 greater than predicted by Robinson and Cairns (1998). t_d varied with ρ and f such that $t_d(\rho) \propto \rho^{-0.67}$ for $t_d(f) \propto f^{-1}$ and $t_d(\rho) \propto \rho^{-1.34}$ when $t_d(f) \propto f^{-2}$. This result can be interpreted in terms of changes in the radial dependence of density turbulence with radial distance. We conclude that the scattering effect responsible for depolarizing burst emission is a viable reason for getting lower polarization fractions for our observed type IIIs at frequencies from 80 to 240 MHz.

Chapter 4

Observed Sources and Related Properties of Metric Type III Radio Bursts at 80–240 MHz

Abstract

We present low-frequency observations of the intriguing properties of type III solar radio bursts using the *Murchison Widefield Array* (MWA). Specifically, near times of burst maximum intensity we study the burst source sizes, flux densities, and brightness temperatures of 10 type III events in both total (Stokes I) and polarized intensity (Stokes V) images. We find that the source area A increases as the frequency f decreases according to $A \propto f^{-2.4\pm0.4}$ and $A \propto f^{-2.6\pm0.4}$ in Stokes I and V images, respectively, whereas the MWA beam area varies as $f^{-2.5\pm0.2}$. Scattering theory predicts that $A \propto f^{-4}$ inconsistent with the MWA observations. We suggest that the observed area changes as due to divergence of open magnetic field lines, which causes the source sizes to increase at lower frequencies and larger heights. On average, the total and polarized fluxes are found to increase as f decreases. We find total fluxes on average 550 and 50 SFU at 80 and 240 MHz, respectively, whereas logarithmic flux density of type IIIs ranges from 0.2 to 4.8 at 80 MHz (Dulk and Suzuki, 1980). Our flux values lie within the range of their flux values. The brightness temperatures T_b decrease as f increases. We obtain maximum and minimum T_b $4{\times}10^{11}$ and $1.2{\times}10^{8}$ K at 80 and 240 MHz, respectively, which are consistent with previous observations ($\log T_b$: 7−11.5 at 80 MHz) Dulk and Suzuki (1980). We find that T_b does not depend on the source's position, although this result is not definitive since we analyse a small number of events. We argue that divergence of open field lines is a process to explain increasing source size as the frequency decreases.

4.1 Introduction

Type III solar radio bursts are the Sun's most intense and frequent non-thermal radio emissions and are released by semi-relativistic electron beams of speed ≈ 0.2−0.5 c (Dulk et al., 1984; Morosan et al., 2014; McCauley et al., 2017). These electron beams originate in the lower corona during magnetic reconnection events that occur, generally but not always, in solar flares (Cairns et al., 2018). The beams generate Langmuir waves while traveling along open magnetic field lines into the outer corona and interplanetary space.

The first detailed theory of type III bursts was given by Ginzburg and Zhelezniakov (1958) and thereafter has been developed by many authors (Melrose, 1982; Cairns, 1987a,b, 1988; Cairns and Robinson, 1992; Robinson et al., 1993; Li et al., 2005; Cairns, 2011; Graham and Cairns, 2013). The modern concept of the theory is that fundamental emission occurs due to the decay $L \rightarrow T + S$ of beam-driven Langmuir wave into a radio wave and an ion sound wave (where L, S, and T denote Langmuir, ion sound, and transverse waves respectively), stimulated by the electrostatic decay process $L \rightarrow L' + S$ in which beam-driven Langmuir waves decay into a backscattered L' wave and an ion sound S wave. The second harmonic emission is due to the coalescence process $L + L' \rightarrow T$. Each step of the theory has been updated several times as ideas based on underlying plasma theory are established, as reviewed by Robinson and Cairns (2000), Melrose (2009), Cairns (2011), and Reid and Ratcliffe (2014).

Type III bursts have higher frequency drift rate than type I and II bursts. Usually, their drift rates vary from burst to burst. Type IIIs can be observed from kHz frequencies (Dulk et al., 1984; Krupar et al., 2011) up to frequencies of 8 GHz (Ma et al., 2012). Some type IIIs drift from higher starting frequencies near 900 MHz (Benz et al., 2009) while others begin to drift at lower frequencies below 50 MHz (Ganse et al., 2012). *Coronal* type III bursts are those which

have frequencies above about 20 MHz. *Interplanetary* type III bursts originate when the electron beams escape along the open field lines and continue to stimulate the Langmuir waves in the solar wind plasma. They have frequencies from about 10 MHz down to frequencies of 20 kHz and below near 1 AU (Lin et al., 1973; Leblanc et al., 1998).

These type IIIs exhibit fascinating properties such as frequency drift, motion, large source sizes, brightness temperature, polarization, etc. There is an active debate about the origin of many of the observed properties of type III burst sources. Some authors argue that the observed properties of sources are primarily driven by the divergence of the coronal magnetic field, variability of semi-relativistic non-thermal electron beams, and other physical conditions at the burst site (Sheridan et al., 1972; Dulk et al., 1979; Raoult and Pick, 1980; Duncan, 1985) while others argue for the dominance of wave propagation effects such as ducting, scattering, and refraction (Robinson, 1983; Bastian, 1994; Arzner and Magun, 1999).

It is widely believed that divergence of open magnetic field lines plays a significant role in causing the source size to be larger at higher heights and lower frequencies since the electrons are guided by these field lines. Observations of the source size, position, and polarization of type III bursts have been reported and interpreted in terms of the divergence of coronal magnetic field increasing the source sizes at higher heights (Bougeret et al., 1970; Dulk et al., 1979; Dulk and Suzuki, 1980). Recently, McCauley et al. (2017) also reported that divergence of open field lines is responsible for the source sizes increasing with decreasing frequencies. On the other side, large source sizes can be produced by the refraction, reflection, and scattering of radio waves by density gradients and inhomogeneities in the corona (Fokker, 1965; Riddle, 1974; Robinson, 1983).

The source sizes, source fluxes, and brightness temperatures of type III bursts have been reported in the literature for frequencies ranging from 100s of MHz to

a few GHz. Saint-Hilaire et al. (2013) performed a statistical survey of 10,000 type III radio bursts observed over a decade using the *Nançay Radioheliograph* at 150 to 450 MHz and studied source sizes, distributions of source fluxes, and peak brightness temperatures. They observed Full Width at Half Maximum (FWHM) rms source sizes ≈ 15 and ≈ 5.5 arcmin at 150.9 and 432 MHz, respectively. The flux distributions followed a power-law with an index ≈ −1.7. They also found that the distribution of burst brightness temperatures T_b varied as a power-law with index ≈ −1.8 for all six frequencies. Interestingly, the power-law index of the flux distribution for type III bursts in the GHz range is ≈ −1.8 (Nita et al., 2002), almost identical to that found by Saint-Hilaire et al. (2013).

Observations by the *Culgoora Radioheliograph* at 43, 80, and 160 MHz yield source sizes (full width at 1/e brightness of the equivalent Gaussian source) of 20, 11, and 6 arcmin, respectively, confirming that the source size increases as the frequency decreases (Dulk and Suzuki, 1980). Bougeret et al. (1970) reported source sizes ≈ 5.5 arcmin at 169 MHz and Dulk et al. (1979) observed source sizes ≈ 5.4 arcmin at that same frequency. Recently, Mohan et al. (2019) studied second-scale quasi-periodic oscillations in source size at 111.1 MHz using the *Murchison Widefield Array* (MWA) and found on average source size of 10.6 arcmin. In comparison, the sources of interplanetary type IIIs are roughly 1 AU in size at ≈ 20 kHz (Lin et al., 1973; Lin, 1974). Therefore, it is evident from the above-mentioned observations that source size increases as frequency decreases.

The source sizes, source fluxes, and brightness temperatures of multiple type III bursts have not been observed with the MWA across the whole frequency range from 80 to 240 MHz. In this Chapter we present these observations organised as follows. Relevant MWA characteristics and data reduction processes are presented in Section 4.2. The observed MWA beam and burst source areas are presented in Section 4.3. The evolution of source area with time is described

in Section 4.4. Source fluxes and brightness temperatures are given in Sections 4.5 and 4.6, respectively. Section 4.7 is reserved for interpretation and discussion. Finally, the conclusions of the study are presented in Section 4.8.

4.2 MWA Radio Observations and Data Reduction

The MWA is a low-frequency interferometer in Western Australia (Lonsdale et al., 2009; Tingay et al., 2013a). Technical details of MWA and its overall design are described by Tingay et al. (2013a). The MWA science targets are reported by Bowman et al. (2013). The radio instrument is composed of 128 "tiles" each containing 16 dual-polarization dipole antennas. The total bandwidth is 30.72 MHz, which can be distributed across the range 80 to 300 MHz (Tingay et al., 2013a). Significant amounts of solar research have been done by many authors using MWA observations (Tingay et al., 2013b; Oberoi et al., 2014, 2017; Mohan and Oberoi, 2017; Suresh et al., 2017; McCauley et al., 2017, 2018; Cairns et al., 2018; McCauley et al., 2019; Mohan et al., 2019).

For our events the MWA is observing in the "picket fence" mode, meaning in 12 coarse channels of bandwidth 2.56 MHz whose centre frequencies range from 80 to 240 MHz. The MWA data are recorded in fine-frequency channels with 0.5 s time and 40 kHz frequency resolution, which we average across the 2.56 MHz bandwidths to produce 0.5 s images at 80, 89, 98, 108, 120, 132, 145, 161, 179, 196, 217, and 240 MHz. We used WSClean (w-stacking clean) (Offringa et al., 2014) for imaging, with a Briggs -2 (Briggs, 1995) weighting scheme in order to emphasize spatial resolution.

The type III burst data that we analyze are part of an imaging survey of many type IIIs observed by the MWA during 45 separate observing periods

in 2014 and 2015 (McCauley et al., 2018). We chose burst events occurring between August 2014 to November 2015 due to the existence of processed data and a catalog produced by McCauley et al. (2019). They focused on non-burst spectro-polarimetric observations of the solar corona and studied circular polarization of low-latitude coronal holes at frequencies 80 to 240 MHz using MWA. We, therefore, selected ten sufficiently distinct and locally isolated sets of type III burst events for detailed analysis. The data were flux calibrated using the same manner described by McCauley et al. (2017, 2018).

It is noted here we have chosen events to whose bursts are sufficiently distinguishable from other bursts near the time of peak burst intensity. Table 4.1 shows the date, onset burst time, duration, source position, and source motion of our bursts chosen for analysis.

4.3 MWA Beam and Burst Source Sizes

The burst sources are well fitted with a two-dimensional (2D) elliptical Gaussian model. The fit has parameters, including the semi-major axis a, semi-minor axis b, and the angle θ represents the rotation of the ellipse from the x axis. Consider first these fits to images of the total intensity (Stokes I) of type III burst sources near the peak burst intensity at frequencies ranging from 80 to 240 MHz. Figure 4.1 shows the Full Width at Half Maximum (FWHM) areas on top of the burst sources near times of peak burst intensity on November 11, 2015, at the frequencies 80, 108, 120, 132, 145, 161, 179, and 196 MHz, respectively. Clearly the fits work well. Note that the FWHM areas equal $\pi \times a \times b$, where a and b are the 2D elliptical Gaussian FWHM fit parameters. These fit parameters also work well for the images of Stokes V (not shown here).

Table 4.1

Type III bursts chart			
Date, Symbol	Start time (UT), Duration (s)	Position	Motion
2014/08/26, ◇	03:49:21.20, 5	East limb	Yes, outward
2014/09/15(a), ▫	03:34:18.70, 5	West limb	Yes, outward
2014/09/15(b), △	06:25:58.20, 4	Large radial height	No
2014/09/26, ▽	06:27:10.10, 3	Disk center	No
2014/10/14, ●	03:05:18.70, 3	Large radial height	No
2015/08/25, ■	03:14:58.70, 6	Disk center	No
2015/09/03(a), ◁	01:55:02.70, 5	Disk/East limb	No
2015/09/03(b), ◆	02:10:37.20, 4	Partial on disk	Yes, limited motion
2015/09/18, ∗	03:06:08.20, 6	Disk/West limb	Yes, outward
2015/11/11, +	02:32:40.20, 6	Disk center	No

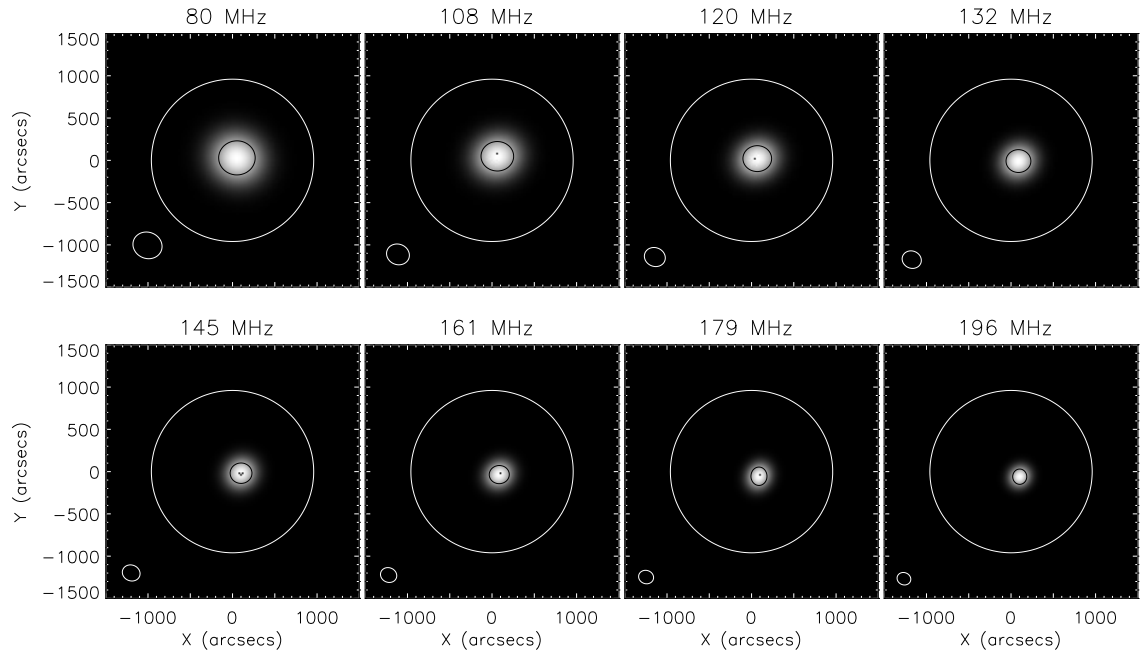

Figure 4.1: FWHM source area (black colored ellipses) superposed on Stokes I images of a type III burst source at different frequencies on November 11, 2015. The solid circles (white color) indicate the optical disk and the ellipses at the lower left corners indicate the MWA synthesized beam sizes.

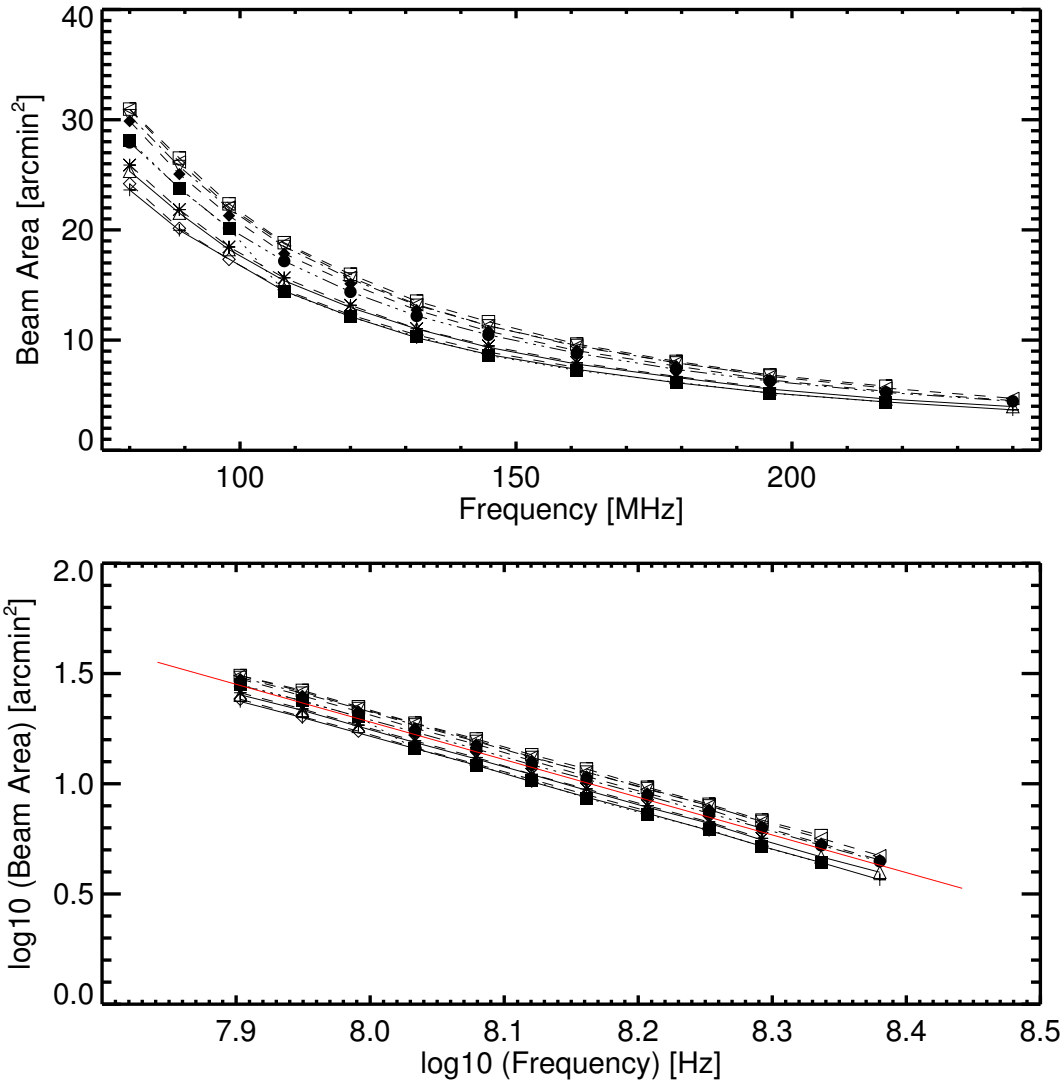

Figure 4.2: (Top) MWA beam area at frequencies from 80 to 240 MHz for 10 events between August 2014 and November 2015. (Bottom) Same plots but on a logarithmic scale. A linear fit in log-log space (red colored line) yields a power-law fit with index $\approx -2.5 \pm 0.2$.

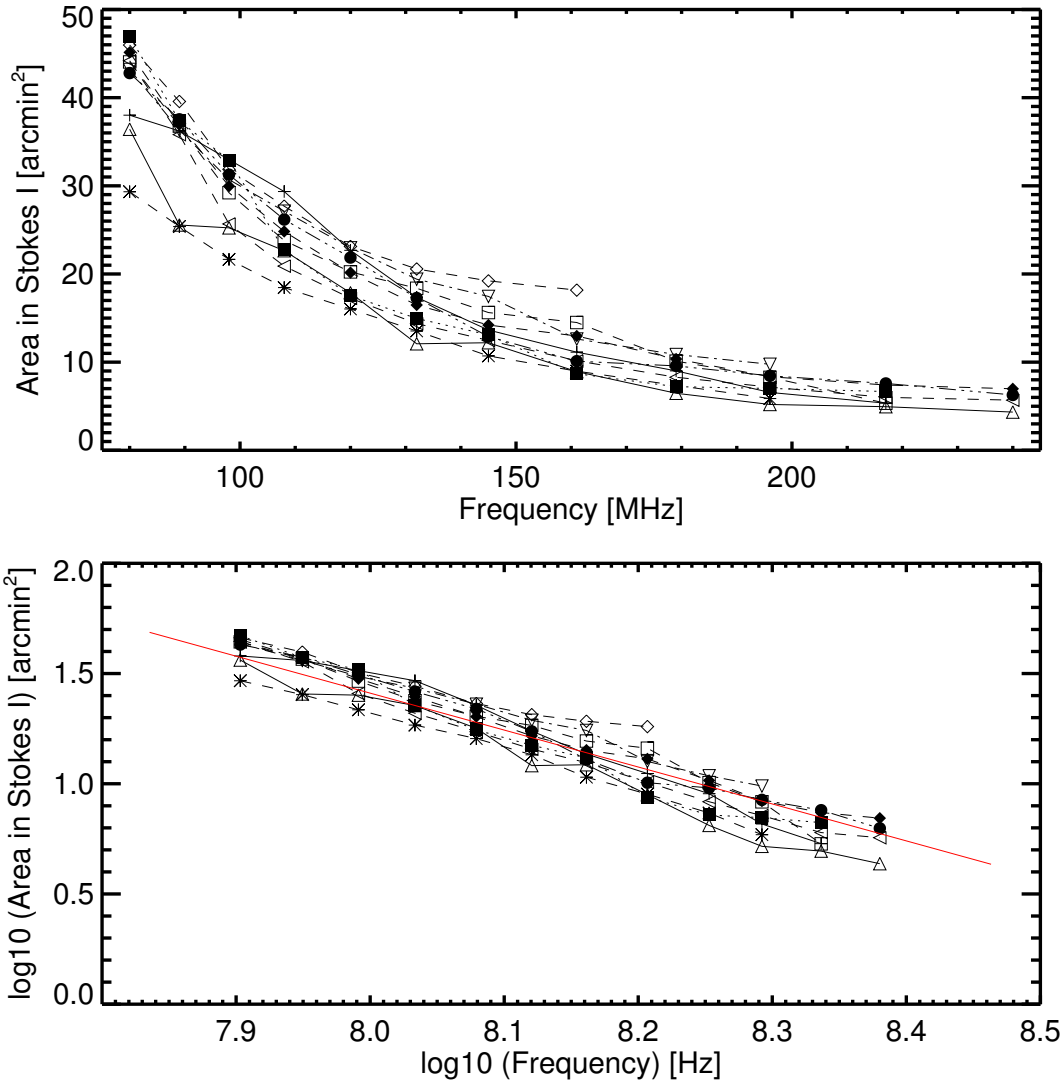

Figure 4.3: (Top) FWHM source areas at frequencies from 80 to 240 MHz for 10 type III burst events between August 2014 and November 2015. (Bottom) Same plots but drawn on a logarithmic scale. A linear fit in log-log space (red colored line) yields a power-law fit with index $\approx -2.4 \pm 0.4$.

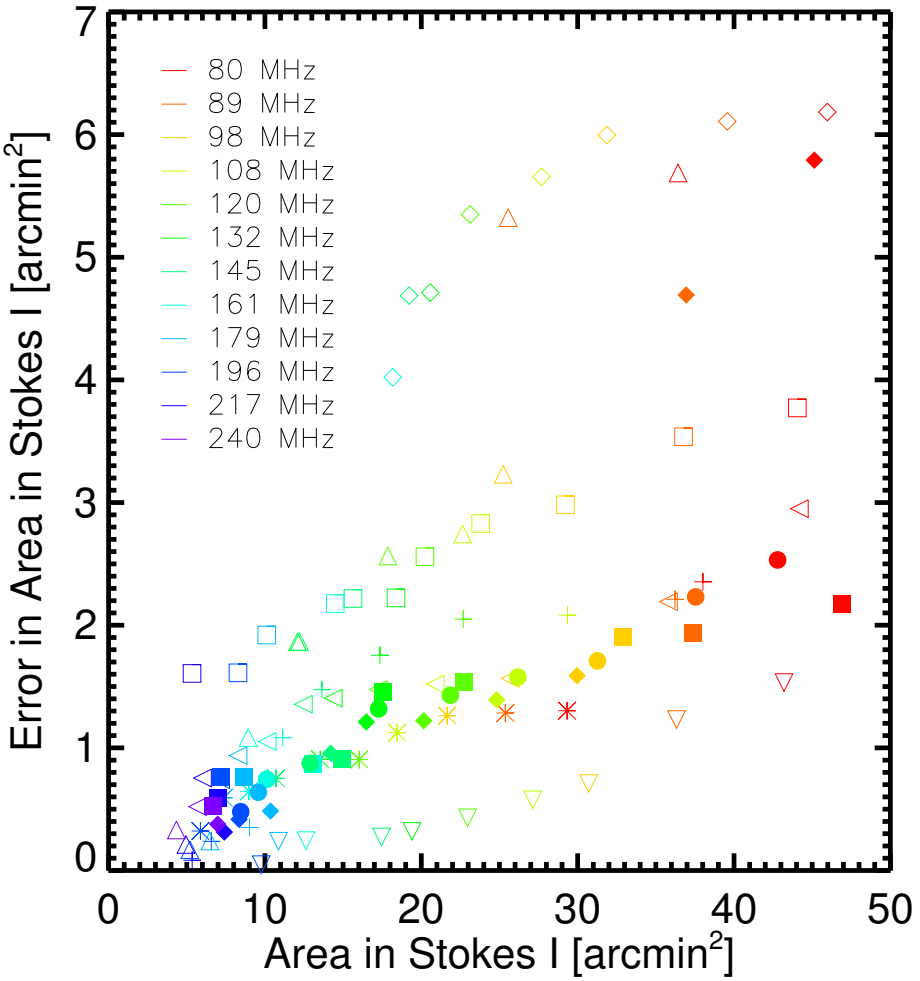

Figure 4.4: Area in Stokes I against the estimated uncertainty in its estimate for observations across all the events as identified in Table 4.1.

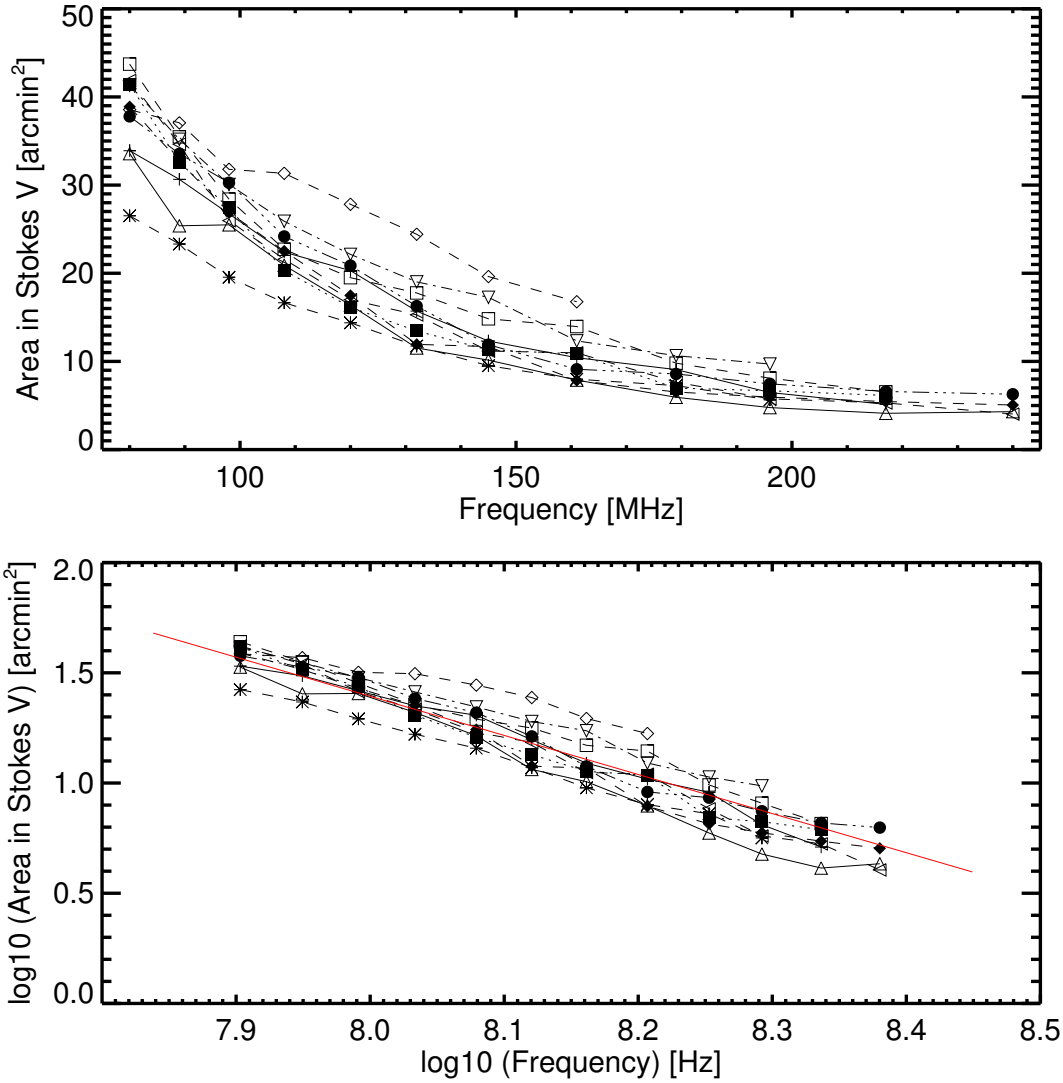

Figure 4.5: Same as Figure 4.3 but using the polarized intensity (Stokes V) images. A linear fit in log-log space (red colored line) yields a power-law fit with index $\approx -2.6 \pm 0.4$.

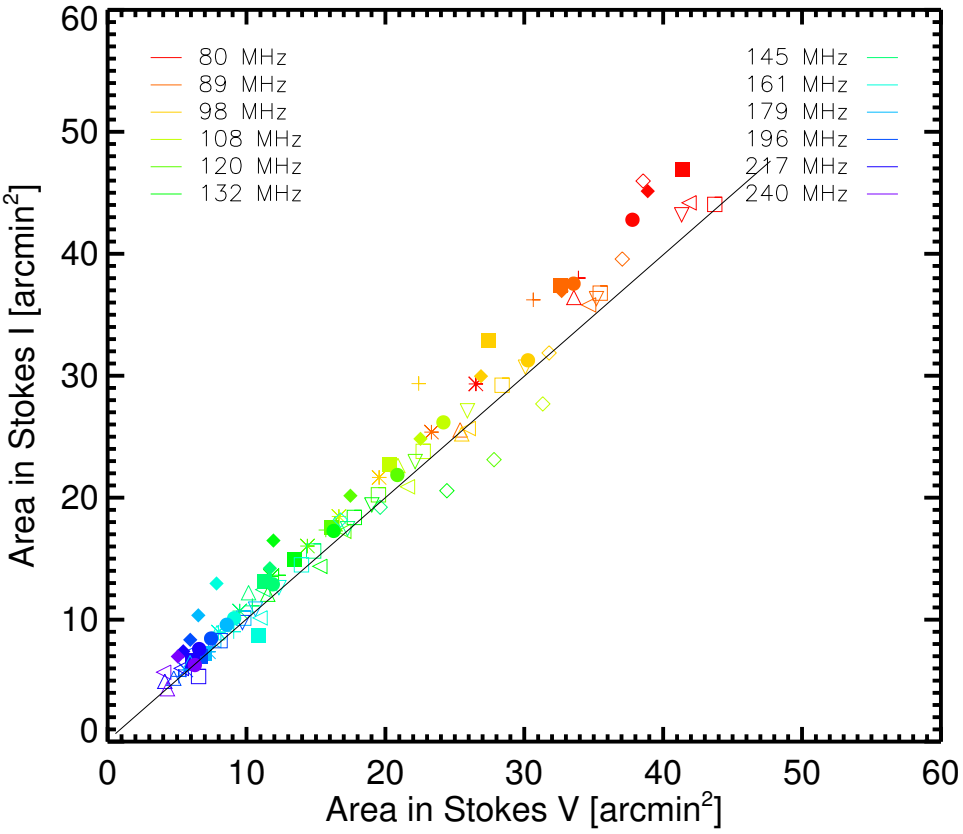

Figure 4.6: Variations of FWHM source area of total intensity (Stokes I) and polarized intensity (Stokes V) images at 12 frequencies. Different symbols indicate different events as identified in Table 4.1. The solid line indicates a straight line that has a slope equal to 1.

The MWA has 16×2 dipole antennas in each tile (aperture array) which receive radio frequency signals. These signals are wired to the analog beam-former using a 50-ohm cable. The analog beam-former forms X- and Y-polarized tile beams as an output by summing each polarization from each antenna. The beam shape can change with pointing direction and frequency.

We now measure MWA beam areas using Stokes I images in the same method as mentioned earlier for measuring source areas. The beam area is then πab in general. Figure 4.2 (top panel) shows the beam areas for ten events

that we chose for analysis of the source areas, source fluxes, and brightness temperatures. The beam is found to have different sizes for each event. We find that the beam size decreases as frequency increases. In log-log space the beam size varies in a closely linear fashion with increasing frequency (Figure 4.2, bottom panel). This corresponds to a power-law dependence with an index -2.5 ± 0.2. It is noted here that the beam areas in the polarized intensity (Stokes V) images are almost identical to those shown in Figure 4.2. That's why we only present the measurements of beam areas using Stokes I.

Figure 4.3 plots the FWHM source areas of bursts using the Stokes I images at frequencies from 80 to 240 MHz for all 10 events. We find that the area $A(f)$ decreases gradually with increasing frequency f for all events. The average source area observed is $\approx$ 40 arcmin^2 at 80 MHz and 7 arcmin^2 at 240 MHz. Importantly, the bottom panel of Figure 4.3 shows a clear power-law dependence, with $A(f) \propto f^{-2.4\pm0.4}$. The estimated uncertainty in area is shown in Figure 4.4. This error estimation has been made using 1 σ standard deviation of observed areas measured at 0.5 s before, during, and 0.5 s after the time of peak burst intensity for each frequency and event. We find relatively large uncertainty for larger area at lower frequency and vice versa. However, Figure 4.5 shows the FWHM source areas of bursts using the Stokes V images. We also find that the area decreases gradually with increasing frequency for all events. The average source area observed is $\approx$ 37 arcmin^2 at 80 MHz and 6 arcmin^2 at 240 MHz. Moreover, the bottom panel of Figure 4.5 shows a power-law dependence, with $A(f) \propto f^{-2.6\pm0.4}$. The uncertainty estimations in observed areas for Stokes V are found relatively similar to those for Stokes I (not shown here). However, for all the events, we find that the average FWHM area in Stokes I is greater than that of Stokes V by almost $2-4$ arcmin^2 at 80 MHz and $1-2$ arcmin^2 at 240 MHz.

Figure 4.6 compares the source areas in total intensity (Stokes I) and

polarized intensity (Stokes V) images at each frequency. Clearly the area in Stokes I is almost always larger than the area in Stokes V, but not by a significant factor. It is noted that both the total and polarized source areas are larger at lower frequencies.

Our results show that the FWHM source area increases as the frequency decreases (Figure 4.3). For comparison, the average values of FWHM source areas are 38 arcmin^2 at 80 MHz, 23 arcmin^2 at 120 MHz, 12 arcmin^2 at 161 MHz, and 6 arcmin^2 at 240 MHz. Using the *Culgoora Radioheliograph*, Dulk and Suzuki (1980) found source sizes 20, 11, and 6 arcmin (full width at 1/e brightness of the equivalent Gaussian source) at 43, 80, and 160 MHz, respectively. Bougeret et al. (1970) and Dulk et al. (1979) reported source sizes ≈ 5.5 arcmin at 169 MHz. Recently, Mohan et al. (2019) reported type III burst source sizes ≈ 10.6 acrmin near 111.1 MHz and 9 arcmin near 119.8 MHz using the MWA. Source sizes between 2 and 7 arcmin at frequencies 169 and 327 MHz are reported for the *Nançay Radioheliograph* (Zlobec et al., 1992; Mercier et al., 2006; Saint-Hilaire et al., 2013). Our measured source areas are thus consistent with those at 80 MHz reported by Dulk and Suzuki (1980), but a factor of one larger than that near 120 MHz observed by Mohan et al. (2019). At higher frequencies (> 161 to 240 MHz), the observed areas are almost similar to those reported for *Nançay Radioheliograph* (Zlobec et al., 1992; Mercier et al., 2006).

It is noted that Dulk and Suzuki (1980) find that the burst sources for fundamental emission is larger than that for harmonic emission, while Melrose (1989) suggests that the true source size is smaller than the observed source between 3.5 (harmonic) and 1.7 (fundamental). We cannot directly identify fundamental and harmonic structure in the dynamic spectra for these type IIIs (Chapter 3). However, the polarization data in Chapter 3 suggest there is substantial fundamental emission for all our events near burst maximum, so we expect relatively large source sizes for our events.

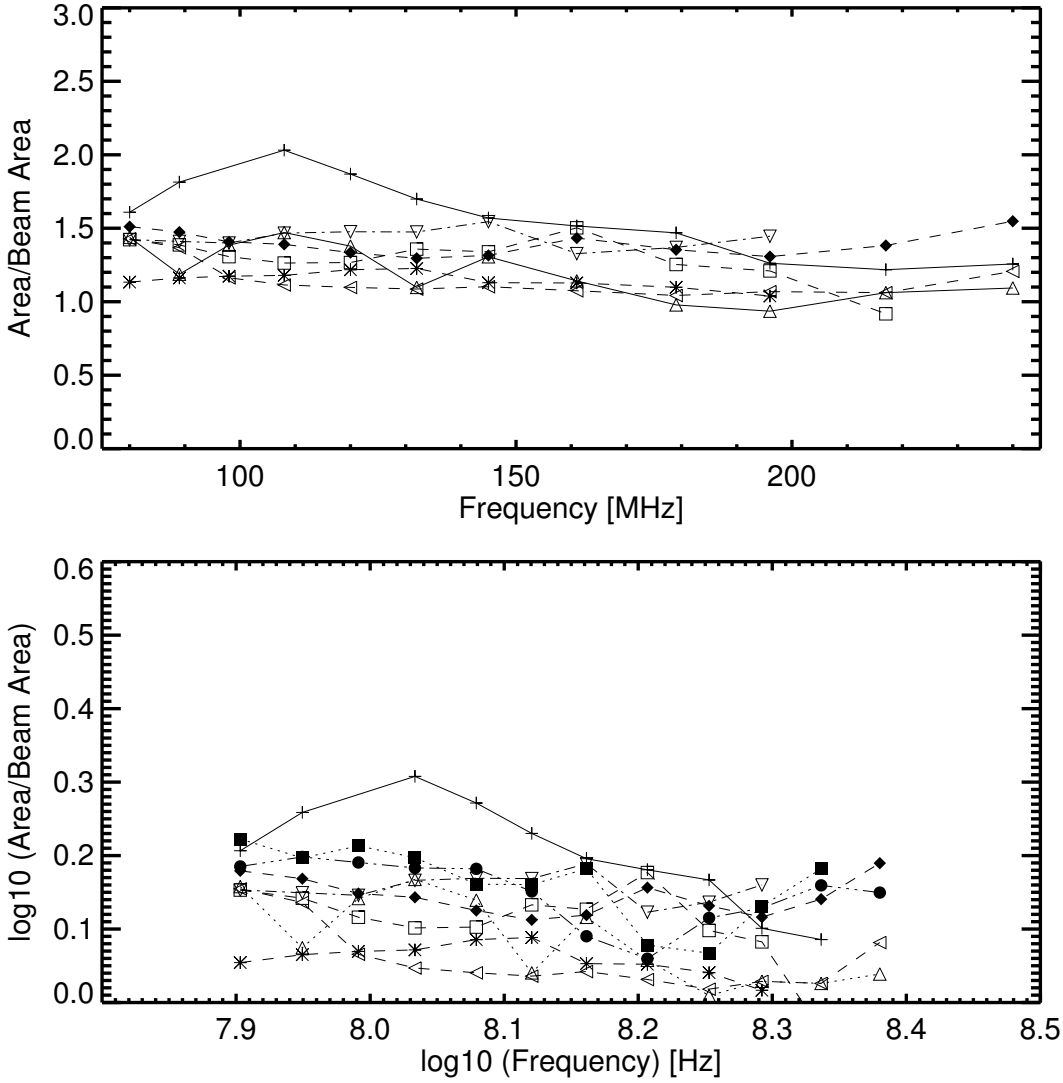

Figure 4.7: (Top) FWHM source area (in Stokes I) over beam area at frequencies range from 80 to 240 MHz for 10 events occurred between August 2014 and November 2015. (Bottom) Same plots but depicted in a logarithmic scale.

In order to understand how the source images (in Stokes I) differ from the beam, Figure 4.7 (top panel) shows the total intensity source areas divided by the beam areas at 12 frequencies for all 10 events. Clearly the ratio of source area to beam area does not change significantly with frequency. On average,

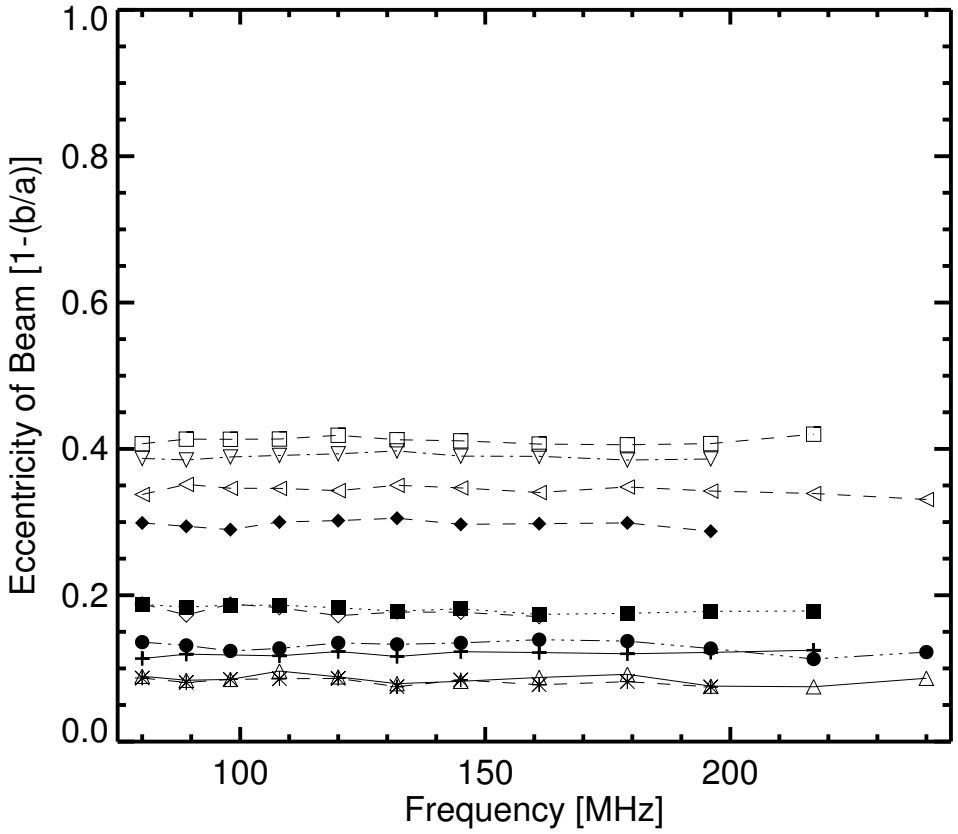

Figure 4.8: Eccentricity of the beam area at frequencies ranging from 80 to 240 MHz.

the source area is larger than the beam area by factors of 1.5 and 1.2 at 80 and 240 MHz, respectively.

We now measure the eccentricity of the beam as shown in Figure 4.8. We find that the beam eccentricity does not change as f increases, being independent of f for all 10 events. Next, we evaluate the eccentricity of the Stokes I sources, as shown in Figure 4.9. It appears that the source eccentricity is almost independent of f for most events. However, for some events the sources are more elliptical at lower frequencies, with relatively higher values of eccentricity. Comparing Figures 4.8 and 4.9 the values of the beam and source eccentricities

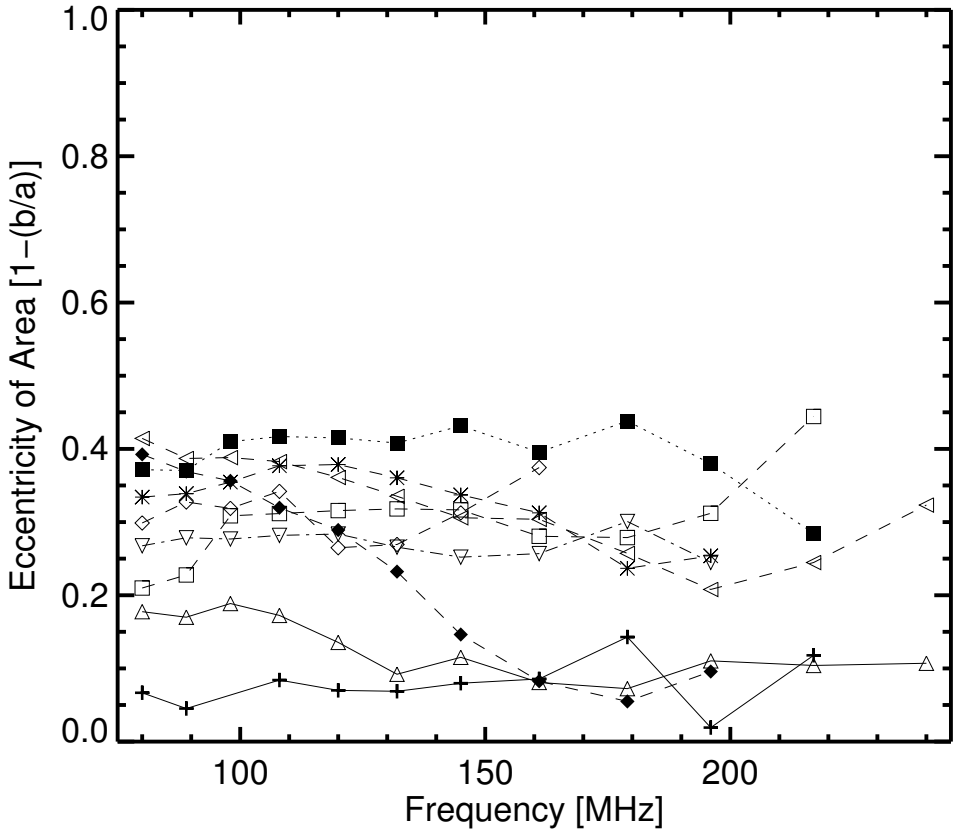

Figure 4.9: Eccentricity of the source area (in Stokes I) at frequencies ranging from 80 to 240 MHz.

are similar in magnitude. However, for each specific event the beam and source eccentricities are typically very different, often differing by a factor of 2. Thus, while the imaged source and beam areas and eccentricities are very similar in magnitude and have very similar variations in frequency and ratios for a given event their detailed magnitudes are not identified and their ratios differ from event to event. These differences are evidence against the beam strongly determining the imaged source characteristics despite the overall similarities. This suggests that the imaged source areas are strongly determined by the interferometric beam areas. Indeed, WSClean should remove beam effects from

the final images.

4.4 Evolution of Source Area with Time

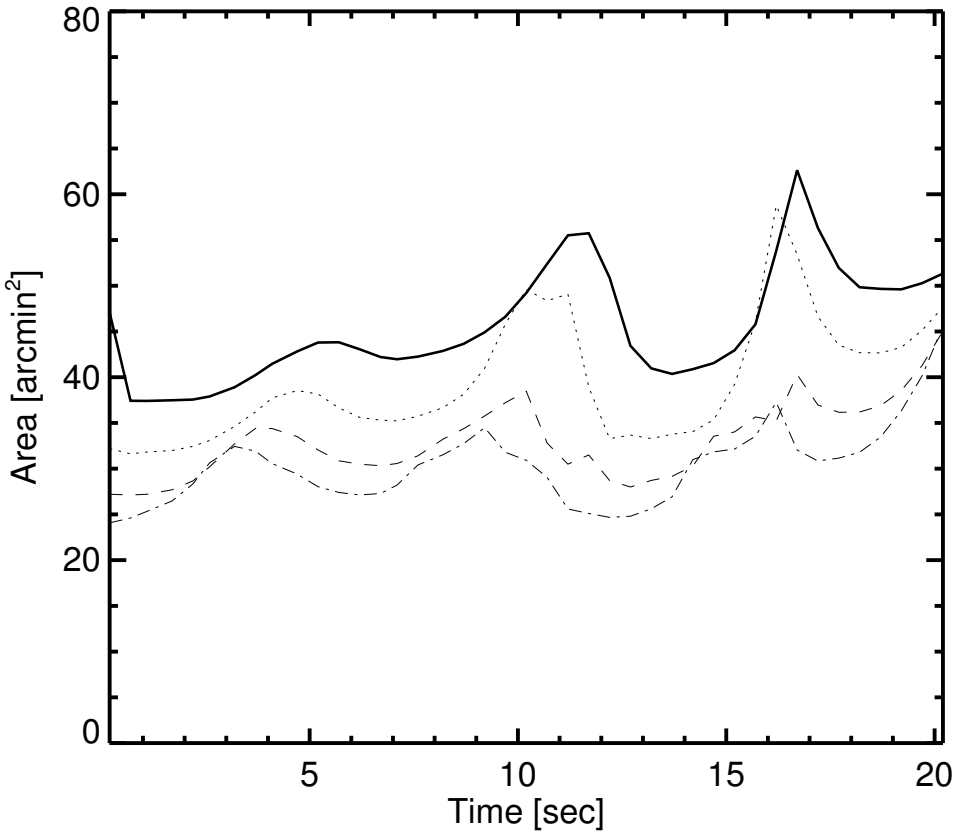

Figure 4.10: Variations of FWHM source areas (in Stokes I) with time periods for multiple type III bursts starting near 05:52:30 UT on 2015/08/25, at different frequencies, respectively, 80 MHz (solid line), 89 MHz (dotted line), 98 MHz (dashed line), and 108 MHz (dashed-dot line).

We now study temporal evolution of source area $A(t)$ (in Stokes I) for multiple type III bursts at different frequencies for the events between 05:52:30 UT and 05:52:50 UT on 2015/08/25. Figure 4.10 plots $A(t)$ at 80, 89, 98, and 108 MHz, respectively. We find that $A(t)$ peaks roughly every 5−6 s, lagging

increasingly at lower f and with qualitatively similar behaviour at each f. We add that $A(t)$ increases as t increases and f decreases.

Using data from the MWA, Mohan et al. (2019) reported $A(t)$ for two groups of weak type III bursts in a 17 s time period at 111, 119, and 126 MHz. They found that $A(t)$ increases as f decreases and observed a tendency for $A(t)$ to increase with t up to first 5 s. After that, the areas tend to oscillate with a mean value in a quasi-periodic manner. This mean value ranged from 20 to 25 arcmin^2. In our case, the area shows an oscillatory trend like that observed by Mohan et al. (2019). Indeed, our observed area does show peaks at roughly 5.5 s time interval although those peaks do not show at same time for all frequencies.

4.5 Source Flux

We now address the maximum intensity of burst sources in solar flux units (SFU, with 1 SFU = 10^{-22} W m^{-2} Hz^{-1}) at frequencies from 80 to 240 MHz. We note that the burst source is sufficiently bright enough to be distinguished from the surrounding quiescent corona when the burst intensity exceeds the background level by at least a several order of magnitude. The procedure is as follows. First, the background levels for each frequency are estimated by taking the median intensity. Second, the burst images are background subtracted for the whole time period. Third, the intensity for the burst source is measured then by summing the background-subtracted flux over the burst source at each time step (0.5 s interval). It is noted here that the burst source is identified as when the total intensity of burst image is 105% greater than the background intensity.

Figure 4.11 plots the total intensity of each of the ten events as a function of frequency. We find that the intensity decreases as the frequency increases for both most events and the sample-averaged intensity spectrum. On average, the

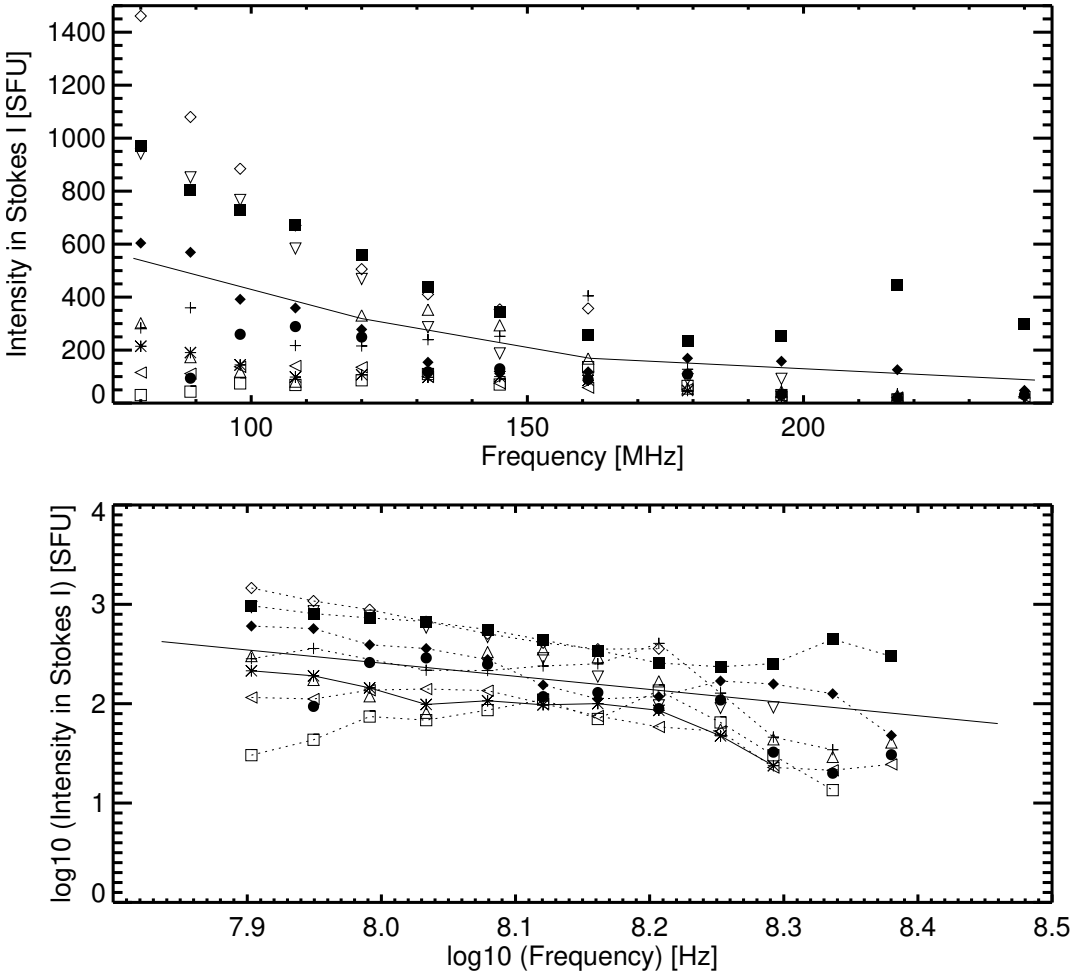

Figure 4.11: (Top) Total fluxes at frequencies from 80 to 240 MHz for the 10 events, at the times of maximum burst intensity. Different symbols indicate different events. The solid line represents the variation of the average intensity with frequency. (Bottom) Same as top panel but on a logarithmic scale. The solid line represents a linear fit to the average values of logarithmic intensity.

intensity is ≈ 550 SFU at 80 MHz and ≈ 50 SFU at 240 MHz. The logarithmic intensity also gradually decreases as we move to higher frequencies as shown in Figure 4.11 (bottom panel). On the other side, Figure 4.12 shows the polarized intensity of the ten events. We also find that the intensity decreases as the frequency increases for both most events and the sample-averaged intensity

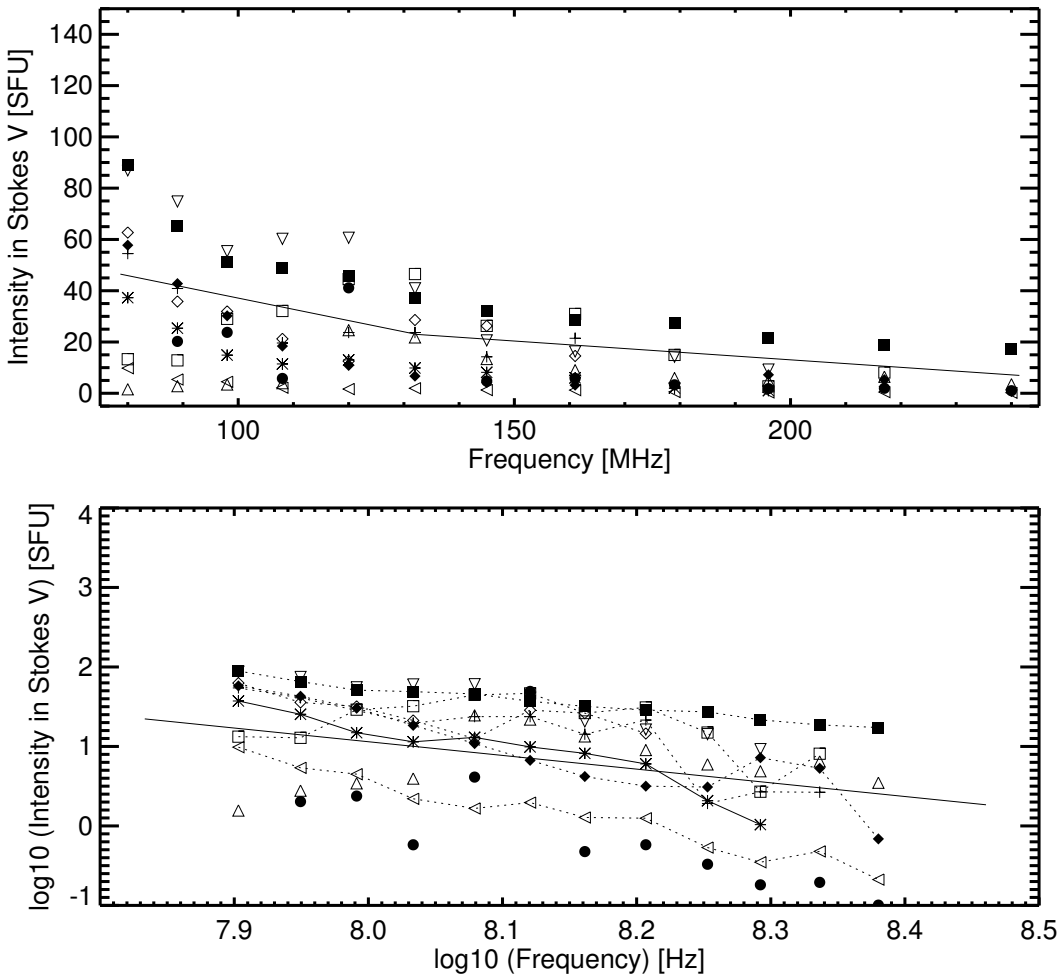

Figure 4.12: Polarized fluxes using the Stokes V (polarized intensity) images. Annotations are same as Figure 4.11.

spectrum. On average, the intensity is ≈ 50 SFU at 80 MHz and ≈ 20 SFU at 240 MHz. The logarithmic intensity also gradually decreases as we move to higher frequencies as shown in Figure 4.12 (bottom panel).

Using the *Culgoora Radioheliograph*, Dulk and Suzuki (1980) reported logarithmic flux densities of type III bursts range from 0.2 to 4.8 SFU at 80 MHz. Recently, Mohan et al. (2019) reported on average flux density 300 SFU at 126 MHz using data from the MWA. In our case, we find average log-intensities 2.5

SFU at 80 MHz and 1.75 SFU at 240 MHz for Stokes *I*. This implies that at 80 MHz, our total flux intensity lies in the range flux values of Dulk and Suzuki (1980) though we analysed a small number of burst events. We add that our flux result is consistent with that of Mohan et al. (2019) at lower frequencies where we found total intensities on average ≈ 550 SFU at 80 MHz, ≈ 350 SFU at 120 MHz, and ≈ 50 SFU at 240 MHz.

4.6 Brightness Temperature

In order to measure the source-averaged brightness temperature T_b of a source, we utilize the measured area and flux intensity of the burst sources using the standard expression (Cairns, 1986):

$$T_b = \frac{V_\phi^2}{2k_B f^2} \frac{F(f)}{\Delta\Omega}, \tag{4.1}$$

where V_ϕ is the phase speed of the radio waves at the observer at frequency f, k_B is Boltzmann's constant, and $F(f)$ is the frequency dependent flux density. The source solid angle $\Delta\Omega = A/4\pi r^2$ where A is the burst source area seen by the observer, and r = 1 AU is the distance from burst source to the observer. It is noted here that the phase speed is equivalent to the speed of light when $f >> f_p$, where f_p is the plasma frequency.

Figure 4.13 (top panel) shows $T_b(f)$ calculated using Equation (4.1) and the areas and fluxes from the Stokes I images near the time of maximum burst intensity. We find that on average T_b decreases as f increases. A linear fit yields $T_b \propto f^{-4.2}$. The maximum and minimum values of T_b are $4{\times}10^{11}$ K at 80 MHz and $1.2{\times}10^{8}$ K at 240 MHz, respectively. For a couple of events, $T_b(f)$ peaks at intermediate frequencies, not at 80 MHz, and then decreases with decreasing f. This is reminiscent of the event of Dulk and Suzuki (1980). Figure 4.13 (bottom panel) shows $T_b(f)$ for the polarized emission V. Now T_b always decreases with

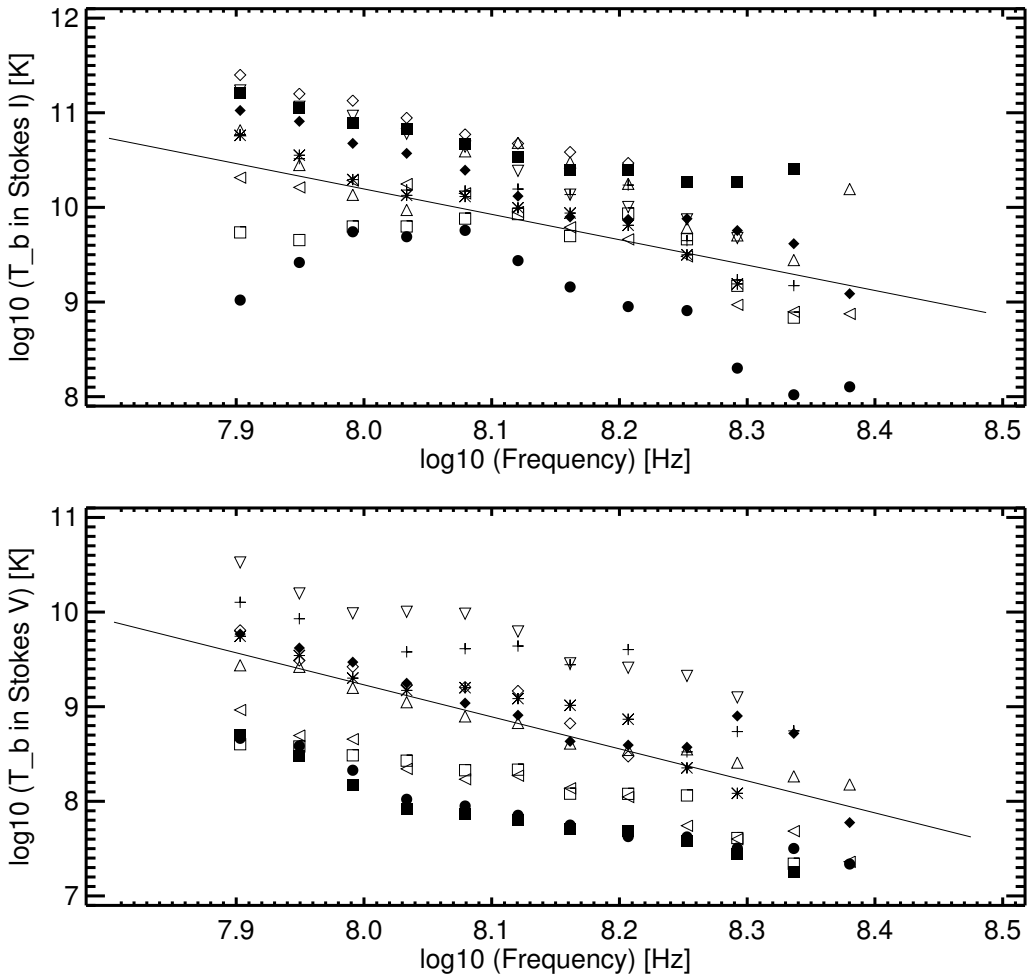

Figure 4.13: Variations of T_b with f using the fluxes and areas for (top) Stokes I and (bottom) V. Solid lines show the corresponding power-law fits $T_b \propto f^{-4.2}$ and $T_b \propto f^{-5.2}$, respectively.

increasing f. A linear fit yields $T_b \propto f^{-5.2}$. We now obtain maximum and minimum values of $T_b \approx 6{\times}10^{10}$ K at 80 MHz and $2.5{\times}10^{7}$ K at 240 MHz, respectively. We see that the values of T_b in Stokes I are greater by about one order of magnitude than those values of T_b in Stokes V.

The values of T_b for our type III burst sources range from a minimum of 1.2×10^{8} K at 240 MHz to a maximum of 4×10^{11} K at 80 MHz (Figure 4.13).

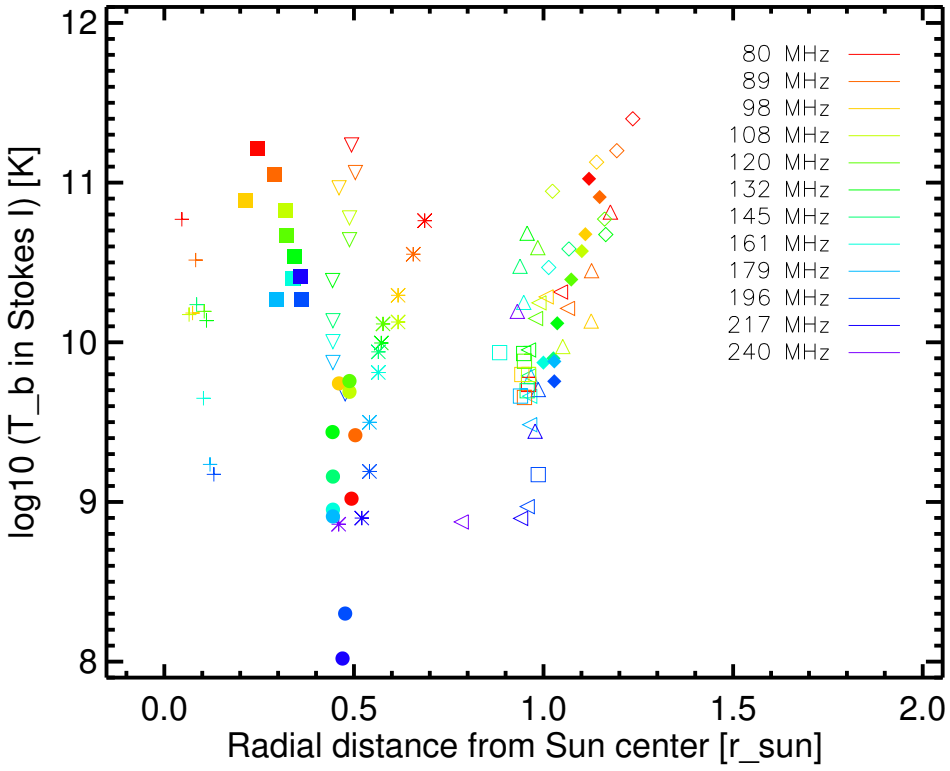

Figure 4.14: Variations of $T_b(f)$ with radial distance from the Sun's center. Different symbols indicate different events as identified in Table 4.1.

These results are consistent with those of Dulk and Suzuki (1980), who found T_b minimum 2 $\times 10^7$ K and maximum 4 $\times 10^{11}$ K at 80 MHz. The brightness temperature at 80 MHz is three orders of magnitude higher than that at 240 MHz in our case. For comparison, Bougeret et al. (1970) reported a maximum value of $T_b \approx 1.5 \times 10^8$ K at 169 MHz whereas we found 2 $\times 10^9$ K at 161 MHz. Value of $T_b \approx 10^8$ K at 118 MHz for weak type III bursts has recently been reported by Mohan et al. (2019). At 1 MHz, the average and maximum values of T_b are 10^{12} and 10^{15} K (Evans et al., 1971). The higher values of the brightness temperature at lower frequencies found by these authors are

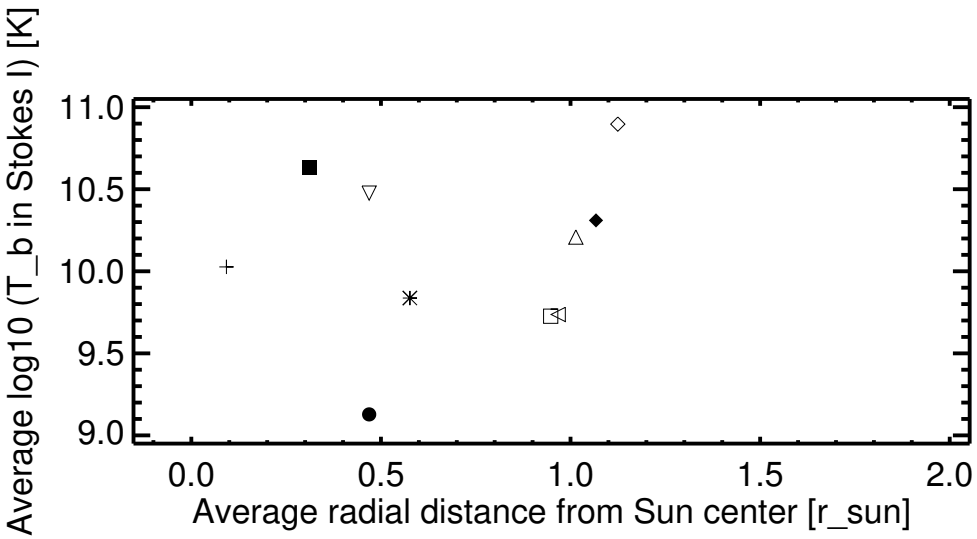

Figure 4.15: Variations of frequency-averaged $T_b(f)$ with averaged radial distance from the Sun's center. Different symbols indicate different events as identified in Table 4.1.

qualitatively consistent with the trend in Figure 4.13 that $T_b(f)$ increases with decreasing f.

We now investigate whether T_b has any dependency on the burst source's position or not (Figure 4.14). A few of the burst events are located near the disk center and rest of them near the limb and, as expected, $T_b(f)$ decreases as f increases. As radial distance r from the Sun's center increases, T_b does not show an obvious variation on the source's positions in Figure 4.14. Similarly, a frequency-averaged values of T_b for those events do not show an increase or decrease trend with r (Figure 4.15). From our results, it is unclear whether T_b depends on whether the source is located near the disk center or near the limb. This may be due to the small number of events considered, as discussed below in connection with the results of Dulk and Suzuki (1980).

4.7 Interpretation and Discussion

We consider that the source sizes can be affected by three effects: 1) divergence of open magnetic field lines to have large extent at lower frequencies and larger heights, 2) scattering effects, and 3) spatial resolution of the MWA beam. We discuss these issues in turn now.

Our observed source sizes are found to decrease as the frequency increases, with a very similar dependence to that for the beam area ($f^{-2.4\pm0.4}$ and $f^{-2.6\pm0.4}$ versus $f^{-2.5\pm0.2}$), and to be somewhere larger ($\leq$ a factor of 2) than the MWA beam sizes. Moreover, for most events (not all) the source eccentricity is constant with f, although 3 events have higher eccentricities at lower frequencies (Figure 4.9), and the beam and source eccentricities are different (Figures 4.8 and 4.9). Given that the WSClean processing removes the MWA beam from the images, we focus now on effects 1) and 2) above.

Divergence of open magnetic field lines likely plays a significant role in varying the intrinsic source size with frequency. We know that type III bursts are generated by semi-relativistic electrons released from the flare sites in active regions. These electrons are then accelerated outward from the corona along the open magnetic field lines. Direct evidence for diverging open field lines is provided by EUV imaging (Chen et al., 2013; McCauley et al., 2017; Cairns et al., 2018) and magnetic modelling (Masson et al., 2012, 2014). Based physically on a diverging field line topology, burst sources can be modelled as a filled cone centered on the Sun (Bougeret et al., 1970; Dulk et al., 1979). (The cone angles are the full widths to the 1/e points of the Gaussian sources) This angle can be larger than 70° for larger burst sources at larger heights and lower frequencies. The sources fill Sun-centered cone angles ranging from $\approx$ 35° to 65° at 169 MHz (Bougeret et al., 1970) to $\approx$ 40° to 72° at 80 MHz (Dulk and Suzuki, 1980). Interplanetary electrons associated with type IIIs fill a cone with an angle of $\approx$

100° near 20 kHz (Lin, 1974). Hence source sizes increase rapidly as f decreases and fill larger cones.

McCauley et al. (2017) studied the morphology of type III burst sources splitting that split into two parts moving apart to low frequency but were a single component at a lower height and higher frequencies. As f decreased from ≈ 132 to 80 MHz, the burst sources were observed to elongate, become larger, and split into two components at larger heights. They interpreted this behaviour as being due to extreme divergence of open magnetic field lines, as the electrons generating the type III bursts followed the open field lines modelled independently. We will not focus on source splitting but instead on increasing source sizes at decreasing frequencies.

It is generally known that radio waves originating from a localized source can be scattered due to refraction and reflection by coronal density fluctuations (Melrose, 1989a). The scattering of burst emission due to density inhomogeneities of the solar corona can in principle explain larger source areas at lower frequencies. This scattering leads to larger angular broadening of the source (Fokker, 1965; Steinberg et al., 1971; Bastian, 1994; Subramanian and Cairns, 2011; Ingale et al., 2015). They added that scatter-broadened images might be elongated by radial magnetic field lines and this effect observable if the field lines are sufficiently aligned with the line of sight. Therefore, from these scenarios it is possible to expect a larger source area at higher heights and lower frequencies.

From our observations, we find that burst source sizes are elliptical in general and exhibit an increase in area as frequency decreases for all the events (Figures 4.3 and 4.5). We now consider quantitatively the simple hypothesis of divergence of open magnetic field lines, as illustrated by the cartoon in Figure 4.16. The burst source is considered to be intrinsic, compact, and smaller in size at a lower height, being closer to the electron release site. Then the open magnetic field lines which guide the electrons diverge more with increasing height. Thus

the intrinsic source begins to expand (elliptically) as the open field lines diverge to large separations at higher heights.

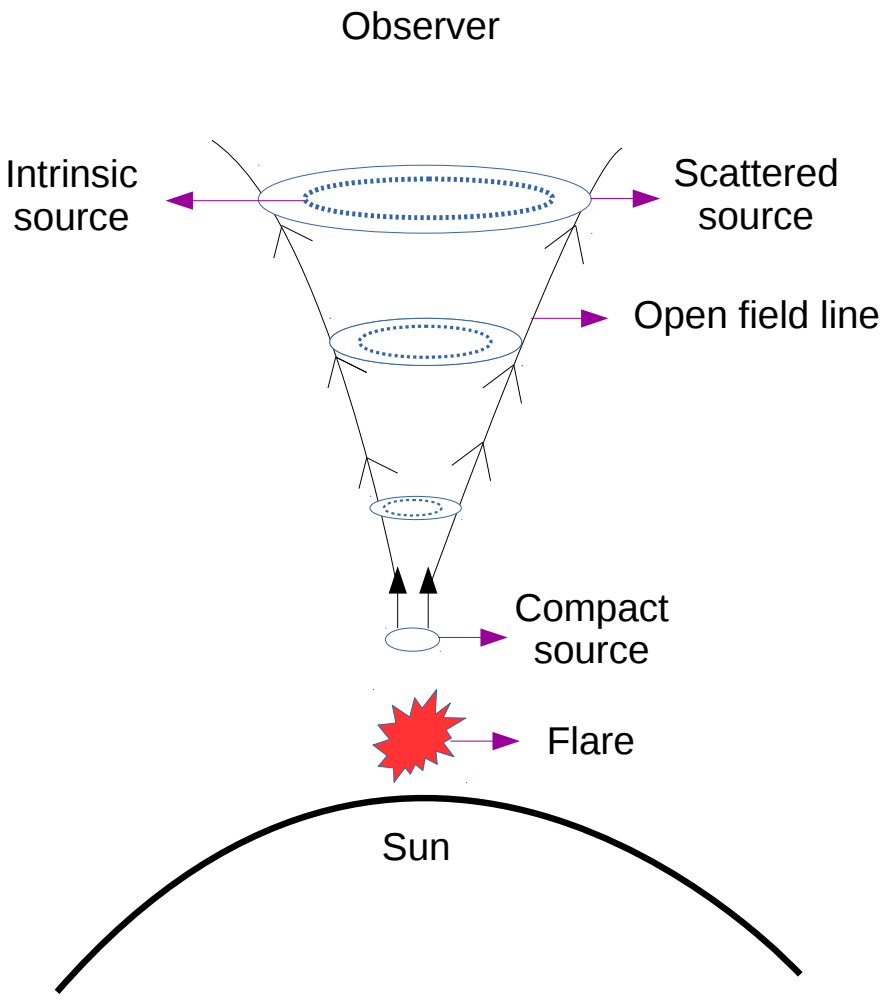

Figure 4.16: Cartoon representation of divergence of open magnetic field lines. The two open field lines (black curved lines) are diverging outward (indicated by arrows in black color) from the region of flare site. The dotted ellipse shows the intrinsic burst source that is assumed to be smaller and compact at the initial stage. The solid ellipse shows the scattered burst source.

Quantitative analyses of the scattering of radio emission in the solar atmo-

sphere predict a f^{-2} dependence on the linear source size (Fokker, 1965; Steinberg et al., 1971; Bastian, 1994; Cairns, 1998). Coles and Harmon (1989) confirmed this dependence from observations of cosmic sources through the corona. In our case, on average, the source area A (in Stokes I and V), which varies as the square of the linear source size, varies as $A \propto f^{-2.4\pm0.4}$ and $A \propto f^{-2.6\pm0.4}$ between 80 and 240 MHz, not the expected dependence f^{-4} expected from the f^{-2} dependence of the linear source sizes. Thus the frequency dependence of the observed source areas in Stokes I and V are quantitatively inconsistent with an interpretation in terms of scattering determining the observed source sizes. Only if one uses a non-traditional version of scattering theory, source area which yields $A \propto f^{-2.4\pm0.4}$ can the observations be interpreted in terms of scattering dominating the observed source sizes.

We note that ionospheric refraction can perturb the apparent position of burst sources in ground-based observations, exceeding a few arcmins in frequencies range from 100 to 300 MHz (Bougeret, 1981; Mercier, 1986). This effect can cause position shifts due to the ionospheric gravity waves (Saint-Hilaire et al., 2013). We neglect the effects of ionospheric refraction in our analysis.

The total and polarized fluxes are found to increase as frequency decreases for almost all the events (Figures 4.11 and 4.12). On average the total fluxes are greater than the polarized fluxes by a factor of 10 at lower frequencies near 80 MHz. Thus the sources are relatively weakly polarized emission, as found in Chapter 3.

It is well known that, in general, coronal type III bursts have brightness temperature T_b that varies from 10^6 K to even as high as 10^{15} K (Suzuki and Dulk, 1985; Kirk et al., 1994). The range of T_b for our type III burst events is between 1.2×10^8 K and 4×10^{11} K, smaller than those at 1 MHz (Evans et al., 1971) and type III bursts in the solar wind (Melrose, 1989a), where T_b is maximum $\approx 10^{15}$ K. These high brightness temperatures demonstrate

that the emission associated with type III bursts is coherent and non-thermal, consistent with earlier results of Dulk and Suzuki (1980) and Melrose (1989a). Our analyses show that T_b decreases with increasing f, consistent with those values of T_b ($\approx$ $2{\times}10^7$-$4{\times}10^{11}$ K at 80 MHz) observed by Dulk and Suzuki (1980).

Dulk and Suzuki (1980) suggested that T_b decreases from the disk center to the limb by a factor of three at frequencies between 43 and 160 MHz. Our results show no clear variation of T_b with the source's position (Figures 4.14 and 4.15), although we considered only a small number of events.

4.8 Conclusions

We studied the source sizes, fluxes, and brightness temperatures of 10 type III solar radio bursts using data from the MWA at frequencies from 80 to 240 MHz. The areas of both the polarized and unpolarized (total) sources increased as frequency decreased. We interpreted this in terms of the divergence of open magnetic field lines. On average the unpolarized source areas varied with frequency as $f^{-2.4\pm0.4}$, while the polarized source areas varied as $f^{-2.6\pm0.4}$ and the MWA beam sizes varied as $f^{-2.5\pm0.2}$. We did not find the expected dependence f^{-4} of the source area predicted from scattering theory. The temporal evolution of source area showed oscillatory behaviour at our time period, which had consistency with previous observations. We showed that the frequency dependence of the source areas did not support scattering as the primary physical effect determining the observed source sizes. The source sizes were similar in magnitude but different in ellipticity and magnitude to the MWA beam. The brightness temperatures decreased as frequency increased, consistent with previous observations. We also found that the brightness temperatures did not depend on the positions of type III burst sources, although this result may

not be statistically significant due to the small sample size. We conclude that the divergence of open field lines is a viable process which causes the source size to increase as the frequency decreases.

Chapter 5

Summary and Future Work

5.1 Summary

After providing context to the thesis research in Chapter 1, Chapter 2 presented, analyzed, and interpreted MWA observations of coronal holes (CHs) in the frequency range 80−240 MHz. CHs are expected to be observed as dark structures across the bandwidth of MWA since CHs are low-density regions relative to the corona. Four CHs were observed near disk center and found to transition from being relatively dark structures at higher frequencies ($\gtrsim$ 145 MHz) to relatively bright structures at lower frequencies ($\lesssim$ 145 MHz). Some CHs showed a transition frequency near 145 MHz and others had that transition frequency near 130 MHz or 135 MHz. MWA observations were compared to FORWARD synthetic images based on the MAS model. The synthetic images obtained from model data did not exhibit the dark-to-bright transition so that this model was not consistent with our observations at lower frequencies. We proposed that the dark-to-bright transition results from refraction of radio waves from the surrounding corona into the low density CH regions, a process not included in the MAS-FORWARD model, and we developed a qualitative model based on refraction and the relative optical depths inside and outside a CH as a function of frequency. The optical depths calculated based on the MAS model were qualitatively consistent with our interpretation. We have therefore shown that propagation and relative absorption effects are a feasible explanation for the dark-to-bright transition exhibited by these CHs from high to low frequencies.

Chapter 3 described radio observations of circular polarization in sixteen isolated type III solar radio bursts observed by the MWA from 80 to 240 MHz. On average for the bursts, near onset we found 5−30% circular polarization at 80 MHz and 15−40% at 240 MHz whereas these percentages were 3−15% and 5−25% near burst maximum. We measured the polarization fraction as

a function of source position for all the events and, on average, near both burst onset and maximum we found higher polarization near the disk center and lower polarization near the limb. This is qualitatively consistent with results of the previous observations of Dulk and Suzuki (1980), although we analyzed small sample size. We studied total intensity (Stokes I), circularly polarized intensity (Stokes V), and polarization fraction ($\mid V \mid/I$) profiles of type III events as a function of position at times near burst maximum, and found symmetric Stokes I, V, and $\mid V \mid/I$ profiles for a burst event with no source motion but asymmetric $\mid V \mid/I$ profiles for two events which had source motion. We argued the asymmetric $\mid V \mid/I$ profiles are due to the contribution of fundamental emission at the front of a beam and motion of the burst source. Imaging of the polarization fraction for moving sources showed relatively higher polarization fraction at burst onset which was interpreted in terms of dominant fundamental plasma emission from the front of the beam. At burst maximum, the images showed lower polarization fraction, interpreted in terms of burst emission being a combination of fundamental and harmonic components. During the decay phase the emission was dominated again by the fundamental component, which decayed till the end of a burst with lesser polarization fraction; this was interpreted as being due to scattering. This pattern of fundamental, fundamental and harmonic, and then fundamental emission with time was consistent with the interpretations of Dulk et al. (1984), Robinson et al. (1994), and Robinson and Cairns (1998). We proposed that scattering effects can be a viable reason for having lower polarization fractions for type III events than predicted theoretically. Finally, we investigated the decay time t_d after peak intensity, finding it to decrease more rapidly with increasing frequencies with $t_d \propto f^{-2.0\pm0.1}$ as compared with the previous observations ($t_d \propto f^{-1.1\pm0.1}$). This result can be interpreted in terms of changes in the radial dependence of density turbulence with radial distance.

Chapter 4 analyzed low-frequency solar type III radio bursts observed by the MWA. Near times of burst maximum, the source sizes, flux densities, and brightness temperatures were studied for 10 type III events using total (Stokes I) and polarized intensity (Stokes V) images. We found that the source area (A) increased as frequency (f) decreased and varied as $A \propto f^{-2.4\pm0.4}$ and $A \propto f^{-2.6\pm0.4}$ in Stokes I and V images, respectively, whereas the MWA beam area varied as $f^{-2.5\pm0.2}$. Therefore, the measured source areas were not consistent with the expected dependence f^{-4} predicted from standard scattering theory. We proposed that the source areas, once separated from the effects of the MWA beam, did not support scattering theory and instead interpreted the data in terms of the divergence of open magnetic field lines causing the source size to increase at lower frequencies and larger heights. On average, the total and polarized fluxes were also found to increase as the frequency decreased. We found total fluxes, averaged over the sample, of 550 SFU at 80 MHz and 50 SFU at 240 MHz, whereas Dulk and Suzuki (1980) found the logarithmic flux density of type IIIs ranging from 0.2 to 4.8 at 80 MHz. Our flux values thus lie within the range of their flux values. On average the brightness temperatures T_b decreased as f increased and we found a maximum T_b = 4×10^{11} K at 80 MHz and a minimum T_b = 1.2×10^{8} K at 240 MHz. Our results for T_b are consistent with those of Dulk and Suzuki (1980) (T_b: $10^7 - 4 \times 10^{11}$ at 80 MHz). We found that T_b did not depend on the source's position, but this finding is uncertain due to the small sample size and so not necessarily and inconsistent with the results of Dulk and Suzuki (1980). We argued that divergence of open field lines is a viable process for increasing source size as the frequency decreases.

5.2 Future Work

Some suggestions for future work on radio observations of coronal holes (CHs) are the following:

1. Flux calibrated MWA data of CHs for longer observing periods are needed to observe the dark-to-bright transition of multiple low-latitude radio CHs that move from disk center to limb. CHs are always observed as darker regions near the limb though. The data from MWA that we used for our analysis are for CHs near the disk center but not near the limb. Our qualitative model for the dark-to-bright transition would expect CHs to diminish in brightness with proximity to the limb since the radiation is being refracted radially and so not towards the Earth, and future work could investigate this potential viewing angle effect by examining CHs continuously as they transit the Sun from limb to limb.

2. A ray tracing calculation or simulation using the MAS model for the background corona and CH structure is needed to test the refraction and propagation mechanism proposed for the dark-to-bright transition of CHs. This is required in order to know the underlying physics for why many CHs to become brighter at lower frequencies and darker at higher frequencies. It will also lead to an explanation for why all CHs do not show this behaviour.

3. The reason for the varying transition frequency (the corresponding frequency at which a CH structure transitions to being bright from dark) for each CH is still not clear and must be addressed in future work, such as new observations and ray tracing calculations.

4. The brightness temperature (T_b) is an important parameter to examine whether an observed emission is classified as thermal or non-thermal.

For thermal emission, one finds $T_b < T$, where T is the temperature of the radiating particles. On the other hand, non-thermal emission has $k_B T_b > \epsilon$, where ϵ is a typical energy of the radiating particles. The emission associated with the CHs is likely to be thermal (bremsstrahlung) due to CHs having low-temperature electrons, smaller densities, and exhibiting less activity in the solar corona as compared to the highly dynamic active regions, whereas active regions typically emit non-thermal radiation. It is thus necessary to measure the brightness temperature of CHs to confirm that whether the emission coming from these low-density darker regions is really thermal or non-thermal as compared to the surrounding corona.

Possible investigations on solar type III radio bursts that can be done in future research include the following:

1. The time resolution (0.5 s) of the MWA data is not good enough to classify the structures of type III bursts robustly as fundamental, harmonic, fundamental-harmonic pair, and structureless. In other words, it is not possible to clarify the structure of bursts only by seeing their appearance from the dynamic spectra constructed from current MWA data. We need type III burst data with better time resolution ($\sim$ 0.1 s) to address this issue. Only then we can expect to definitively separate fundamental and harmonic bands for type IIIs.

2. A more extended statistical survey of circular polarization properties of type III bursts is needed to extend the analysis in Chapter 3. This study should definitely examine the positional dependence of polarization.

3. We note that we do not have magnetic observations as a function of height in the corona. From Equation (3.1), it would be interesting to compare

the degree of circular polarization with the magnetic field and ratio f_B/f_p using some model predictions. As an example of what is possible now (but beyond this thesis), the PFSS model (Schatten et al., 1969) and the FORWARD software package (Gibson et al., 2016) are viable ways to predict magnetic field values at different heights in the corona. This could help us to constrain magnetic field configurations in the corona at certain heights, which could be tested with MWA imaging observations of type IIIs, since we know that type IIIs preserve pristine information of magnetic field at burst generation sites.

4. The positional dependence of brightness temperature could be interesting to study for a large set of burst events to verify the suggestion of Dulk and Suzuki (1980) that the brightness temperature is larger on average when the burst source is near the disk center and smaller near the limb.

5. Along with MWA data, some LOFAR (Low Frequency Array) data could also be interesting in future research (Morosan et al., 2014; Reid and Kontar, 2018; Zhang et al., 2019).

5.3 Conclusions

We presented MWA radio observations of CHs that showed the dark-to-bright transition in their structures as we move from high to low frequencies. We developed a qualitative model that explained this transition based on refraction and propagation effects was consistent. The circular polarization properties of multiple type III solar radio bursts were studied, followed by measurements of the positional dependence on polarization. The average degree of circular polarization increased with increasing frequencies for both burst onset and maximum burst intensity, and circular polarization was dependent on the

source's position, were consistent with the previous observations. We then performed spectropolarimetric imaging studies for moving burst sources, and the images (Stokes $\mid V \mid/I$) showed larger polarization near the burst onset, smaller polarization near the peak burst intensity, and then lesser polarization than burst maximum during the decay phase. We observed the intriguing properties of type IIIs: source sizes, source fluxes, and brightness temperatures using the total (Stokes I) and polarized intensity (Stokes V) images. These measurements were compared with the previous observations and found to be qualitatively consistent. These investigations were performed using the MWA data for small sample size, and new observations with better time resolution are needed to test our results.

The important results of this thesis work are summarised as the following:

1. We observed the dark-to-bright transition of four radio CHs using the MWA data and interpreted this transition in terms of refraction and propagation effects causing CH structures to dark at higher frequencies and bright at lower frequencies. The density and temperature properties of CHs extracted from the MAS-FORWARD model were qualitatively consistent with this interpretation.

2. We performed circular polarization measurements of sixteen isolated type III solar radio bursts using data from the MWA. We found the average degree of circular polarization to be 9−24% at burst onset and 4−22% at burst maximum in frequencies ranging from 80 to 240 MHz. We found that the sense of polarization (left hand or right hand) did not change over frequency and time during a burst, which was consistent with the previous observations of Dulk and Suzuki (1980) and Mercier (1990).

3. The positional type III dependence of circular polarization fractions showed on average higher polarization fraction near the disk center and lower

polarization fraction near the limb, which was consistent with the previous observations of Dulk and Suzuki (1980) and with type I bursts (Aschwanden, 1986). One of the three possible alternative ways described by Melrose (1989b) to reduce the polarization of F emission scattering is that a large angle scatter can change polarization significantly; specifically, a scatter through an angle $\theta \approx 90^{\circ}$ reduces the polarization to ≈ 0. Some observations argue that depolarization mechanism that is happened in the burst source region is due to the scattering effect (Wentzel, 1984).

4. We found symmetric total intensity (Stokes I), polarized flux (Stokes V), and polarization fraction ($\mid V \mid/I$) profiles for one type III burst event without source motion and asymmetric $\mid V \mid/I$ profiles for two events which had source motion. We argued that these asymmetric $\mid V \mid/I$ profiles were due to the contribution of fundamental emission at the front of an electron beam and motion of the burst source.

5. The polarized flux profile of one type III burst example peaked before the total intensity profile that results in a "spike polarization" (Santin, 1976; Benz and Zlobec, 1978). This could happen after the mode conversion, where o-mode waves travel faster and reaches us first. We argued that the burst emission was highly circularly-polarized fundamental plasma emission with o-mode.

6. The polarized emission showed a rapid fall off, perhaps even faster than exponentially than the total emission with time at a given f after the burst peaks. This is interpreted in terms of depolarization effects being more prominent at the decay phase of bursts, for instance, scattering in the source and along the path.

7. We performed spectropolarimetric imaging studies for type III bursts with

moving sources. At burst onset the images showed higher polarization fraction, which was interpreted in terms of dominant fundamental plasma emission. At burst maximum, a lower polarization fraction was obtained, interpreted in terms of burst emission being a combination of fundamental and harmonic components. During the decay phase the emission was dominated again by the fundamental component, which decayed till the end of a burst with lesser polarization fraction; this was interpreted as being due to scattering. This pattern of fundamental, fundamental and harmonic, and then fundamental emission with time is consistent with the interpretations of Dulk et al. (1984), Robinson et al. (1994), and Robinson and Cairns (1998).

8. We investigated the decay time t_d after peak intensity and found it to decrease more rapidly with increasing frequencies with $t_d \propto f^{-2.0\pm0.1}$ as compared with the previous observations ($t_d \propto f^{-1.1\pm0.1}$). This is interpreted that intensity of fundamental emission falls off exponentially with time after the peak due to scattering by density irregularities and losses by linear mode conversion.

9. The source sizes, flux densities, and brightness temperatures of ten type III bursts were estimated from the MWA data in both Stokes I and V images. The source area A increased as frequency f decreased and varied as $A \propto f^{-2.4\pm0.4}$ and $A \propto f^{-2.6\pm0.4}$ in Stokes I and V images, whereas the MWA beam area varied as $A \propto f^{-2.5\pm0.2}$. Our source size data therefore do not support the interpretation that scattering determines the source size, since standard scattering theory predicts an f^{-4} dependence. We interpreted the increasing source size with decreased frequency in terms of divergence of open magnetic field lines, which causes the source area to increase at lower frequencies and larger heights.

10. The average total intensities of burst sources were found to be 550 and 50 SFU at 80 and 240 MHz, respectively, consistent with the flux results of Dulk and Suzuki (1980). The brightness temperatures T_b that we found ranged from a maximum of $4{\times}10^{11}$ K at 80 MHz to a minimum of $1.2{\times}10^{8}$ K at 240 MHz. Our results of T_b are consistent with those of Dulk and Suzuki (1980).

Finally, this thesis work will be helpful in understanding the activities of the quiet Sun, corona, active regions, solar flares, and coronal holes, as well as the properties of different emission mechanisms: gyromagnetic, bremsstrahlung, and plasma emissions. This work touches on the generation and propagation of radio waves into the solar corona and dark-to-bright transitions of coronal holes resulting from refraction and propagation effects. It has implications for two possible solutions to open problems in the study of Type III solar radio bursts: scattering effects and linear mode conversion as depolarization catalysts for type III bursts having lower polarization and the divergence of the open magnetic field lines being a viable process that causes the burst source sizes to increase at lower frequencies and larger heights. Finally, this work is useful in the ongoing study of intriguing features of type III solar radio bursts: circular polarization, source sizes, source fluxes, and brightness temperatures using the MWA data at the frequencies ranging from 80 to 240 MHz.

Bibliography

Alissandrakis CE. Radio observations of the quiet solar corona. Adv Space Res 1994; 14:81–91.

Alissandrakis CE, Lantos P, Nicolaidis E. Coronal structures observed at metric wavelengths with the Nançay radioheliograph. Sol Phys 1985; 97:267–282.

Alvarez H, Haddock FT. Decay time of type III solar bursts observed at kilometric wavelengths. Sol Phys 1973a; 30:175–182.

Alvarez H, Haddock FT. Solar wind density model from km-wave type III bursts. Sol Phys 1973b; 29:197–209.

Arzner K, Magun A. Radiowave propagation in a statistically inhomogeneous plasma. Astron Astrophys 1999; 351:1165–1189.

Aschwanden MJ. The polarization of decimetric pulsations. Sol Phys 1986; 104:57–65.

Aschwanden MJ. Physics of the Solar Corona. An Introduction with Problems and Solutions (2nd edition). 2005.

Aschwanden MJ, Benz AO, Dennis BR, Schwartz RA. Solar Electron Beams Detected in Hard X-Rays and Radio Waves. Astrophys J 1995; 455:347–365.

Axisa F, Avignon Y, Martres MJ, Pick M, Simon P. Solar coronal streamers observed at 169 MHz with the Nançay East-West radioheliograph. Sol Phys 1971; 19:110–127.

Bastian TS. Angular scattering of solar radio emission by coronal turbulence. Astrophys J 1994; 426:774–781.

Benz AO, Brajša R, Magdalenić J. Are There Radio-quiet Solar Flares? Sol Phys 2007; 240:263–270.

Benz AO, Grigis PC, Csillaghy A, Saint-Hilaire P. Survey on Solar X-ray Flares and Associated Coherent Radio Emissions. Sol Phys 2005; 226:121–142.

Benz AO, Monstein C, Beverland M, Meyer H, Stuber B. High Spectral Resolution Observation of Decimetric Radio Spikes Emitted by Solar Flares - First Results of the Phoenix-3 Spectrometer. Sol Phys 2009; 260:375–388.

Benz AO, Treumann R, Vilmer N, Mangeney A, Pick M, Raoult A. Evidence of primary and secondary bursts in solar type III emission. Astron Astrophys 1982; 108:161–168.

Benz AO, Zlobec P. Correlation between drift rate and polarization in solar type III radio bursts. Astron Astrophys 1978; 63:137–145.

Bougeret JL. Some effects produced by the ionosphere on radio interferometry - Fluctuations in apparent source position and image distortion. Astron Astrophys 1981; 96:259–266.

Bougeret JL, Caroubalos C, Mercier C, Pick M. Sources of Type III Solar Bursts Observed at 169 MHz with the Nançay Radiohellograph. Astron Astrophys 1970; 6:406.

Bowman JD, Cairns I, Kaplan DL, Murphy T, Oberoi D, Staveley-Smith L, Arcus W, Barnes DG, Bernardi G, Briggs FH, Brown S, Bunton JD, Burgasser AJ, Cappallo RJ, Chatterjee S, ECorey B, Coster A, Deshpande A, deSouza L, Emrich D, Erickson P, Goeke RF, Gaensler BM, Greenhill LJ, Harvey-Smith L, Hazelton BJ, Herne D, Hewitt JN, Johnston-Hollitt M, Kasper JC, Kincaid BB, Koenig R, Kratzenberg E, Lonsdale CJ, Lynch MJ, Matthews LD, McWhirter SR, Mitchell DA, Morales MF, Morgan EH, Ord SM, Pathikulangara J, Prabu T, Remillard RA, Robishaw T, Rogers AEE, Roshi AA, Salah JE, Sault RJ, Shankar NU, Srivani KS, Stevens JB, Subrahmanyan R, Tingay SJ, Wayth RB, Waterson M, Webster RL, Whitney AR, Williams AJ, Williams CL, Wyithe JSB. Science with the Murchison Widefield Array. Proc Astron Soc Aust 2013; 30:e031.

Briggs DS. High Fidelity Interferometric Imaging: Robust Weighting and NNLS Deconvolution. In: American Astronomical Society Meeting Abstracts, vol. 27 of Bull. American Astron. Soc. 1995; 1444.

Cairns IH. Plasma emission processes involving ion sound waves. 1986. Thesis (Ph. D.)–University of Sydney.

Cairns IH. Fundamental plasma emission involving ion sound waves. J Plasma Phys 1987a; 38:169–178.

Cairns IH. Second harmonic plasma emission involving ion sound waves. J Plasma Phys 1987b; 38:179–198.

Cairns IH. A semiquantitative theory for the $2f_p$ radiation observed upstream from the Earth's bow shock. J Geophys Res 1988; 93:3958–3968.

Cairns IH. Angular Broadening: Effects of Nonzero, Spatially Varying Plasma Frequency between the Source and Observer. Astrophys J 1998; 506:456–463.

Cairns IH. Coherent Radio Emissions Associated with Solar System Shocks. Dordrecht: Springer Netherlands, 2011.

Cairns IH, Lobzin VV, Donea A, Tingay SJ, McCauley PI, Oberoi D, Duffin RT, Reiner MJ, Hurley-Walker N, Kudryavtseva NA, Melrose DB, Harding JC, Bernardi G, Bowman JD, Cappallo RJ, Corey BE, Deshpand e A, Emrich D, Goeke R, Hazelton BJ, Johnston-Hollitt M, Kaplan DL, Kasper JC, Kratzenberg E, Lonsdale CJ, Lynch MJ, McWhirter SR, Mitchell DA, Morales MF, Morgan E, Ord SM, Prabu T, Roshi A, Shankar NU, Srivani KS, Subrahmanyan R, Wayth RB, Waterson M, Webster RL, Whitney AR, Williams A, Williams CL. Low Altitude Solar Magnetic Reconnection, Type III Solar Radio Bursts, and X-ray Emissions. Sci Rep 2018; 8:1676.

Cairns IH, Robinson PA. Theory for low-frequency modulated Langmuir wave packets. Geophys Res Lett 1992; 19:2187–2190.

Cairns IH, Robinson PA, Zank GP. Progress on Coronal, Interplanetary, Foreshock, and Outer Heliospheric Radio Emissions. Publ Astron Soc Aust 2000; 17:22–34.

Chen B, Bastian TS, White SM, Gary DE, Perley R, Rupen M, Carlson B. TRACING ELECTRON BEAMS IN THE SUN'S CORONA WITH RADIO DYNAMIC IMAGING SPECTROSCOPY. Astrophys J Lett 2013; 763:L21.

Coles WA, Harmon JK. Propagation observations of the solar wind near the sun. Astrophys J 1989; 337:1023–1034.

Cranmer SR. Coronal Holes. Living Rev Sol Phys 2009; 6:3.

DeForest CE, Lamy PL, Llebaria A. Solar Polar Plume Lifetime and Coronal Hole Expansion: Determination from Long-Term Observations. Astrophys J 2001; 560:490–498.

Dulk GA. Radio emission from the sun and stars. Annu Rev Astron Astrophys 1985; 23:169–224.

Dulk GA, Marsh KA. Simplified expressions for the gyrosynchrotron radiation from mildly relativistic, nonthermal and thermal electrons. Astrophys J 1982; 259:350–358.

Dulk GA, Melrose DB, Suzuki S. Evidence for extreme divergence of open field lines from solar active regions. Proc Astron Soc Aust 1979; 3:375–379.

Dulk GA, Nelson GJ. The Position of a Type I Storm Source in the Magnetic Field of an Active Region. Publ Astron Soc Aust 1973; 2:211–214.

Dulk GA, Sheridan KV. The Structure of the Middle Corona from Observations at 80 and 160 MHz. Sol Phys 1974; 36:191–202.

Dulk GA, Sheridan KV, Smerd SF, Withbroe GL. Radio and EUV observations of a coronal hole. Sol Phys 1977; 52:349–367.

Dulk GA, Steinberg JL, Hoang S. Type III bursts in interplanetary space - Fundamental or harmonic? Astron Astrophys 1984; 141:30–38.

Dulk GA, Suzuki S. The position and polarization of Type III solar bursts. Astron Astrophys 1980; 88:203–217.

Duncan RA. Rapid fluctuations in the position, size, and brightness of intense solar metre-wave radio sources. Sol Phys 1985; 97:173–182.

Emslie AG, Kucharek H, Dennis BR, Gopalswamy N, Holman GD, Share GH, Vourlidas A, Forbes TG, Gallagher PT, Mason GM, Metcalf TR, Mewaldt RA, Murphy RJ, Schwartz RA, Zurbuchen TH. Energy partition in two solar flare/CME events. J Geophys Res 2004; 109:A10104.

Evans LG, Fainberg J, Stone RG. A comparison of type III solar radio burst theories using satellite radio observations and particle measurements. Sol Phys 1971; 21:198–203.

Evans LG, Fainberg J, Stone RG. Characteristics of type III exciters derived from low frequency radio observations. Sol Phys 1973; 31:501–511.

Fokker AD. Coronal scattering of radiation from solar radio sources. Bull Astron Inst Neth 1965; 18:111.

Freeland S, Handy B. Data Analysis with the SolarSoft System. Sol Phys 1998; 182:497–500.

Ganse U, Kilian P, Vainio R, Spanier F. Emission of Type II Radio Bursts – Single-Beam Versus Two-Beam Scenario. Sol Phys 2012; 280:551–560.

Gary DE, Hurford GJ. Radio Spectral Diagnostics. Dordrecht: Springer Netherlands, 2005.

Gelfreikh GB. Coronal Magnetic Field Measurements Through Bremsstrahlung Emission. In: Gary DE, Keller CU, editors. Astrophys. Space Sci. Lib., vol. 314. 2004; 115.

Gibson S, Kucera T, White S, Dove J, Fan Y, Forland B, Rachmeler L, Downs C, Reeves K. FORWARD: A toolset for multiwavelength coronal magnetometry. Front Astron Space Sci 2016; 3:8.

Gibson SE, Kucera TA, Rastawicki D, Dove J, de Toma G, Hao J, Hill S, Hudson HS, Marqué C, McIntosh PS, Rachmeler L, Reeves KK, Schmieder B, Schmit DJ, Seaton DB, Sterling AC, Tripathi D, Williams DR, Zhang M. Three-dimensional Morphology of a Coronal Prominence Cavity. Astrophys J 2010; 724:1133–1146.

Ginzburg VL, Zhelezniakov VV. On the Possible Mechanisms of Sporadic Solar Radio Emission (Radiation in an Isotropic Plasma). Sov Astron 1958; 2:653.

Golap K, Sastry CV. The radio brightness of the undisturbed outer solar corona in the presence of a radial magnetic field. Sol Phys 1994; 150:295–304.

Goldman MV. Progress and problems in the theory of type III solar radio emission. Sol Phys 1983; 89:403–442.

Goldman MV. Strong turbulence of plasma waves. Rev Mod Phys 1984; 56:709–735.

Golub L, Pasachoff JM. The Solar Corona. Cambridge University Press, 2010.

Graham DB, Cairns IH. Electrostatic decay of Langmuir/z-mode waves in type III solar radio bursts. J Geophys Res 2013; 118:3968–3984.

Gurnett DA, Bhattacharjee A. Introduction to Plasma Physics. 2005.

Hamidi ZS, Shariff NNM. Investigation of Characteristics of Noise Storm Solar Burst Type I on 11th March 2013. In: Kim KJ, Kim H, editors. Mobile and Wireless Technology 2018. Singapore: Springer Singapore, 2019; 361–367.

Hartree DR. The Propagation of Electromagnetic Waves in a Refracting Medium in a Magnetic Field. Proc Camb Phil Soc 1931; 27:143–162.

Harvey JW, Sheeley NR Jr. Coronal holes and solar magnetic fields. Space Sci Rev 1979; 23:139–158.

Hayes LM. Reflection of magnetoionic waves from a steep density gradient. I - Incident extraordinary mode. Aust J Phys 1985a; 38:687–704.

Hayes LM. Reflection of magnetoionic waves from a steep density gradient. II - Incident ordinary mode. Aust J Phys 1985b; 38:705–714.

He J, Marsch E, Tu C, Tian H, Guo L, Curdt W, Xia L, Kamio S. A new view of solar wind origin near active regions and in polar coronal holes on the basis of Hinode observations. In: 38th COSPAR Scientific Assembly, vol. 38 of COSPAR Meeting. 2010; 9.

Hudson HS. Coronal holes as seen in soft X-rays by Yohkoh. In: Wilson A, editor. From Solar Min to Max: Half a Solar Cycle with SOHO, vol. 508 of ESA Special Publication. 2002; 341–349.

Hutchinson IH. Principles of Plasma Diagnostics. Cambridge University Press, Cambridge, UK. p. 109. 2005.

Ingale M, Subramanian P, Cairns I. Coronal turbulence and the angular broadening of radio sources - the role of the structure function. Mon Not Roy Astron Soc 2015; 447:3486–3497.

Kai K. The structure, polarization, and spatial relationship of solar radio sources of spectral types I and III. Sol Phys 1970; 11:456–466.

Kai K, Sheridan KV. Coronal magnetic field structure derived from two-frequency radioheliograph observations. Sol Phys 1974; 35:181–192.

Kim EH, Cairns IH, Robinson PA. Extraordinary-Mode Radiation Produced by Linear-Mode Conversion of Langmuir Waves. Phys Rev Lett 2007; 99:015003.

Kim EH, Cairns IH, Robinson PA. Mode conversion of Langmuir to electromagnetic waves at magnetic field-aligned density inhomogeneities: Simulations, theory, and applications to the solar wind and the corona. Phys Plasmas 2008; 15:102110–102110.

Kirk JG, Melrose DB, Priest ER. Plasma Astrophysics. Springer-Verlag, 1994.

Kivelson MG, Russell CT. Introduction to Space Physics, Cambridge University Press, UK. 1995.

Kontar EP, Yu S, Kuznetsov AA, Emslie AG, Alcock B, Jeffrey NLS, Melnik VN, Bian NH, Subramanian P. Imaging spectroscopy of solar radio burst fine structures. Nat Commun 2017; 8:1515.

Krupar V, Santolik O, Maksimovic M, Cecconi B. Type III Radio Bursts at Long Wavelengths: STEREO/Waves Observations and Future Prospects for Inner Heliospheric Missions. AGU Fall Meet Abstr 2011; SH33B-2048.

Kundu MR. The Nature of Type IV Solar Radio Bursts. J Phys Soc Jpn Supp 1962; 17:215.

Kundu MR. Solar radio astronomy, Interscience Publication, New York. 1965.

Lang KR. The Cambridge Encyclopedia of the Sun. 2001.

Lantos P. Low Frequency Observations of the Quiet Sun: a Review. In: Bastian TS, Gopalswamy N, Shibasaki K, editors. Proc. Nobeyama Symp., vol. 479. 1999; 11–24.

Lantos P, Alissandrakis CE. Meter wavelength observations of the quiet sun and the slowly varying component during declining phase of the solar cycle. Adv Space Res 1994; 14:97–102.

Lantos P, Alissandrakis CE. Analysis of coronal emissions observed at meter wavelengths. Astron Astrophys 1999; 351:373–381.

Lantos P, Alissandrakis CE, Gergely T, Kundu MR. Quiet sun and slowly varying component at meter and decameter wavelengths. Sol Phys 1987; 112:325–340.

Lantos P, Alissandrakis CE, Rigaud D. Quiet-Sun emission and local sources at meter and decimeter wavelengths and their relationship with the coronal neutral sheet. Sol Phys 1992; 137:225–256.

Leblanc Y, Dulk GA, Bougeret JL. Tracing the Electron Density from the Corona to 1au. Sol Phys 1998; 183:165–180.

Lemen JR, Title AM, Akin DJ, Boerner PF, Chou C, Drake JF, Duncan DW, Edwards CG, Friedlaender FM, Heyman GF, Hurlburt NE, Katz NL, Kushner GD, Levay M, Lindgren RW, Mathur DP, McFeaters EL, Mitchell S, Rehse RA, Schrijver CJ, Springer LA, Stern RA, Tarbell TD, Wuelser JP, Wolfson CJ, Yanari C, Bookbinder JA, Cheimets PN, Caldwell D, Deluca EE, Gates R, Golub L, Park S, Podgorski WA, Bush RI, Scherrer PH, Gummin MA, Smith P, Auker G, Jerram P, Pool P, Soufli R, Windt DL, Beardsley S, Clapp M, Lang J, Waltham N. The Atmospheric Imaging Assembly (AIA) on the Solar Dynamics Observatory (SDO). Sol Phys 2012; 275:17–40.

Lenc E, Anderson CS, Barry N, Bowman JD, Cairns IH, Farnes JS, Gaensler BM, Heald G, Johnston-Hollitt M, Kaplan DL, Lynch CR, McCauley PI, Mitchell DA, Morgan J, Morales MF, Murphy T, Offringa AR, Ord SM, Pindor B, Riseley C, Sadler EM, Sobey C, Sokolowski M, Sullivan IS, O'Sullivan SP, Sun XH, Tremblay SE, Trott CM, Wayth RB. The Challenges of Low-Frequency Radio Polarimetry: Lessons from the Murchison Widefield Array. Publ Astron Soc Aust 2017; 34:e040.

Li B, Cairns IH, Gosling JT, Malaspina DM, Neudegg D, Steward G, Lobzin VV. Comparisons of mapped magnetic field lines with the source path of the 7 April 1995 type III solar radio burst. J Geophys Res 2016; 121:6141–6156.

Li B, Cairns IH, Robinson PA. Imprints of coronal temperature disturbances on type III bursts. Astron Astrophys 2010; 510:L6.

Li B, Willes AJ, Robinson PA, Cairns IH. Second harmonic electromagnetic emission via beam-driven Langmuir waves. Phys Plasmas 2005; 12:012103.

Li W, Pober JC, Hazelton BJ, Barry N, Morales MF, Sullivan I, Parsons AR, Ali ZS, Dillon JS, Beardsley AP, Bowman JD, Briggs F, Byrne R, Carroll P, Crosse B, Emrich D, Ewall-Wice A, Feng L, Franzen TMO, Hewitt JN, Horsley L, Jacobs DC, Johnston-Hollitt M, Jordan C, Joseph RC, Kaplan DL, Kenney D, Kim H, Kittiwisit P, Lanman A, Line J, McKinley B, Mitchell DA, Murray S, Neben A, Offringa AR, Pallot D, Paul S, Pindor B, Procopio P, Rahimi M, Riding J, Sethi SK, Udaya Shankar N, Steele K, Subrahmanian R, Tegmark M, Thyagarajan N, Tingay SJ, Trott C, Walker M, Wayth RB, Webster RL, Williams A, Wu C, Wyithe S. Comparing Redundant and Sky-model-based Interferometric Calibration: A First Look with Phase II of the MWA. Astrophys J 2018; 863:170.

Lin RP. Non-relativistic solar electrons. Space Sci Rev 1974; 16:189–256.

Lin RP, Evans LG, Fainberg J. Simultaneous Observations of Fast Solar Electrons and Type III Radio Burst Emission Near 1 AU. Astrophys Lett 1973; 14:191.

Linker JA, Mikić Z, Biesecker DA, Forsyth RJ, Gibson SE, Lazarus AJ, Lecinski A, Riley P, Szabo A, Thompson BJ. Magnetohydrodynamic modeling of the solar corona during Whole Sun Month. J Geophys Res 1999; 104:9809–9830.

Lionello R, Linker JA, Mikić Z. MULTISPECTRAL EMISSION OF THE SUN DURING THE FIRST WHOLE SUN MONTH: MAGNETOHYDRODYNAMIC SIMULATIONS. Astrophys J 2009; 690:902–912.

Lonsdale CJ, Cappallo RJ, Morales MF, Briggs FH, Benkevitch L, Bowman JD, Bunton JD, Burns S, Corey BE, Desouza L, Doeleman SS, Derome M,

Deshpande A, Gopala MR, Greenhill LJ, Herne DE, Hewitt JN, Kamini PA, Kasper JC, Kincaid BB, Kocz J, Kowald E, Kratzenberg E, Kumar D, Lynch MJ, Madhavi S, Matejek M, Mitchell DA, Morgan E, Oberoi D, Ord S, Pathikulangara J, Prabu T, Rogers A, Roshi A, Salah JE, Sault RJ, Shankar NU, Srivani KS, Stevens J, Tingay S, Vaccarella A, Waterson M, Wayth RB, Webster RL, Whitney AR, Williams A, Williams C. The Murchison Widefield Array: Design Overview. IEEE Proc 2009; 97:1497–1506.

Low BC, Hundhausen JR. Magnetostatic structures of the solar corona. 2: The magnetic topology of quiescent prominences. Astrophys J 1995; 443:818–836.

Ma Y, xiang Xie R, min Zheng X, Wang M, Yi-hua Y. A Statistical Analysis of the Type-III Bursts in Centimeter and Decimeter Wavebands. Chin Astron Astrophys 2012; 36:175–186.

Masson S, Aulanier G, Pariat E, Klein KL. Interchange Slip-Running Reconnection and Sweeping SEP Beams. Sol Phys 2012; 276:199–217.

Masson S, McCauley P, Golub L, Reeves KK, DeLuca EE. DYNAMICS OF THE TRANSITION CORONA. Astrophys J 2014; 787:145.

Maxwell A, Swarup G. A New Spectral Characteristic in Solar Radio Emission. Nat 1958; 181:36–38.

McCauley PI, Cairns IH, Morgan J. Densities Probed by Coronal Type III Radio Burst Imaging. Sol Phys 2018; 293:132.

McCauley PI, Cairns IH, Morgan J, Gibson SE, Harding JC, Lonsdale C, Oberoi D. Type III Solar Radio Burst Source Region Splitting due to a Quasi-separatrix Layer. Astrophys J 2017; 851:151.

McCauley PI, Cairns IH, White SM, Mondal S, Lenc E, Morgan J, Oberoi D.

The Low-Frequency Solar Corona in Circular Polarization. Sol Phys 2019; 294:106.

McLean DJ. Radioheliograph observations of harmonic type III solar bursts. Aust J Phys 1971; 24:201.

McLean DJ, Labrum NR. Solar radiophysics: Studies of emission from the sun at metre wavelengths. 1985.

Melnik VN, Konovalenko AA, Rucker HO, Boiko AI, Dorovskyy VV, Abranin EP, Lecacheux A. Observations of Powerful Type III Bursts in the Frequency Range 10 – 30 MHz. Sol Phys 2011; 269:335–350.

Melrose DB. Fundamental emission for type III bursts in the interplanetary medium: The role of ion-sound turbulence. Sol Phys 1982; 79:173–185.

Melrose DB. Instabilities in Space and Laboratory Plasmas, Cambridge University Press, Cambridge, UK. 1986.

Melrose DB. The brightness temperatures of solar type III bursts. Sol Phys 1989a; 120:369–381.

Melrose DB. Depolarization of solar bursts due to scattering by low-frequency waves. Sol Phys 1989b; 119:143–156.

Melrose DB. The brightness temperatures of solar type III bursts. Bull Am Phys Soc 1989; 34:1293.

Melrose DB. Coherent emission. In: Gopalswamy N, Webb DF, editors. Universal Heliophysical Processes, vol. 257 of IAU Symposium. 2009; 305–315.

Melrose DB, Dulk GA, Gary DE. Corrected formula for the polarization of second harmonic plasma emission. Proc Astron Soc Aust 1980; 4:50–53.

Melrose DB, Sy WN. Plasma emission processes in a magnetoactive plasma. Aust J Phys 1972; 25:387.

Mercier C. Observations of atmospheric gravity waves by radiointerferometry. J Atmospheric Terr Phys 1986; 48:605–624.

Mercier C. Polarisation of type III bursts between 164 and 435 MHz - Structure and variation with frequency. Sol Phys 1990; 130:119–129.

Mercier C, Chambe G. High Dynamic Range Images of the Solar Corona Between 150 and 450 MHz. Astrophys J 2009; 700:L137–L140.

Mercier C, Chambe G. Morphology of the quiet Sun between 150 and 450 MHz as observed with the Nançay radioheliograph. Astron Astrophys 2012; 540:A18.

Mercier C, Subramanian P, Kerdraon A, Pick M, Ananthakrishnan S, Janardhan P. Combining visibilities from the giant meterwave radio telescope and the Nancay radio heliograph. High dynamic range snapshot images of the solar corona at 327 MHz. Astron Astrophys 2006; 447:1189–1201.

Mohan A, Mondal S, Oberoi D, Lonsdale CJ. Evidence for Super-Alfvénic Oscillations in Solar Type III Radio Burst Sources. Astrophys J 2019; 875:98.

Mohan A, Oberoi D. 4D Data Cubes from Radio-Interferometric Spectroscopic Snapshot Imaging. Sol Phys 2017; 292:168.

Morosan DE, Gallagher PT, Zucca P, Fallows R, Carley EP, Mann G, Bisi MM, Kerdraon A, Konovalenko AA, MacKinnon AL, Rucker HO, Thidé B, Magdalenić J, Vocks C, Reid H, Anderson J, Asgekar A, Avruch IM, Bentum MJ, Bernardi G, Best P, Bonafede A, Bregman J, Breitling F, Broderick J, Brüggen M, Butcher HR, Ciardi B, Conway JE, de Gasperin F, de Geus E,

Deller A, Duscha S, Eislöffel J, Engels D, Falcke H, Ferrari C, Frieswijk W, Garrett MA, Grießmeier J, Gunst AW, Hassall TE, Hessels JWT, Hoeft M, Hörandel J, Horneffer A, Iacobelli M, Juette E, Karastergiou A, Kondratiev VI, Kramer M, Kuniyoshi M, Kuper G, Maat P, Markoff S, McKean JP, Mulcahy DD, Munk H, Nelles A, Norden MJ, Orru E, Paas H, Pandey-Pommier M, Pandey VN, Pietka G, Pizzo R, Polatidis AG, Reich W, Röttgering H, Scaife AMM, Schwarz D, Serylak M, Smirnov O, Stappers BW, Stewart A, Tagger M, Tang Y, Tasse C, Thoudam S, Toribio C, Vermeulen R, van Weeren RJ, Wucknitz O, Yatawatta S, Zarka P. LOFAR tied-array imaging of Type III solar radio bursts. Astron Astrophys 2014; 568:A67.

Munro RH, Withbroe GL. Properties of a Coronal "hole" Derived from Extreme-Ultraviolet Observations. Astrophys J 1972; 176:511.

Nelson GJ, Melrose DB. Type II bursts. 1985.

Newkirk G Jr. The Solar Corona in Active Regions and the Thermal Origin of the Slowly Varying Component of Solar Radio Radiation. Astrophys J 1961; 133:983.

Newkirk G Jr. Structure of the Solar Corona. Annu Rev Astron Astrophys 1967; 5:213.

Nita GM, Gary DE, Lanzerotti LJ, Thomson DJ. The Peak Flux Distribution of Solar Radio Bursts. Astrophys J 2002; 570:423–438.

Oberoi D, Sharma R, Bhatnagar S, Lonsdale CJ, Matthews LD, Cairns IH, Tingay SJ, Benkevitch L, Donea A, White SM, Bernardi G, Bowman JD, Briggs F, Cappallo RJ, Corey BE, Deshpande A, Emrich D, Gaensler BM, Goeke R, Greenhill LJ, Hazelton BJ, Johnston-Hollitt M, Kaplan DL, Kasper JC, Kratzenberg E, Lynch MJ, McWhirter SR, Mitchell DA, Morales MF,

Morgan E, Offringa AR, Ord SM, Prabu T, Rogers AEE, Roshi A, Salah JE, Udaya Shankar N, Srivani KS, Subrahmanyan R, Waterson M, Wayth RB, Webster RL, Whitney AR, William A, Williams CL. Observing the Sun with the Murchison Widefield Array. ArXiv e-prints 2014; .

Oberoi D, Sharma R, Rogers AEE. Estimating Solar Flux Density at Low Radio Frequencies Using a Sky Brightness Model. Sol Phys 2017; 292:75.

Offringa AR, McKinley B, Hurley-Walker N, Briggs FH, Wayth RB, Kaplan DL, Bell ME, Feng L, Neben AR, Hughes JD, Rhee J, Murphy T, Bhat NDR, Bernardi G, Bowman JD, Cappallo RJ, Corey BE, Deshpande AA, Emrich D, Ewall-Wice A, Gaensler BM, Goeke R, Greenhill LJ, Hazelton BJ, Hindson L, Johnston-Hollitt M, Jacobs DC, Kasper JC, Kratzenberg E, Lenc E, Lonsdale CJ, Lynch MJ, McWhirter SR, Mitchell DA, Morales MF, Morgan E, Kudryavtseva N, Oberoi D, Ord SM, Pindor B, Procopio P, Prabu T, Riding J, Roshi DA, Shankar NU, Srivani KS, Subrahmanyan R, Tingay SJ, Waterson M, Webster RL, Whitney AR, Williams A, Williams CL. WSCLEAN: an implementation of a fast, generic wide-field imager for radio astronomy. Mon Not Roy Astron Soc 2014; 444:606–619.

Parker EN. Heating solar coronal holes. Astrophys J 1991; 372:719–727.

Priest ER. Solar magneto-hydrodynamics. 1982.

Rahman MM, McCauley PI, Cairns IH. On the Relative Brightness of Coronal Holes at Low Frequencies. Sol Phys 2019; 294:7.

Ramaty R, Lingenfelter RE. The Influence of the Ionized Medium on Synchrotron Emission Spectra in the Solar Corona. J Geophys Res 1967; 72:879.

Raoult A, Pick M. Space-time evolution of type III burst sources observed with

the Nancay radioheliograph - Implications for the size of the emitting source. Astron Astrophys 1980; 87:63–67.

Reid HAS, Kontar EP. Solar type III radio burst time characteristics at LOFAR frequencies and the implications for electron beam transport. Astron Astrophys 2018; 614:A69.

Reid HAS, Ratcliffe H. A review of solar type III radio bursts. Res Astron Astrophys 2014; 14:773–804.

Reid HAS, Vilmer N. Coronal type III radio bursts and their X-ray flare and interplanetary type III counterparts. Astron Astrophys 2017; 597:A77.

Riddle AC. On the observation of scattered radio emission from sources in the solar corona. Sol Phys 1974; 35:153–169.

Robinson PA, Cairns IH. Fundamental and harmonic radiation in type III solar radio bursts. Sol Phys 1994; 154:335–360.

Robinson PA, Cairns IH. Fundamental and Harmonic Emission in Type III Solar Radio Bursts – I. Emission at a Single Location or Frequency. Sol Phys 1998; 181:363–394.

Robinson PA, Cairns IH. Theory of Type III And Type II Solar Radio Emissions. Wash DC Am Geophys Union Geophys Monogr Series 2000; 119:37.

Robinson PA, Cairns IH, Willes AJ. Dynamics and Efficiency of Type III Solar Radio Emission. Astrophys J 1994; 422:870.

Robinson PA, Willes AJ, Cairns IH. Dynamics of Langmuir and Ion-Sound Waves in Type III Solar Radio Sources. Astrophys J 1993; 408:720.

Robinson RD. Scattering of radio waves in the solar corona. Proc Astron Soc Aust 1983; 5:208–211.

Rohlfs K, Wilson TL. Tools of radio astronomy. Springer-Verlag, Berlin. 2004.

Rybicki GB, Lightman AP. Radiative processes in astrophysics. Wiley-VCH, Weinheim. 1979.

Saint-Hilaire P, Vilmer N, Kerdraon A. A DECADE OF SOLAR TYPE III RADIO BURSTS OBSERVED BY THE NANÇAY RADIOHELIOGRAPH 1998-2008. Astrophys J 2013; 762:60.

Santin P. The time and polarization profile of type III solar radio bursts at meter wavelengths. Astron Astrophys 1976; 49:193–195.

Schatten KH, Wilcox JM, Ness NF. A model of interplanetary and coronal magnetic fields. Sol Phys 1969; 6:442–455.

Schonfeld SJ, White SM, Henney CJ, Hock-Mysliwiec RA, McAteer RTJ. The Slowly Varying Corona. II. The Components of F $_{10.7}$ and Their Use in EUV Proxies. Astrophys J 2019; 884:141.

Sheridan KV. Some Recent Explorations of the Solar Corona from the Culgoora Solar Radio Observatory. Publ Astron Soc Aust 1978; 3:185–194.

Sheridan KV, Dulk GA. Radio observations of coronal holes. In: Dryer M, Tandberg-Hanssen E, editors. Solar and Interplanetary Dynamics, vol. 91 of IAU Symp. 1980; .

Sheridan KV, Labrum NR, Payten WJ. Multiple-frequency Operation of the Culgoora Radioheliograph. Nat Phys Sci 1972; 238:115–116.

Shibasaki K, Alissandrakis CE, Pohjolainen S. Radio Emission of the Quiet Sun and Active Regions (Invited Review). Sol Phys 2011; 273:309–337.

Shibasaki K, Ishiguro M, Enome S, Tanaka H, editors. A coronal hole observed by 8-cm wavelength radioheliograph, COSPAR, 20th Plenary Meeting. 1977.

Smerd SF, Wild JP, Sheridan KV. On the Relative Position and Origin of Harmonics in the Spectra of Solar Radio Bursts of Spectral Types II and III. Aust J Phys 1962; 15:180.

Sokolowski M, Bhat NDR, Macquart JP, Shannon RM, Bannister KW, Ekers RD, Scott DR, Beardsley AP, Crosse B, Emrich D, Franzen TMO, Gaensler BM, Horsley L, Johnston-Hollitt M, Kaplan DL, Kenney D, Morales MF, Pallot D, Sleap G, Steele K, Tingay SJ, Trott CM, Walker M, Wayth RB, Williams A, Wu C. No Low-frequency Emission from Extremely Bright Fast Radio Bursts. Astrophys J Lett 2018; 867:L12.

Staehli M, Benz AO. Microwave emission of solar electron beams. Astron Astrophys 1987; 175:271–276.

Steinberg JL, Aubier-Giraud M, Leblanc Y, Boischot A. Coronal Scattering, Absorption and Refraction of Solar Radiobursts. Astron Astrophys 1971; 10:362.

Subramanian P, Cairns I. Constraints on coronal turbulence models from source sizes of noise storms at 327 MHz. J Geophys Res 2011; 116:A03104.

Suresh A, Sharma R, Oberoi D, Das SB, Pankratius V, Timar B, Lonsdale CJ, Bowman JD, Briggs F, Cappallo RJ, Corey BE, Deshpande AA, Emrich D, Goeke R, Greenhill LJ, Hazelton BJ, Johnston-Hollitt M, Kaplan DL, Kasper JC, Kratzenberg E, Lynch MJ, McWhirter SR, Mitchell DA, Morales MF, Morgan E, Ord SM, Prabu T, Rogers AEE, Roshi A, Udaya Shankar N, Srivani KS, Subrahmanyan R, Tingay SJ, Waterson M, Wayth RB, Webster RL, Whitney AR, Williams A, Williams CL. Wavelet-based Characterization of Small-scale Solar Emission Features at Low Radio Frequencies. Astrophys J 2017; 843:19.

Sutinjo A, O'Sullivan J, Lenc E, Wayth RB, Padhi S, Hall P, Tingay SJ. Understanding instrumental Stokes leakage in Murchison Widefield Array polarimetry. Radio Sci 2015; 50:52–65.

Suzuki S, Dulk GA. Bursts of Type III and Type V (Solar Radiophysics: Studies of Emission from the Sun at Metre Wavelengths). 1985.

Suzuki S, Sheridan KV. Observations of the circular polarization of fundamental and harmonic type III bursts throughout the frequency range 24 to 220 MHz. Radiophys Quantum Electron 1977; 20:989–996.

Suzuki S, Sheridan KV, Dulk GA. Polarization and position measurements of Type III bursts. In: Kundu MR, Gergely TE, editors. Radio Physics of the Sun, vol. 86 of IAU Symposium. 1980; 315–321.

Thejappa G, MacDowall RJ. Effects of Scattering on Radio Emission from the Quiet Sun at Low Frequencies. Astrophys J 2008; 676:1338–1345.

Tingay SJ, Goeke R, Bowman JD, Emrich D, Ord SM, Mitchell DA, Morales MF, Booler T, Crosse B, Wayth RB, Lonsdale CJ, Tremblay S, Pallot D, Colegate T, Wicenec A, Kudryavtseva N, Arcus W, Barnes D, Bernardi G, Briggs F, Burns S, Bunton JD, Cappallo RJ, Corey BE, Deshpande A, Desouza L, Gaensler BM, Greenhill LJ, Hall PJ, Hazelton BJ, Herne D, Hewitt JN, Johnston-Hollitt M, Kaplan DL, Kasper JC, Kincaid BB, Koenig R, Kratzenberg E, Lynch MJ, Mckinley B, Mcwhirter SR, Morgan E, Oberoi D, Pathikulangara J, Prabu T, Remillard RA, Rogers AEE, Roshi A, Salah JE, Sault RJ, Udaya-Shankar N, Schlagenhaufer F, Srivani KS, Stevens J, Subrahmanyan R, Waterson M, Webster RL, Whitney AR, Williams A, Williams CL, Wyithe JSB. The Murchison Widefield Array: The Square Kilometre Array Precursor at Low Radio Frequencies. Publ Astron Soc Aust 2013a; 30:e007.

Tingay SJ, Oberoi D, Cairns I, Donea A, Duffin R, Arcus W, Bernardi G, Bowman JD, Briggs F, Bunton JD, Cappallo RJ, Corey BE, Deshpande A, deSouza L, Emrich D, Gaensler BM, R G, Greenhill LJ, Hazelton BJ, Herne D, Hewitt JN, Johnston-Hollitt M, Kaplan DL, Kasper JC, Kennewell JA, Kincaid BB, Koenig R, Kratzenberg E, Lonsdale CJ, Lynch MJ, McWhirter SR, Mitchell DA, Morales MF, Morgan E, Ord SM, Pathikulangara J, Prabu T, Remillard RA, Rogers AEE, Roshi A, Salah JE, Sault RJ, Udaya-Shankar N, Srivani KS, Stevens J, Subrahmanyan R, Waterson M, Wayth RB, Webster RL, Whitney AR, Williams A, Williams CL, Wyithe JSB. The Murchison Widefield Array: solar science with the low frequency SKA Precursor. J. Phys. Conf. Ser. vol. 440. 2013b; 012033.

Tsvetanov ZI, Charugin VM. The Brightness Temperature of Radio Sources with Synchrotron Self-Absorption. Sov Astron 1981; 25:293.

Verbanac G, Vršnak B, Živković S, Hojsak T, Veronig AM, Temmer M. Solar wind high-speed streams and related geomagnetic activity in the declining phase of solar cycle 23. Astron Astrophys 2011; 533:A49.

Waldmeier M. Synoptische Karten der Sonnenkorona. Mit 16 Textabbildungen. Z Astrophys 1956; 38:219.

Wang M, Duan C, Xie R, Yan Y. Highly polarized Type III microwave bursts on 15 April 1998. Sol Phys 2003; 212:401–406.

Wang YM. Coronal Holes and Open Magnetic Flux. Space Sci Rev 2009; 144:383–399.

Weiss LAA, Stewart RT. Solar radio bursts of spectral type V. Aust J Phys 1965; 18:143.

Wentzel DG. Polarization of fundamental type III radio bursts. Sol Phys 1984; 90:139–159.

White SM, Kundu MR. Radio Observations of Gyroresonance Emission from Coronal Magnetic Fields. Sol Phys 1997; 174:31–52.

Wild JP, McCready LL. Observations of the Spectrum of High-Intensity Solar Radiation at Metre Wavelengths. I. The Apparatus and Spectral Types of Solar Burst Observed. Aust J Sci Res A 1950; 3:387.

Wild JP, Smerd SF, Weiss AA. Solar Bursts. Ann Rev Astron Astrophys 1963; 1:291.

Woo R, Habbal SR. Coronal Hole Myth. American Astronomical Society Meeting Abstracts. vol. 31, Bull. Amer. Astron. Soc. 1999; 870.

Woo R, Habbal SR, Howard RA, Korendyke CM. Extension of the Polar Coronal Hole Boundary into Interplanetary space. Astrophys J 1999; 513:961–968.

Zhang P, Yu S, Kontar EP, Wang C. On the Source Position and Duration of a Solar Type III Radio Burst Observed by LOFAR. Astrophys J 2019; 885:140.

Zheleznyakov VV, Zaitsev VV. The Origin of Type-V Solar Radio Bursts. Sov Astron 1968; 12:14.

Zlobec P, Messerotti M, Dulk GA, Kucera T. VLA and Trieste observations of type I storms, type IV and pulsations. Sol Phys 1992; 141:165–180.

Zucca P, Carley EP, McCauley J, Gallagher PT, Monstein C, McAteer RTJ. Observations of Low Frequency Solar Radio Bursts from the Rosse Solar-Terrestrial Observatory. Sol Phys 2012; 280:591–602.